2017

The Evolution of Luminous Compact Blue Galaxies in COSMOS between z~0.0-1.0

Lucas Hunt

The Evolution of Luminous Compact Blue Galaxies in COSMOS between z∼0.0-1.0

Lucas Hunt

Dissertation Submitted to
The Eberly College of Arts and Sciences
at West Virginia University
in partial fulfillment of the requirements
for the degree of

Doctor of Philosophy
in
Physics

Dr. D.J. Pisano Ph.D., Chair
Dr. Loren Anderson Ph.D.
Dr. Sean McWilliams Ph.D.
Dr. John Jones Ph.D.

Moragntown, West Virginia
2017

Keywords: galaxies: evolution; galaxies: star formation; radio continuum: galaxies;

Abstract

The Evolution of Luminous Compact Blue Galaxies in COSMOS between z∼0.0-1.0

Lucas Hunt

Luminous Compact Blue Galaxies are bright, compact star forming galaxies that are common in the distant universe, but rare locally. In this thesis we have conducted studies tracing changes in the LCBG population between z=0.0-1.0 in the COSMOS survey region. We used the luminosity function to show LCBG's contribution to the luminosity density is increasing between z=0.0-1.0. From this we also find the number density of LCBGs is increasing by an order of magnitude from z=0.0-1.0. Finally we show that 10% of galaxies brighter than $M_B = -18.5$ are LCBGs at $z \sim 0.1$ but 62% are LCBGs at $z \sim 0.9$ indicating LCBGs are a significant population of bright star forming galaxies at high redshift. In the second study we use the COSMOS HI Large Extragalactic Survey (CHILES) and CHILES Con Pol to trace star formation rate and HI in LCBGs to higher redshift. We determine the HI mass and distribution of two LCBGs in CHILES. We find the average star formation rate of LCBGs increases between z=0.0-1.0 from 2 $M_\odot$ yr^{-1} to 53 $M_\odot$ yr^{-1}. Finally, we set upper limits on the evolution of the average HI mass in LCBGs between z=0.0-0.45, which range from $(2.3 - 5.6)x10^9$ $M_\odot$. In the last study we report on the first observations of HI in gravitationally lensed galaxies behind the galaxy cluster Abell 773. We find the upper limit for the average HI mass in the lensed galaxies at z=0.398 to be 6.58×10^9 $M_\odot$ and the upper limit for the HI mass of the galaxy at z=0.487 to be 1.5×10^{10} $M_\odot$. We use an automated flagging routine to remove RFI which reduces the noise in the spectrum by 25% when compared to spectrum in which we discarded integrations with RFI.

Acknowledgements

I would like to start by thanking my wife Johanna. This degree is as much hers as it is mine. Her love and support helped pull me through the difficult times and her encouragement helped push me the rest of the way. Especially when I wasn't moving as fast as I needed to.

I would also like to thank my parents Bev and Doug, and my brothers Dustin and Caleb. It's easy to take chances in life when you know you have help to fall back in if it didn't work. Continuously moving farther away from home to pursue my dream hasn't always been easy but having family along for the ride has eased the transition. Thank you to all of you for being there whenever I call.

Next I would like to thank my advisor, D.J. Pisano. He's always made me feel more like a peer than a student. He allowed me to work at my own pace and his door was always open for a discussion when it was needed. I truly appreciate the opportunities to work on unique and exciting projects, and to see different parts of the world while doing it. Thank you so much for helping me grow as an astronomer and a person.

I need to thank my "physics family", my friends, officemates, and colleagues: Joe, Pete, Mehran, Fernando, Sarah, Golnoosh, Akshaya, Nipuni, Amy, Nick, and numerous others who have made life in Morgantown a joy. The late nights doing homework, endless conversations, geocaching adventures, friends dinners, football games, early morning workouts and other various escapades, have made Morgantown feel more like home. Thank you for the memories.

Next I want to thank various people who have helped and inspired me as to continue pursuing a career as a scientist. Carson Cook, Jacqueline van Gorkom, Brigid Geroux, Steve Crawford, Ed Churchwell, Snezana Stanimirovic, and countless others. Your kindness and generosity mean more to me than you'll likely know!

I want to thank my committee, D.J., Loren Anderson, Sean McWilliams, and John Jones, for taking the time to read my work, and providing feedback that have improved this document!

Finally, I want to say hi Michaela! Daddy loves you.

Table of Contents

List of Tables vi

List of Figures vii

1 Introduction 1
- 1.1 The Evolution of Blue Galaxies . . . 1
- 1.2 Photometry and The Luminosity Function . . . 5
- 1.3 Evolution of Gas in Galaxies and Measuring Star Formation Rates . . 6
- 1.4 HI at High Redshift . . . 10

2 The Evolution of the Luminosity Function of Luminous Compact Blue Galaxies in COSMOS 12
- 2.1 Introduction . . . 12
- 2.2 Data . . . 16
  - 2.2.1 Photometric data . . . 17
  - 2.2.2 Spectroscopic Data . . . 18
  - 2.2.3 Sample Selection . . . 19
- 2.3 Luminosity Function Estimate . . . 24
  - 2.3.1 Luminosity Function Estimator . . . 24
  - 2.3.2 Weighting . . . 26
  - 2.3.3 Comparison to Previous Work . . . 27
- 2.4 The LCBG Luminosity Function . . . 30
- 2.5 Conclusion . . . 42

3 A Study of Luminous Compact Blue Galaxies in the CHILES field 45
- 3.1 Introduction . . . 46
- 3.2 Sample Selection, Data, and Reduction . . . 49
  - 3.2.1 Sample Selection . . . 49
  - 3.2.2 Observations . . . 49
  - 3.2.3 Spectral Line Data Reduction and Imaging . . . 50
  - 3.2.4 Continuum Data Reduction, Imaging . . . 51
  - 3.2.5 Radio Continuum Sample . . . 52
- 3.3 HI Stacking . . . 52
- 3.4 Star Formation Rates . . . 55
  - 3.4.1 Avoiding AGN Contamination . . . 58
- 3.5 Results and Discussion . . . 59
  - 3.5.1 HI Detections . . . 59
  - 3.5.2 HI Mass Limits . . . 62
  - 3.5.3 LCBG Star Formation Rates . . . 64
- 3.6 Conclusions . . . 70

4 The Search for HI Emission at z ≈ 0.4 in Gravitationally Lensed Galaxies with the Green Bank Telescope 72
4.1 Introduction . . . 73
4.2 Observations and Analysis . . . 77
4.2.1 Sources . . . 77
4.2.2 Observations . . . 77
4.2.3 Data Reduction . . . 80
4.2.4 RFI and Flagging Routine . . . 81
4.3 Results . . . 85
4.4 Discussion . . . 87
4.4.1 Effectiveness of Flagging . . . 87
4.4.2 Mass Limits . . . 90
4.5 Conclusions and Future Work . . . 92

5 Conclusion 95
5.1 Future studies of LCBGs . . . 96
5.2 Gravitationally Lensed HI . . . 97

List of Tables

2.1 Photometric offsets 18
2.2 Comparison of luminosity function to previous work 28
2.3 Schechter function parameters derived from fit to the luminosity function 31

3.1 HI properties of detected LCBGs 59
3.2 Properties of the stacked HI spectra of LCBGs 63
3.3 Star formation rates of LCBGs in CHILES Con POl 66
3.4 Describing evolution of star formation in LCBGs 66

4.1 Summary of lensed HI observations 79

List of Figures

2.1 Comparison of surface brightness and color for galaxies in COSMOS . 21
2.2 Comparison of absolute magnitude and surface brightness for galaxies in COSMOS 22
2.3 Comparison of absolute magnitude and color for galaxies in COSMOS 23
2.4 Comparison of luminosity function to previous work 29
2.5 Luminosity function for our work 32
2.6 Absoulte magnitude vs redshift in COSMOS 33
2.7 Evolution of M* with redshift 36
2.8 Evolution of ϕ^* with redshift 37
2.9 Evolution of j_B with redshift 38
2.10 Evolution of LCBG number density in COSMOS 40
2.11 Evolution of the fraction of LCBGs in COSMOS 43

3.1 HI contours and optical image of LCBG J100055.2+022343 61
3.2 HI contours and optical image of LCBG J100103.7+023053 61
3.3 Stacked HI spectra of LCBGs in CHILES 62
3.4 Evolution of star formation rate of LCBGs in CHILES Con Pol . . . 67
3.5 Fraction of star formation rate coming from LCBGs 69

4.1 Optical image of Abell 773 showing lensed sources 78
4.2 Spectra showing tests of flagging routine 86
4.3 Final spectra of lensed HI sources 88
4.4 Examples of how flagging routine works on a single integration 90
4.5 Number of times a channel was flagged using our routine 91
4.6 Estimating the magnification required to detect lensed HI with the GBT between z=0.0-1.0 93

Chapter 1

Introduction

1.1 The Evolution of Blue Galaxies

The Egyptian astronomer Ptolemy divided stars into classes based on how bright they appeared on the sky. The brightest stars were labeled class 1 stars while the dimmest were labeled class 6. Astronomers still use a more specific, accurate, and expanded version of this classification system known as the magnitude system. Eventually astronomers began measuring the temperature of stars, and the Hertzsrpung-Russell (H-R) (Russell, 1914) diagram was created by comparing the magnitude and temperature of multiple stars in a cluster. This diagram showed a sequence of stars diagonally across the middle known as the main sequence. Main sequence stars are fusing hydrogen in their cores to generate energy and emit light. Johnson & Morgan (1953) defined the first wide band photometric filter system which only allowed light within a small wavelength range to reach the sensor of the telescope. This filter system was developed to classify stars based on their colors, where color is defined as the difference in the magnitude of a star as measured with two different filters. If you plot a star's color versus it's magnitude, the plot looks similar to the H-R diagram, where stars that are brighter in a blue filter than a red filter are found in the high temperature section of the H-R diagram. These hot, bright stars are massive and short-lived main-sequence stars that quickly use up

their hydrogen and become giant stars or supernovae. The presence of these blue stars therefore indicates that star formation must have recently occurred in that region.

Light from these blue stars can be 10^5 times more luminous than that of the Sun, therefore a small number of these stars present in any galaxy would dominate the light we see from that galaxy. If a galaxy appears blue in color astronomers can infer it must contain these massive, short-lived stars, which means it must have recently created stars. This general relation between color and star formation allows astronomers to effectively target galaxies for in-depth analyses, for example to get a more accurate determination of how many stars these blue galaxies are creating, or how much a blue or red galaxy changes with time. Light from distant objects is stretched by the expansion of the universe and we must correct these effects to compare objects at different distances.

The cosmic expansion of the universe means space is expanding and objects are continuously moving farther away from us. This expansion also stretches the light coming from distant objects to longer wavelengths. Because space is expanding at a faster rate the farther away you move, light from distant objects will be stretched to lower frequencies. This stretching is quantified as:

$$\frac{\nu_{em} - \nu_{obs}}{\nu_{obs}} = z \tag{1.1}$$

Where ν_{em} is the frequency the light is emitted, ν_{obs} is the frequency the light is observed, and z is the redshift. As an example, an object emitting light at a

frequency of ν_{em}=100 GHz with a redshift $z = 0.5$ will be observed at a frequency of $\nu_{obs} = 100/(1 + 0.5) = 66.7$ GHz. Because the speed of light is constant, light emitted from distant objects takes a longer time to reach us on Earth and we are seeing that object as it appeared when the universe was younger. We can therefore also use redshift as a simple estimate of both time and distance. We can trace the evolution of galaxies using this property by looking at objects of varying distances and determining what the typical properties of galaxies were at different times in the universe.

As we look farther away we see blue galaxies become more numerous (Tyson, 1988). This excess of blue galaxies implies star forming galaxies were more common in the early universe. Studies of the star formation rate (SFR) at UV, optical and infrared wavelengths have confirmed this, and in fact have shown that between $z = 0.0 - 1.0$, a lookback time of 7.16 Gyr, the star formation rate density of the universe, the star formation rate per unit volume, increases by an order of magnitude (Hopkins & Beacom, 2006; Hopkins, 2004; Glazebrook et al., 2004; Wilson et al., 2002; Haarsma et al., 2000; Flores et al., 1999). Astronomers know that the star formation rate density of the universe is changing, but still need to answer why it is changing. To do this we are studying a class of compact rapidly star forming galaxies known as Luminous Compact Blue Galaxies (LCBGs) whose number density declines in concert with the star formation rate density of the universe (Phillips et al., 1997).

LCBGs first appeared as point sources on plate images from ground based telescopes, and were believed to be quasars (Koo et al., 1986). Follow up spec-

troscopic studies of these quasar candidates found some had emission lines similar to local star forming galaxies and removed them from the sample (Koo & Kron, 1988). These contaminating sources were LCBGs. The Hubble Space Telescope was finally able to resolve these objects as compact star forming galaxies beyond z=0.2 (Koo et al., 1994) and continued observations of these sources with the Keck Low Resolution Imaging Spectrograph and Hubble Space Telescope showed that LCBGs made up $\sim$ 20% of the total galaxy population and up to 45% of the star formation rate density of the universe between z=0.4-1.0 (Guzmán et al., 1997; Phillips et al., 1997). Eventually selection criteria were developed to to facilitate targeted studies of similar types of objects at all redshifts. These targeted studies are critical to understanding why and how the evolution of the SFR density happens with redshift, because of the link between LCBGs and SFR density. LCBG selection criteria will be discussed further in Chapters 2 and 3.

Studies of LCBGs have been done in snapshots, often confined to small areas, small redshift ranges, or both. Using deep, multi-wavelength photometric surveys with a large number of sources, we can trace the evolution of LCBGs using consistently generated data products over the redshift range z=0.0-1.0. We look specifically at the evolution of the number and fraction of LCBGs, brightness of LCBGs, and SFR in LCBGs between z=0.0-1.0, and the evolution of gas in LCBGs between z=0.0-0.45.

1.2 Photometry and The Luminosity Function

Astronomers have developed a simple statistical technique, known as the luminosity function, to trace galaxy evolution by creating a histogram of galaxy magnitudes and dividing by the volume in which the galaxies were observable. A change in the number of galaxies in each bin, with a change in redshift, represents a change in the typical brightness and number density of galaxies. To make sure brightness is consistently measured, some simple corrections must be made to the apparent magnitude of the galaxy based on its redshift.

We must first correct for the distance of an object, because objects near by could be perceived as having the same apparent magnitude as a brighter object, further away. To do this we convert the apparent magnitude to absolute magnitude by determining the magnitude of the object at a set distance of 10 pc using:

$$\mathrm{M} = \mathrm{m} - 5(\log_{10}(D_L) - 1) \tag{1.2}$$

Where M is the absolute magnitude, m is the apparent magnitude, and D_L is the luminosity distance defined by the relationship between the bolometric flux and luminosity. We must also correct for the difference in the emitted and observed frequency and the change in the width of the filter being used. Imagine a filter that allows light from 1 MHz to 2 MHz to reach the sensor on the telescope. If the source being observed is at z=0.5 then the light measured by the detector was emitted from the galaxy between 1×(1+0.5) and 2×(1+0.5) or 1.5-3 MHz. So the light being detected by the 1 MHz filter was emitted over a frequency range of 1.5

MHz. This correction is done by subtracting a term known as a k-correction. Our conversion from apparent magnitude to absolute magnitude then becomes:

$$\mathrm{M} = \mathrm{m} - 5(\log_{10}(D_L) - 1) - k \tag{1.3}$$

Studies using this counting method, known as a luminosity function, have seen an evolution in the number of bright blue galaxies with redshift. For example, results from Beare et al. (2015) are consistent with cosmic down-sizing in which massive, bright, blue galaxies cease star formation earlier than their less massive counterparts. Beare et al. (2015) also find evidence that blue galaxies evolve to red galaxies over time. In Chapter 2 we generate the luminosity function of LCBGs between z=0.01-1.0 in redshift bins of z=0.2 to determine how LCBGs evolve in magnitude, number density, luminosity density and fraction of the galaxy population using a single, consistent dataset.

1.3 Evolution of Gas in Galaxies and Measuring Star Formation Rates

The increase in SFR between z=0.0-1.0 was described in Section 1.1. These stars form from gas which we can also study to determine how gas properties such as mass change with redshift, and how these changes compare to changes in star formation rate. Stars form from clouds of dense molecular gas, mostly molecular hydrogen (H_2) which has few emission mechanisms and is difficult to observe. H_2 is made from the more ubiquitous atomic neutral hydrogen (HI) which does have

an observable emission line at 1420.4 MHz that is created by a small change in the energy of a hydrogen atom. This change in energy is from the spontaneous transition of the spin of the electron and proton in the atom from a parallel state to an anti-parallel state. The transition rate for this flip is 2×10^{-15} s^{-1} meaning it happens on average once every $\sim 10^7$ years. But because hydrogen is so abundant in most galaxies like the Milky Way, emission from this transition is easily visible in the nearby universe. The radiation from this transition is very weak, however, so the detection of HI at high redshift is difficult. Observations of HI at high redshift therefore require more collecting area and long integration times to increase the signal to noise ratio.

Observations of HI provide a view of galaxies distinct from optical images. HI is optically thin, meaning that an emitted photon will be able to travel out of the galaxy without getting absorbed and we can see all of the photons being emitted. Knowing this allows us to estimate how much of the gas is emitting and, using the mass of a hydrogen atom, the entire mass of hydrogen gas in galaxies. We can determine the HI mass of a source with a given integrated flux density (S), or the amount of radiation passing through a given solid angle, using the equation (Wieringa et al., 1992):

$$M_{HI} = \frac{2.35 \times 10^5}{(1+z)} \left(\frac{D_L}{\text{Mpc}}\right)^2 \left(\frac{S}{\text{Jy km s}^{-1}}\right) \tag{1.4}$$

Where D_L is the luminosity distance, z is the redshift, and S is the flux density integrated over the width of the emission line in velocity units. HI in disk galaxies

also typically extends far beyond the visible light from stars (Rao & Briggs, 1993) and allows us to determine how fast the galaxy is rotating. We can use this speed to determine how much mass must be rotating inside this disk as well. Measures of the rotation speed of galaxies at large radii from Hα spectra provided the first evidence of dark matter (Rubin & Ford, 1970).

Large surveys of HI in the local universe like ALFALFA (Giovanelli et al., 2005), have found HI mass in detected galaxies ranges from the survey limit of $\sim 10^7$ to 10^{10} $M_\odot$. Studies of galaxies in the ALFALFA sample have also found that SFR increases with HI mass (Huang et al., 2012), and galaxies in dense environments appear to be gas poor (Stark et al., 2016; Odekon et al., 2016).

Studies of HI in LCBGs have been confined to the local universe due to the weak emission. Garland et al. (2004) studied LCBGs with the Green Bank Telescope (GBT) and found they are typically gas rich, with median values of $M_{HI} = 5 \times 10^9 M_\odot$. Rabidoux et al. (2014) and Garland et al. (2007) targeted the same sample of LCBGs with the VLA, and GMRT, and found the GBT overestimated the HI mass by 66%, because the GBT beam likely contained companion galaxies. This indicates that to get a more accurate measurement of HI in LCBGs we need resolved studies.

As mentioned in Section 1.1, we see an overall increase in SFR density as we look to higher redshift. We target light from or associated with massive stars to measure SFR accurately, because they are short-lived and their presence indicates star formation must have recently occurred. Some indicators include light at optical wavelengths emitted from hydrogen which has been ionized by massive

stars, the temperature of dust that is heated by massive stars measured at infrared wavelengths, and radio emission from electrons accelerated by supernova. When we have estimated the number of massive stars we can use an initial mass function, a function that describes the mass distribution of stars when they are formed, to determine how many lower mass stars have formed with the massive stars.

SFRs for LCBGs have been derived using various tracers including the equivalent width of the [O II] line (Phillips et al., 1997; Crawford et al., 2016), Hα emission (Garland et al., 2015), infrared luminosity (Crawford et al., 2016; Garland et al., 2005), and radio continuum (Garland et al., 2005). Crawford et al. (2016) found about half of the LCBGs in their sample had a higher estimated SFR when measured at infrared wavelengths, which trace the dust heated by massive stars and is not typically effected by obscuration, as opposed to the [O II] equivalent width, which can underestimate the emission from massive stars because some of the light gets blocked by dust in the plane of the galaxy.

In Chapter 3 we use data from the COSMOS HI Large Extragalactic Survey (CHILES), a deep field HI survey using 1000 hours on the VLA, to search for the evolution of HI in LCBGs between z=0.0-0.45. This is the first survey with continuous spectral line frequency coverage from 960-1430 MHz and a long enough integration time to detect HI in more than 300 galaxies in its volume (Fernández et al., 2016). We also use information from CHILES Con Pol, a commensal radio continuum project that will create the most sensitive radio image of the sky to date, to measure the evolution of the SFR of LCBGs in the CHILES area. In Chapter 3 we discuss how the SFR and HI mass of LCBGs in the COSMOS region change

with redshift

1.4 HI at High Redshift

As mentioned above, HI emission is weak and difficult to detect beyond the local universe. HI has been directly detected in an individual galaxy at z=0.378 by the CHILES team (Fernández et al., 2016). The object was a Ultra Luminous Infrared Galaxy (ULIRG), a massive, gas rich, star forming galaxy that is bright at infrared wavelengths due to the rapid star formation rate, with $M_{HI}=(2.9 \pm 1.0) \times 10^{10}$ $M_{\odot}$. The second most distant direct HI detection is at z=0.24 (Catinella & Cortese, 2015). Other studies have averaged the signal from multiple galaxies to determine the average HI mass of $(9.5 \pm 0.4) \times 10^9$ at z=0.11 (Delhaize et al., 2013), to $(3.83 \pm 1.20) \times 10^9$ at z=0.37 (Rhee et al., 2016). Planned deep field surveys with telescopes such as ASKAP, MeerKAT and the Square Kilometer Array (SKA) (Meyer, 2009; Holwerda et al., 2012; Staveley-Smith & Oosterloo, 2015) will have the sensitivity and frequency coverage required to directly detect HI emission in individual galaxies beyond $z = 0.45$.

Until that time, we can use gravitational lensing as a cosmic telescope to detect HI in individual galaxies out to z=1.0. Strong gravitational fields can act like a magnifying glass, stretching the light of objects behind them making them appear brighter on the sky. This effect is achromatic, meaning it affects all light uniformly regardless of frequency. The magnification effect does not change the surface brightness of the object but stretches the object to cover a larger area or create multiple

images of the same object on the sky. Gravitational lensing has been used in a similar fashion before to detect CO in distant galaxies (Brown & Vanden Bout, 1991), and has been used to observe galaxies beyond z=10 at optical wavelengths (Coe et al., 2013). A thorough review of the topic can be found in Schneider (2006). In Chapter 4 we report on observations of HI in gravitationally lensed galaxies, and a method of interference removal for high redshift HI observations.

Finally, in Chapter 5 we give an overview of the results and discuss future plans.

Chapter 2

The Evolution of the Luminosity Function of Luminous Compact Blue Galaxies in COSMOS[1]

Abstract

Luminous Compact Blue Galaxies are a class of compact star forming galaxies that are common at z=1 and rare in the local universe. Their drop in number density roughly follows the drop in star formation rate density from z=1. We present a study of the evolution of the luminosity function of these rapidly evolving galaxies between z≈0-1 using a reanalysis of COSMOS photometry and spectroscopic redshift information generated by the Galaxy and Mass Assembly team. We find that M* decreases by ∼0.7 mag, ϕ^* decreases by a factor of 6, and the number density of LCBGs decreases by a factor of 11.5 from z=1. We find that LCBGs make up ∼ 62% of galaxies brighter than M_B=-18.5 at z=0.9 and only ∼ 10% at z=0.1.

2.1 Introduction

Early Hubble deep field observations were able to resolve a class of compact, bright, star forming galaxies that were seen as point sources in ground based telescope observations and identified as different from stars and QSOs based on optical

[1]Work in this chapter was done in collaboration with D.J. Pisano (WVU), Steve Crawford (SAAO), and Matt Bershady (UW-Madison)

emission lines visible in spectroscopic observations (Koo et al., 1994). The Hubble deep field observations allowed for deeper photometric and spectroscopic studies of these objects. Werk et al. (2004) showed that the number density of these objects out to z=0.045 is roughly an order of magnitude lower than their number density at z=0.85 (Phillips et al., 1997) making them one of the most rapidly evolving galaxy types in the universe (Rawat et al., 2007).Their evolution correlates with the drop in the star formation rate density of the universe from z=1 to present day. Study of the nature and evolution of these galaxies is therefore imperative to reaching a deeper understanding of galaxy evolution as a whole.

The literature describes three classes of galaxies that have similar star formation rates, sizes and colors: compact narrow emission line galaxies (CNELGs Koo et al., 1994, 1995; Guzmán et al., 1996, 1998) faint blue galaxies (Guzmán et al., 1997; Phillips et al., 1997), and blue nucleated galaxies (Schade et al., 1995, 1996). These similar galaxies were coalesced into one class and labeled Luminous Compact Blue Galaxies (LCBGs). The photometric criteria that define LCBGs: $M_B < -18.5$, B-V<0.6, and $SB_e(B) < 21$ mag arcsec^{-2} (Werk et al., 2004), include most galaxies in the original three samples, and allows for studies that target sources with the same selection criteria at all redshifts.

It is also important to note that other galaxy types that overlap with LCBGs in luminosity, color and surface brightness, have previously been described. Cardamone et al. (2009) showed Green Pea galaxies, detected by the Galaxy Zoo project, overlap with LCBGs in blue luminosity, morphology, stellar mass, and metallicity. Higher mass LCBGs also overlap with Ultraviolet Luminous Galaxies (UVLGs),

which were identified by Heckman et al. (2005) as being local counterparts to Lyman Break Galaxies. Guzmán et al. (2003) and Hoyos et al. (2004) have both suggested that LCBGs could be low mass lower redshift counterparts to the high redshift Lyman Break Galaxies. Phillips et al. (1997) and Guzmán et al. (1997) noted that ∼40% of their sample resemble HII galaxies, local, vigorously star forming galaxies. Finally, we note that LCBGs are distinct from Blue Compact Dwarf galaxies (BCDs). LCBGs are more massive (Guzmán et al., 1997; Garland et al., 2004; Tollerud et al., 2010), luminous (Garland et al., 2004), and have higher metallicity (Tollerud et al., 2010) than Blue Compact Dwarfs.

Previous studies of LCBGs have concentrated on small snapshots in time, often being limited to low or intermediate redshift. Intermediate redshift (z>0.5) studies have looked at LCBG morphology (Noeske et al., 2006) and spectral properties (Tollerud et al., 2010), environment (Crawford et al., 2006, 2014, 2016; Randriamampandry et al., 2017), and number density (Guzmán et al., 1997; Phillips et al., 1997). LCBGs make up about 50% of the Butcher-Oemler population in galaxy clusters between redshift, z=0.55-1 (Crawford et al., 2006), and are likely on their initial descent into a cluster (Crawford et al., 2014). There is no significant difference in size, mass, luminosity, star formation rate, or metallicity between cluster and field LCBGs (Crawford et al., 2016). Randriamampandry et al. (2017) found cluster LCBGs have a lower dynamical to stellar mass ratio than field LCBGs at intermediate redshift, but both populations have a statistically similar distribution. Guzmán et al. (1997) and Phillips et al. (1997) found that LCBGs are similar to local HII star forming galaxies, they constitute ∼45% of the star formation rate

density and ∼20% of the galaxy population at z=0.6, and show no evolution in specific star formation rate. Tollerud et al. (2010) found LCBGs have a wide range of metallicities and show no correlation between size and oxygen abundance or M_*.

Studies of local LCBGs have looked at number density (Werk et al., 2004), neutral gas content (Garland et al., 2007; Rabidoux et al., 2014), kinematics from three-dimensional optical spectroscopy (Pérez-Gallego et al., 2011), and morphology and environment (Garland et al., 2015). They have shown that LCBGs are rare locally (Werk et al., 2004), are rotationally supported (Rabidoux et al., 2014; Pérez-Gallego et al., 2011), and are not exclusively generating stars in a merger scenario (Rabidoux et al., 2014; Garland et al., 2015; Pérez-Gallego et al., 2011). Garland et al. (2015) finds local LCBGs fit into roughly three categories: 20% have star formation that is likely triggered by strong interactions, 40% are clumpy spiral galaxies whose star formation is triggered by smoothly accreted gas from tidally disrupted companions or the intracluster medium, and 40% are non-clumpy, non-spiral field galaxies with centrally concentrated morphologies, smaller effective radii, and smaller stellar masses.

In this study we examine the evolution of LCBGs using a consistent, large sample. We generate the luminosity function, and derive the number density in redshift increments of z=0.2 between z=0 and z=1. Throughout this paper we adopt H_0=70 km s^{-1} Mpc^{-1}, $\Omega_M = 0.3$, $\Omega_\Lambda = 0.7$ and we use the Vega magnitude system. In Section 2.2 we describe the data set we used, and how we selected LCBGs from that sample. In Section 2.3 we describe the $1/V_{Max}$ method which we used to generate the luminosity function, and how our calculation of the luminosity function

compares to previous work. In Section 2.4 we discuss the results from the LCBG luminosity function and how compare them to the total galaxy population. Finally, in Section 2.5 we summarize our results.

2.2 Data

We use data obtained as part of the COSMOS survey with photometry rederived by the Galaxy and Mass Assembly (GAMA) survey team. COSMOS is an HST Treasury Project (Scoville et al., 2007) that used 590 orbits on the Hubble Space Telescope (HST) Advanced Camera for Surveys to survey a two square degree equatorial field. The survey was originally designed to better understand the evolution of galaxies and AGN over cosmic time and how that evolution depends on environment from groups to large scale structures, such as filaments and voids. One of the key features of the COSMOS field is its accessibility by most astronomical facilities. This has lead to surveys being carried out across the electromagnetic spectrum from radio (Smolčić et al., 2017a) to x-ray (Civano et al., 2016).

GAMA is a project utilizing a number of ground and space based facilities to study cosmology, and galaxy formation and evolution. Their main goal is to study structures in the universe on scales ranging from 1 kpc to 1 Mpc. This includes galaxy structure, mergers, groups, and clusters. To do this they are amassing large multi-wavelength photometric and spectroscopic datasets across numerous regions of the sky. They have adopted the publicly available data from the COSMOS survey as their G10 region (Davies et al., 2015; Andrews et al., 2017), the GAMA region

at 10 hours right ascension.

2.2.1 Photometric data

The photometric dataset covers the central 1 degree^2 and includes observations from UV (Zamojski et al., 2007), optical (Capak et al., 2007; Taniguchi et al., 2007, 2015), and infrared (McCracken et al., 2012; Sanders et al., 2007; Oliver et al., 2012) bands. Magnitudes were calculated using the Lambda-Adaptive Multi-Band Deblending Algorithm in R (LAMBDAR Wright et al., 2016). LAMBDAR is a software package designed to provide matched aperture photometry over images that are neither pixel- nor PSF-matched. It is specifically produced to provide consistent photometry and uncertainty to calculate the spectral energy distribution of objects in large, multi-instrument, multi-wavelength surveys such as GAMA, or COSMOS. We use the CFHT u^* and Subaru B_j, V_J, r^+, i^+, z^+ photometry for our derivations.

Our photometric sample includes galaxies with $15 \leq i^+ \leq 22.5$, roughly matching the target catalog for zCOSMOS, $15 \leq I_{F814W} \leq 22.5$. This is the photometric completeness limit for Capak et al. (2007) from which zCOSMOS targets were chosen. Since most spectroscopic data comes from zCOSMOS, using their photometry eliminates the need for photometric completeness corrections, and maximizes the number of objects with available spectroscopic information. We excluded stars and bright x-ray sources that are more likely to be AGN using the master star-galaxy classification from Andrews et al. (2017). We also derived photometric offsets be-

tween the G10 reduction and the templates from version 4.3 of the Blanton & Roweis (2007) k-correction code , which we used to calculate our absolute magnitudes and select our source list of LCBGs. These offsets are listed in Table 2.2.1.

filter	offset
B_j.....	-0.051
V_j.....	0.07
r^+.....	-0.013
i^+.....	-0.045
z^+.....	-0.018

Table 2.1 Photometric offsets between apparent magnitude in Andrews et al. (2017) and spectral templates from Blanton & Roweis (2007)

2.2.2 Spectroscopic Data

We used a compilation of spectroscopic redshifts gathered and reanalyzed by the GAMA team. The catalog uses redshift information from GAMA's AUTOZ (Baldry et al., 2014), zCOSMOS-bright 20k (Lilly et al., 2009), PRIsm MUlti-object Survey (Coil et al., 2011; Cool et al., 2013), VIMOS VLT Deep Survey (Garilli et al., 2008), Sloan Digital Sky Survey (Ahn et al., 2014), and the 30 band photometric redshift catalog (Ilbert et al., 2009) to determine the best-fit redshift for each object. Full details of their reanalysis can be found in Davies et al. (2015). Objects were assigned quality flags of 1 to 4, 1 being robust, high resolution redshifts from VIMOS or SDSS, 2 being spectroscopic redshifts from the PRIMUS survey, 3 being uncertain spectroscopic redshifts, and 4 being photometric redshifts. We use the robust sample from Davies et al. (2015), which includes all objects with flags 1 & 2.

2.2.3 Sample Selection

As stated previously, Werk et al. (2004) define LCBGS as galaxies with $M_B \leq$-18.5 mag, $\mu_e(B) \leq$21 mag arcsec^{-2}, and (B-V)$_0$ $\leq$0.6 mag. This combination of parameters provides the best distinction between intermediate redshift LCBGs and irregular, elliptical and spiral galaxies. Werk et al. (2004) point out that LCBGs are not distinct galaxies in the luminosity-color-surface brightness parameter space, but exist at the extreme end of the continuum of galaxies in said space as shown in Figures 2.1, 2.2, and 2.3.

Absolute magnitudes were calculated using the equation:

$$M^{Ref} = m^{Obs} - DM(z, H_0, \Omega_m, \Omega_\Lambda) - KC(z, SED) \tag{2.1}$$

where M^{Ref} is the reference frame absolute magnitude, and m^{obs} is the observed apparent magnitude. DM is the Distance Modulus at redshift z defined as $5(\log_{10}(D_L)-1)$, assuming a cosmology defined by H$_0$, Ω_m, Ω_Λ which we defined in 2.1 and KC is the k-correction defined as:

$$KC(z, SED) = (k^{ref}(z) + m^{Obs}(z) - m^{Ref}(z))^{SED} \tag{2.2}$$

where k^{ref}(z) is the k-correction for the reference frame filter assuming the object is at redshift z, m^{Obs}(z) is the observed apparent magnitude, and m^{Ref}(z) is the reference frame apparent magnitude. The SED superscript indicates these values are taken from fitting to a galaxy template. This roughly follows the procedure from

Ilbert et al. (2005). We integrated the C libraries from *kcorrect* (Blanton & Roweis, 2007) into our Python code to generate the k-correction and reference magnitudes. The absolute magnitude was calculated using the observed filter closest to the rest-frame B band. This minimized the applied k-correction and the error associated with it.

Surface brightness was calculated using the absolute magnitude, with the equation:

$$\mu_e = M_B + 2.5 \times \log_{10}(2\pi R_e^2) + 36.572 \tag{2.3}$$

where M_B is the absolute magnitude in the B band, and R_e is the effective (or half-light) radius from Tasca et al. (2009). The half-light radius was converted from I_{F814W} to B using Equation 2.4 taken from Lange et al. (2015) as:

$$\log_{10}(R_{e,B}) = 0.108 \times \log_{10}\left(\frac{\lambda_{F814W}}{\lambda_B}\right) + \log_{10}(R_{e,F814W}) \tag{2.4}$$

This simplifies to $R_{e,B}$=1.0659×$R_{F814W,e}$.

Finally, all rest frame colors were calculated using:

$$(M_1 - M_2)_0 = m_1 - m_2 - KC_1 + KC_2 \tag{2.5}$$

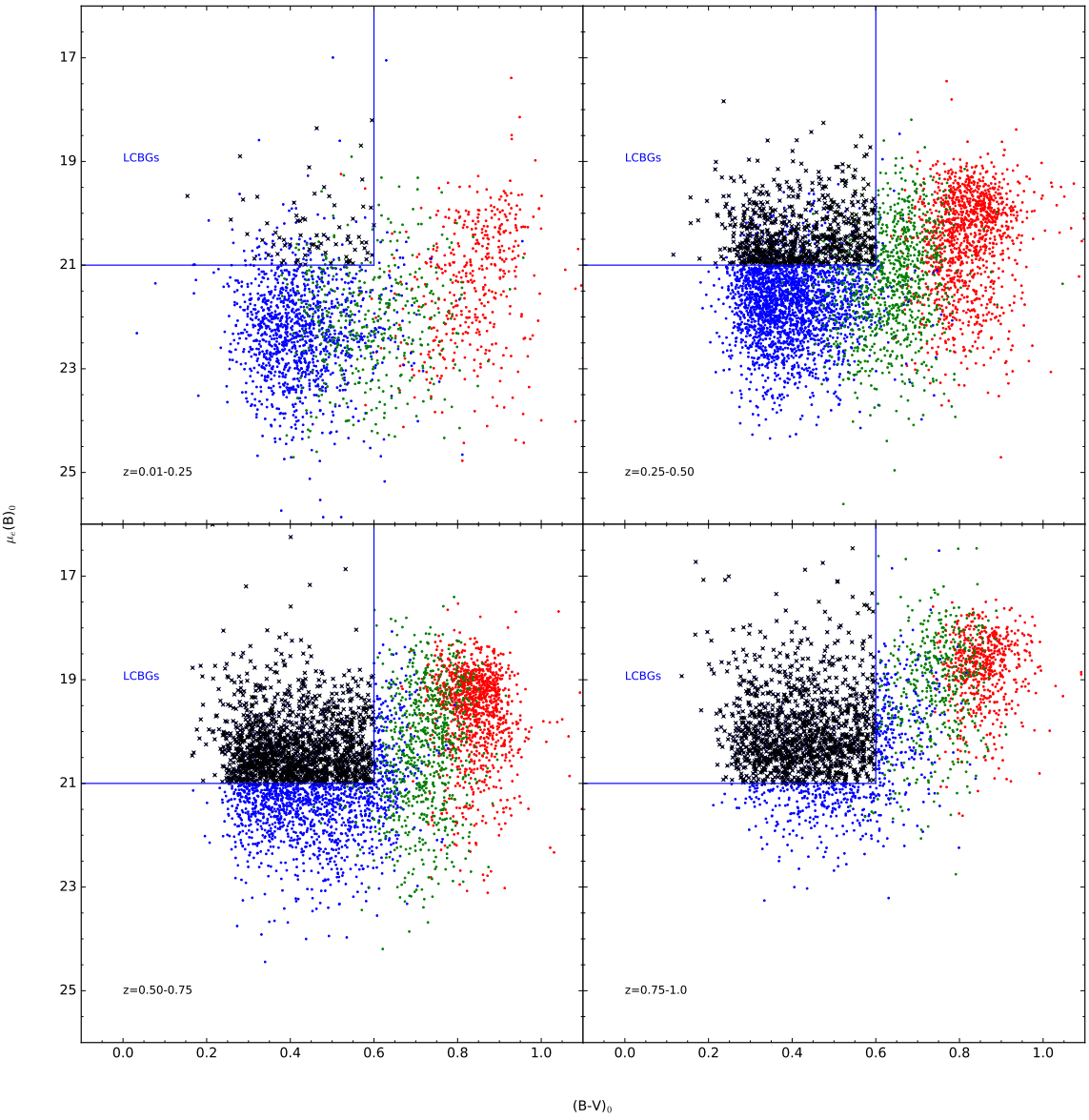

Figure 2.1 Comparison of surface brightness and color selection criteria for LCBGs. All LCBGs (black,x) will fall within the demarcated region of the B-band surface brightness vs color ($\mu_e(B)_0$ vs $(B\text{-}V)_0$) plot, but not all points in the demarcated region are LCBGs. All values are calculated in the galaxies rest frames. The points are colored to denote whether they fall within the red cloud, green valley, or blue cloud based on their $(U\text{-}B)_0$ color as characterized by Willmer et al. (2006).

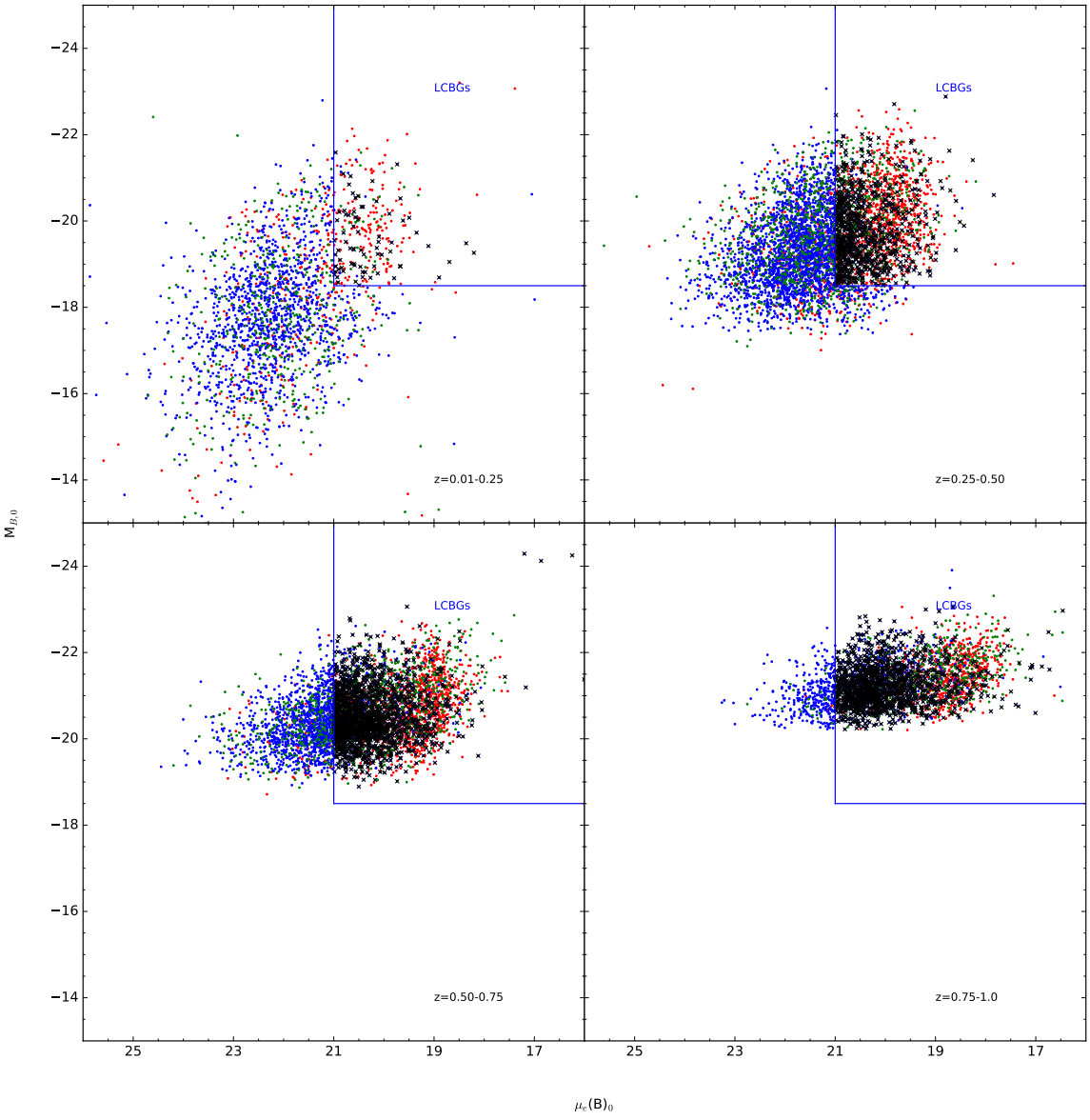

Figure 2.2 Same as figure 2.1 but for magnitude vs surface brightness.

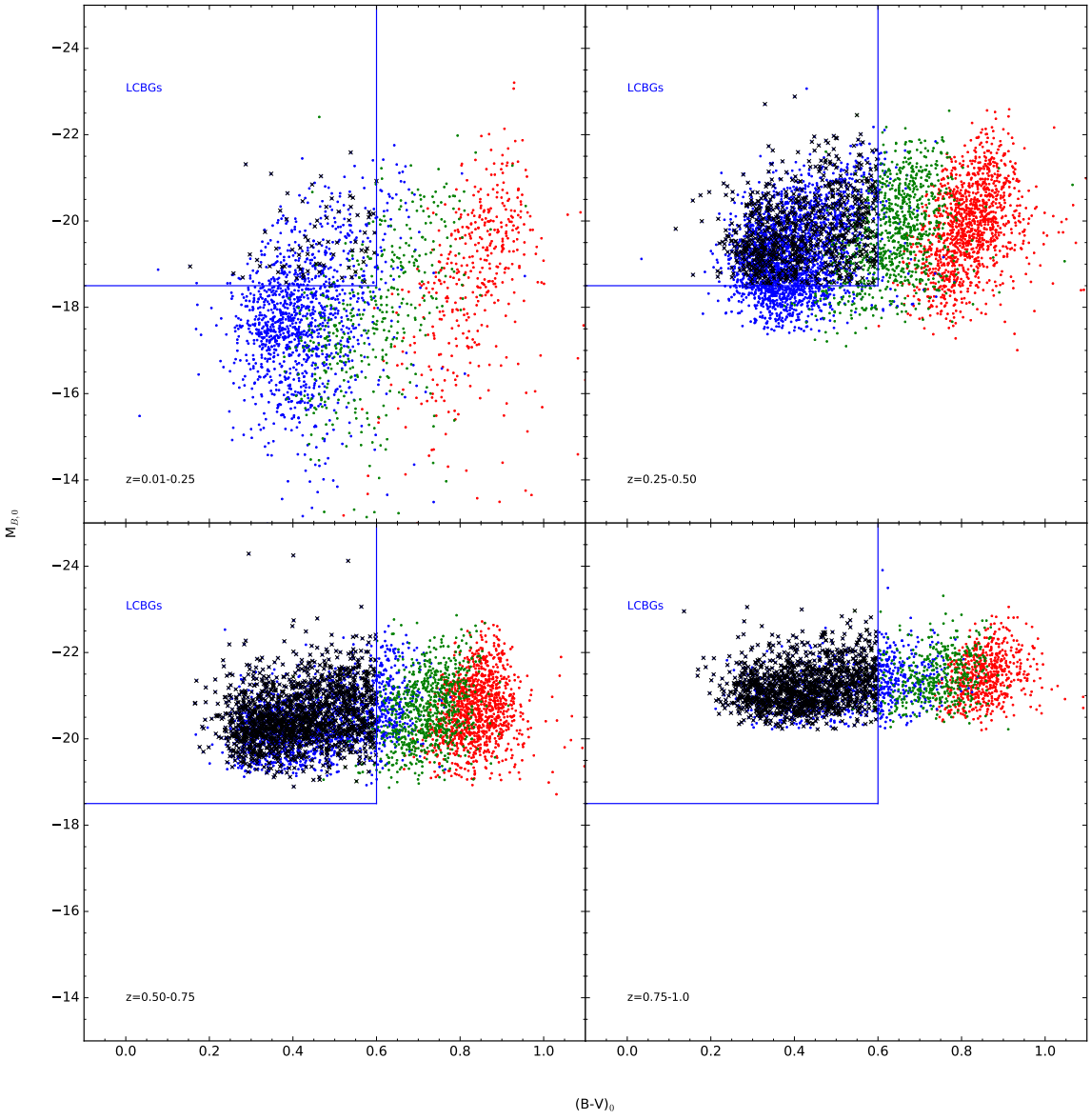

Figure 2.3 Same as Figure 2.1 but for magnitude and color.

2.3 Luminosity Function Estimate

2.3.1 Luminosity Function Estimator

The luminosity function is defined as the number of galaxies per comoving volume, per magnitude bin, and is most often characterized using the Schechter (1976) parameterization. In magnitudes it is defined as

$$\phi(M)dM = 0.4\ ln(10)\ \phi^*\ 10^{0.4(M-M^*)(\alpha+1)}\exp(-10^{0.4(M^*-M)})dM \qquad (2.6)$$

Where ϕ^* is the characteristic number density of galaxies per unit volume per unit magnitude, M* is the characteristic magnitude where the luminosity function turns over from an exponential into a power law, and α is the characteristic slope of that power law describing the faint end of the luminosity function. Several methods have been developed to estimate the luminosity function, including Schmidt (1968); Lynden-Bell (1971); Turner (1979); Tammann et al. (1979); Choloniewski (1986); Efstathiou et al. (1988).

For our analysis we used the $1/\mathrm{V}_{Max}$ method (Schmidt, 1968) which counts galaxies within a known volume. We followed the calculations laid out by Willmer et al. (2006) and Ilbert et al. (2005), described below. The integral luminosity function for a given absolute magnitude is defined as:

$$\int_{M_{bright}}^{M_{faint}} \phi(M)dM = \sum_{i=1}^{N_G} \frac{\chi_i}{V_{max}(i)} \qquad (2.7)$$

where χ_i is the weighting applied to correct for completeness (discussed in Section 2.3.2) and $V_{max}(i)$ is the maximum comoving volume within which a galaxy i with absolute magnitude M_i can be detected in the survey, defined as:

$$V_{max}(i) = \int_{\omega} \int_{z_{min,i}}^{z_{max,i}} \frac{dV}{dz d\omega} dz d\omega \tag{2.8}$$

Here again, z is redshift, and ω is the solid angle of the survey region. In a magnitude limited survey, $z_{min,i}$ and $z_{max,i}$ are defined by:

$$z_{min,i} = \min(z_{min}, z(M_i, m_l)) \tag{2.9}$$

$$z_{max,i} = \max(z_{max}, z(M_i, m_u)) \tag{2.10}$$

where z_{min} and z_{max} are the lower and upper limits of the redshift bin the object occupies, and $z(M_i, m_l)$ and $z(M_i, m_u)$ are the redshifts at which an object with absolute magnitude M_i would no longer fall in the apparent magnitude limits of the survey. We determined the Poisson error using:

$$\sigma_{\phi} = \sqrt{\frac{\chi_i}{V^2_{max,}(i)}} \tag{2.11}$$

For our calculations, we used magnitude bins of 0.5 and redshift bins of 0.2.

2.3.2 Weighting

We considered galaxies in the survey that have not been directly counted due either to photometric incompleteness or spectroscopic incompleteness. As stated in Section 2.2.1 we adopted similar photometric selection criteria to zCOSMOS, namely $15 \leq i^{+} \leq 22.5$ to maximize the number of sources with spectroscopic redshifts. We did not adopt a photometric correction because the G10 catalog is complete to $m_{i^{+}}=24.5$ mag (Andrews et al., 2017), below our selection of $m_{i^{+}}=22.5$.

We made two corrections to compensate for spectroscopic incompleteness. First, we corrected for the photometrically identified galaxies that were not targeted in a spectroscopic survey. This weight is labeled as the target sample rate, and defined as:

$$w_{TSR} = \frac{N_{Phot}^{gal}}{N_{Spec}^{gal}} \tag{2.12}$$

where N_{Phot}^{gal} is the number of objects observed in the photometric catalog, and N_{Spec}^{gal} is the number of objects targeted in the spectroscopic survey. We also corrected for objects that were targeted in the spectroscopic survey, but whose redshifts were unable to be definitively determined. This spectroscopic sampling rate weighting is defined as:

$$w_{SSR} = \frac{N_{spec}^{gal}}{N_{spec}^{gal} - N_{spec}^{fail}} \tag{2.13}$$

where N_{spec}^{gal} is the number of galaxies observed spectroscopically, and N_{spec}^{fail} is the number of galaxies where the redshift was indeterminable. If we define the number of galaxies with secure redshifts as $N_{spec}^{sec} = N_{spec}^{gal} - N_{spec}^{fail}$, then the total weight of

each object, χ_i, is the multiple of the two weights described above:

$$\chi_i = \frac{N_{Phot}^{gal}}{N_{spec}^{gal}} \frac{N_{spec}^{gal}}{N_{spec}^{gal} - N_{spec}^{fail}} = \frac{N_{Phot}^{gal}}{N_{spec}^{sec}} \tag{2.14}$$

The likelihood of obtaining a secure redshift varies with apparent magnitude, so we calculate weights in magnitude bins of 0.5. Weights generally range from 1.04 to 1.6, with six very bright objects having a low target sample rate and corrections above 5.5.

2.3.3 Comparison to Previous Work

We fit a Schechter function to our data points using the *scipy* function *curve_fit* which uses the Levenberg-Marquardt algorithm to fit the derived points. The function also returns a covariant matrix, and the error for each value is calculated using the *uncertainties* package in *python*. The points from our $1/\mathrm{V}_{max}$ calculation are plotted at the average absolute magnitude of their bin, and the error bars on each point indicate the 1σ Poisson errors, calculated as mentioned in Section 2.3. We then compared our results with those from Zucca et al. (2009), who previously studied the effect of environment on the evolution of the luminosity function in COSMOS.

	This Paper				Zucca,2009			
z-bin	Number	α_{Vmax}	M^*_B-5log(h_{70})	$\phi^*(10^{-3}\ h_{70}^{-3}\ \mathrm{MPC}^{-3})$	Number	α_{STY}	M^*_B-5log(h_{70})	$\phi^*(10^{-3}\ h_{70}^{-3}\ \mathrm{MPC}^{-3})$
$0.1-0.35$	4039	$-1.15^{+0.06}_{-0.06}$	$-20.70^{+0.15}_{-0.15}$	$5.85^{+0.93}_{-0.93}$	1968	$-1.09^{+0.04}_{-0.04}$	$-20.85^{+0.10}_{-0.11}$	$5.62^{+0.58}_{-0.56}$
$0.35-0.55$	4147	$-1.03^{+0.06}_{-0.06}$	$-20.69^{+0.07}_{-0.07}$	$6.19^{+0.53}_{-0.53}$	2059	$-0.82^{+0.08}_{-0.08}$	$-20.67^{+0.05}_{-0.06}$	$6.40^{+0.58}_{-0.59}$
$0.55-0.75$	3999	$-0.95^{+0.06}_{-0.06}$	$-20.89^{+0.04}_{-0.04}$	$7.07^{+0.33}_{-0.33}$	2163	$-0.85^{+0.11}_{-0.11}$	$-20.98^{+0.09}_{-0.10}$	$6.59^{+0.57}_{-0.61}$
$0.75-1.0$	2993	$-0.99^{+0.41}_{-0.41}$	$-21.12^{+0.17}_{-0.17}$	$7.45^{+0.62}_{-0.62}$	1769	$-1.59^{+0.16}_{-0.16}$	$-21.57^{+0.13}_{-0.15}$	$4.32^{+0.17}_{-0.17}$
$0.3-0.8$	2993	$-1.10^{+0.06}_{-0.06}$	$-20.89^{+0.08}_{-0.08}$	$5.83^{+0.59}_{-0.59}$	5249	$-1.03^{+0.04}_{-0.04}$	$-21.02^{+0.05}_{-0.05}$	$5.42^{+0.32}_{-0.32}$

Table 2.2 We compare the Schechter parameters fit to the luminosity function derived using the $1/\mathrm{V}_{max}$ method to the parameters derived from Zucca et al. (2009) using the STY (Tammann et al., 1979) method.

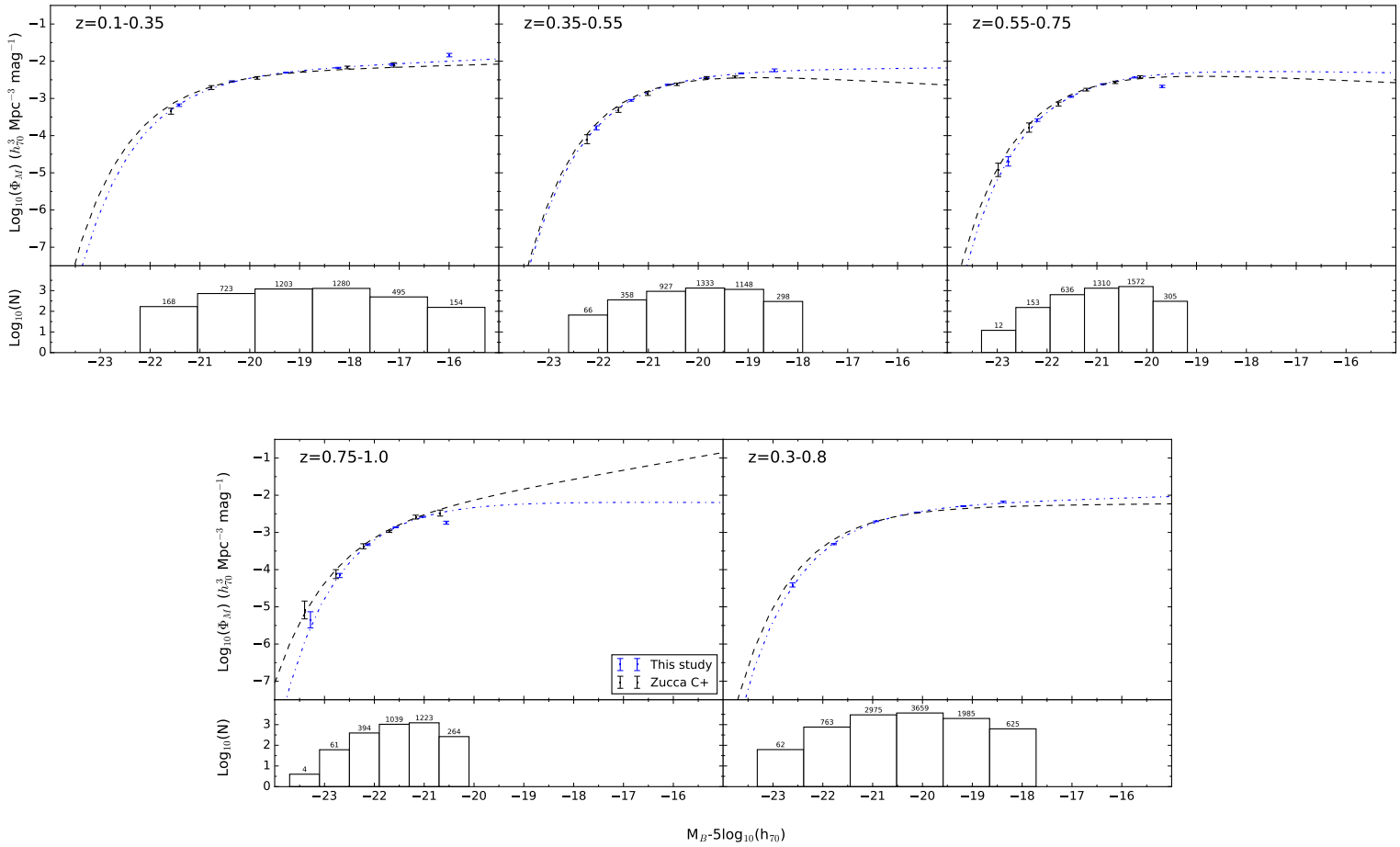

Figure 2.4 Comparing our results with those from Zucca et al. (2009). Our $1/V_{max}$ results are plotted along with the Schechter function that best fits our data (blue). We have also plotted the Schechter function calculated by Zucca et al. (2009) using the STY method (black line) and the points from their use of the C^+ estimator (black points)

We compare the Schechter function parameters fit to our $1/V_{max}$ calculation, to the Schechter function parameters derived from the STY method by Zucca et al. (2009) in Table 2.2. The STY (Tammann et al., 1979) method is a maximum likelihood method first described by Sandage, Tammann and Yahil and subsequently named after them. Figure 2.4 shows our $1/V_{max}$ data points and subsequent fit in blue, and shows the points from Zucca et al. (2009) using the C^+ method (Zucca et al., 1997), a non-parametric, cumulative estimator along with the Schechter function estimated by Zucca et al. (2009) using the STY method.

We see from Table 2.2 that our Schechter function parameters are consistent with Zucca et al. (2009) in the bins z=0.1-0.35, z=0.55-0.75, and z=0.3-0.8. In the bin z=0.35-0.55 the faint end slope, α varies by greater than 1σ and in the bin z=0.75-1.0 both M^* and ϕ^* vary by greater than 1σ. In the bin z=0.75-1.0 we are not sampling enough of the absolute magnitude range to get a strong fit to M^* and ϕ^* so our fit is very uncertain. The points calculated by Zucca et al. (2009) using the C^+ method seen in Figure 2.4 match our fit within 1σ except at $M\sim -19$ in the bin z=0.35-0.55 and at ~ -23 in the bin z=0.75-1.0. In some bins, z=0.1-0.35 for example, the points from the C^+ method match the fit to our $1/V_{max}$ calculation better than the STY method. We did this comparison to show our calculations are consistent with previous work. We now move to calculating the LCBG luminosity function between z=0.0-1.0 in redshift bins of z=0.2.

2.4 The LCBG Luminosity Function

z-bin	Number	α_{Vmax}	M^*_B-5log(h_{70}) (mag)	ϕ^* (10^{-3} h_{70}^{-3} Mpc^{-3})	j_B (10^8 h_{70}L$_\odot$Mpc^{-3})
Total Sample					
$0.01-0.2$	1253	$-1.30^{+0.05}_{-0.05}$	$-20.59^{+0.24}_{-0.24}$	$3.46^{+0.77}_{-0.77}$	$0.68^{+0.15}_{-0.15}$
$0.2-0.4$	4573	$-1.0^{+0.03}_{-0.03}$	$-20.51^{+0.06}_{-0.06}$	$8.87^{+0.56}_{-0.56}$	$1.91^{+0.15}_{-0.15}$
$0.4-0.6$	3171	$-0.98^{+0.06}_{-0.06}$	$-20.67^{+0.08}_{-0.08}$	$4.85^{+0.42}_{-0.42}$	$1.23^{+0.14}_{-0.14}$
$0.6-0.8$	3888	$-0.94^{+0.17}_{-0.17}$	$-20.80^{+0.14}_{-0.14}$	$7.39^{+1.05}_{-1.05}$	$2.16^{+0.41}_{-0.41}$
$0.8-1.0$	2507	$-0.85^{+0.15}_{-0.15}$	$-20.905^{+0.08}_{-0.08}$	$8.93^{+0.56}_{-0.56}$	$2.97^{+0.28}_{-0.28}$
$0.3-0.8$	10077	$-1.053^{+0.08}_{-0.08}$	$-20.852^{+0.10}_{-0.10}$	$5.83^{+0.67}_{-0.67}$	$1.74^{+0.26}_{-0.26}$
LCBGs					
$0.01-0.2$	27	$-0.61^{+0.37}_{-0.37}$	$-20.33^{+0.41}_{-0.41}$	$0.71^{+0.27}_{-0.27}$	$0.14^{+0.07}_{-0.07}$
$0.2-0.4$	508	$-1.06^{+0.24}_{-0.24}$	$-20.08^{+0.25}_{-0.25}$	$1.51^{+0.45}_{-0.45}$	$0.29^{+0.07}_{-0.07}$
$0.4-0.6$	838	$-0.86^{+0.14}_{-0.14}$	$-20.55^{+0.17}_{-0.17}$	$1.53^{+0.27}_{-0.27}$	$0.36^{+0.09}_{-0.09}$
$0.6-0.8$	1342	$-0.88^{+0.36}_{-0.36}$	$-20.56^{+0.26}_{-0.26}$	$3.24^{+0.81}_{-0.81}$	$0.77^{+0.28}_{-0.28}$
$0.8-1.0$	1131	$-1.12^{+0.21}_{-0.21}$	$-20.86^{+0.12}_{-0.12}$	$4.30^{+0.49}_{-0.49}$	$1.26^{+0.25}_{-0.25}$
$0.3-0.8$	2571	$-0.52^{+0.15}_{-0.15}$	$-20.37^{+0.13}_{-0.13}$	$2.68^{+0.28}_{-0.28}$	$0.55^{+0.08}_{-0.08}$

Table 2.3 Schechter function parameters for the entire galaxy population and for LCBGs from z=0.01-1.0 in redshift bins of z=0.2

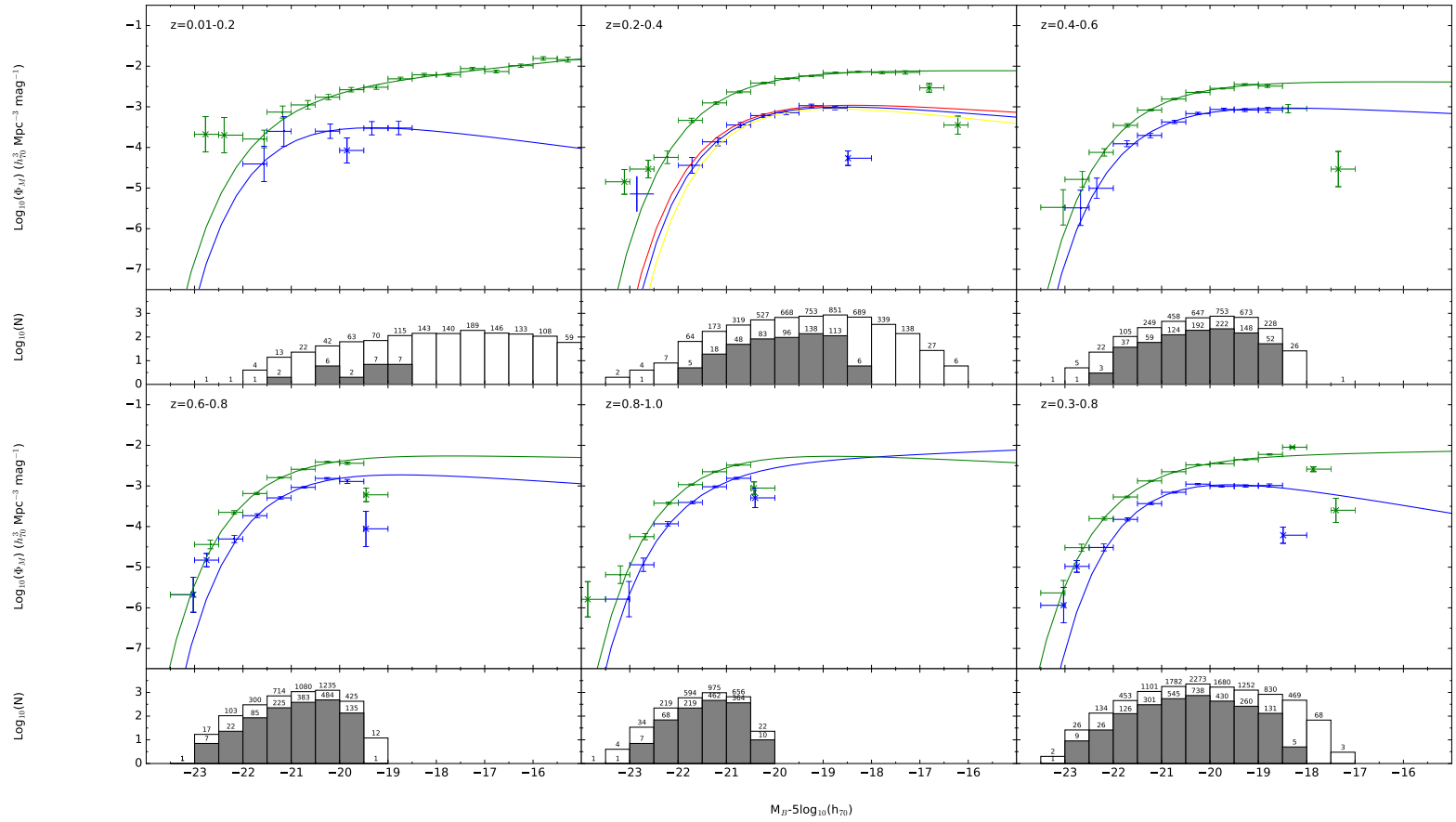

Figure 2.5 Luminosity function for the entire galaxy population (green) and LCBGs (blue). Points mark the average absolute magnitude of sources in that bin, not necessarily the center of the magnitude bin. Points marked with an x are not considered in our fit. They are either not well populated (<3 objects) or objects where the absolute magnitude is detected across less than half the redshift bin (see Figure 2.6. The histogram below each plot shows the $\log_{10}$ of the number of objects in each bin, with the white bars being total galaxies, and the gray bars being LCBGs. The number in each bin is listed above each bar.

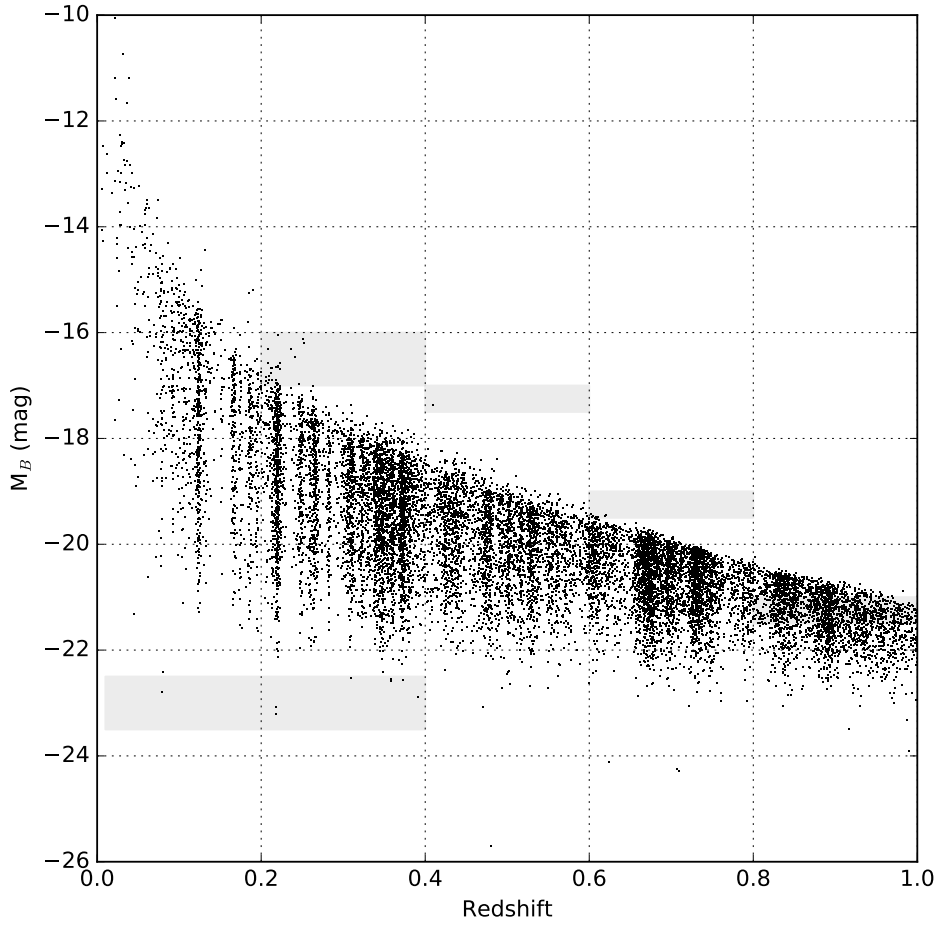

Figure 2.6 The absolute magnitude of galaxies vs redshift. Absolute magnitude ranges that are sampled in less than half the bins are discarded from our luminosity function. The gray regions denote the z-M$_B$ bins that were discarded

We show Schechter function parameters for both the total galaxy population and LCBGs in Table 2.3. The data covers approximately the same redshift range as Zucca et al. (2009), and we see a similar trend in the evolution of M*, approximately 0.4 between z=0.0-1.0. The evolution of M* in the LCBG population is greater, evolving by roughly 0.7 over the same redshift range. This should be expected as both Willmer et al. (2006) and Beare et al. (2015) have found stronger evolution of

M^* in blue galaxies than in the total galaxy population or in red galaxy population over the same range. This evolution is consistent with cosmic downsizing (Cowie et al., 1996) of the blue population of galaxies, wherein the brighter galaxies exhaust their ability to form stars and fade, leaving smaller, less luminous blue galaxies in the local universe.

Evolution of M^* and ϕ^* can be seen in Figures 2.7 and 2.8. In both figures we compare the values we calculated for M^* and ϕ^* to those from six other surveys that looked at the galaxy luminosity function between z≈0.0-1.0. Willmer et al. (2006) studied the evolution of the galaxy luminosity function to z∼1 using the Deep Evolutionary Exploratory Probe 2 (DEEP2) redshift survey. They found the populations of blue and red galaxies, split based on their $(U\text{-}B)_0$ color as defined above, evolve differently with blue galaxies showing an increase in luminosity with redshift, but little change in number density, and red galaxies showing little change in luminosity with redshift but a large change in number density. We also compare to Faber et al. (2007) who combined data from DEEP2 and the COMBO-17 survey and found that there are likely different quenching modes which lead blue galaxies to evolve into red galaxies. Zucca et al. (2009) used COSMOS data to study the evolution of the luminosity function for galaxies of different spectrophotometric types and in different environments. They found that the different evolution of spectrophotometric late and early type galaxies is consistent with the idea that some blue galaxies evolve into red galaxies as cosmic time increases, and that most of the transformation in dense regions likely happened before z=1, while the evolution is still occurring in underdense regions. Cool et al. (2012) studied the luminosity

function from the AGN and Galaxy Evolution Survey and found strong evolution in the luminosity function between z=0.05-0.75. Fritz et al. (2014) found the evolution of luminosity of galaxies on the red sequence is consistent with a passively evolving old stellar population between z=0.4-1 using the VIMOS Public Extragalactic Redshift Survey. Beare et al. (2015) found the blue galaxies are more numerous than red galaxies at all redshifts between z=0.1-0.9, especially at the faint end of the luminosity function using the $\sim 410,000$ galaxies in the Boötes survey.

We see our value for ϕ^* for all galaxies is higher than other surveys at z$\sim$0.3. This is likely due to an overdensity of galaxies in that redshift bin. Our value for ϕ^* is also high at z$\sim$0.9, likely due to how well we can estimate the faint end slope of the Schechter function, α. ϕ^*, M* and α are all dependent on each other, specifically ϕ^* and M* vary depending on α. This can be seen in Table 2.2 in the redshift bin z=0.75-1.0 where the value of α found by us differs from the value calculated by Zucca et al. (2009) and we find a higher characteristic magnitude and number density. We see this in Figure 2.7 as well, where our value for M* is lower, likely due to our value of α being lower.

As discussed in Section 8.4 of Beare et al. (2015), ϕ^* and M* evolve for most galaxy populations, but there is little agreement in how much they vary. This can be attributed to the degenerate nature of the Schechter parameters, and in particular the variance in ϕ^* and M* with the adopted value of α. Measurements of the luminosity density (j) vary much less than measurements of ϕ^* and M* because j is dependent on ϕ^* and M* and brighter luminosities (lower values of M*) correlate with lower ϕ^*. Calculation of the luminosity density requires integrating the luminosity

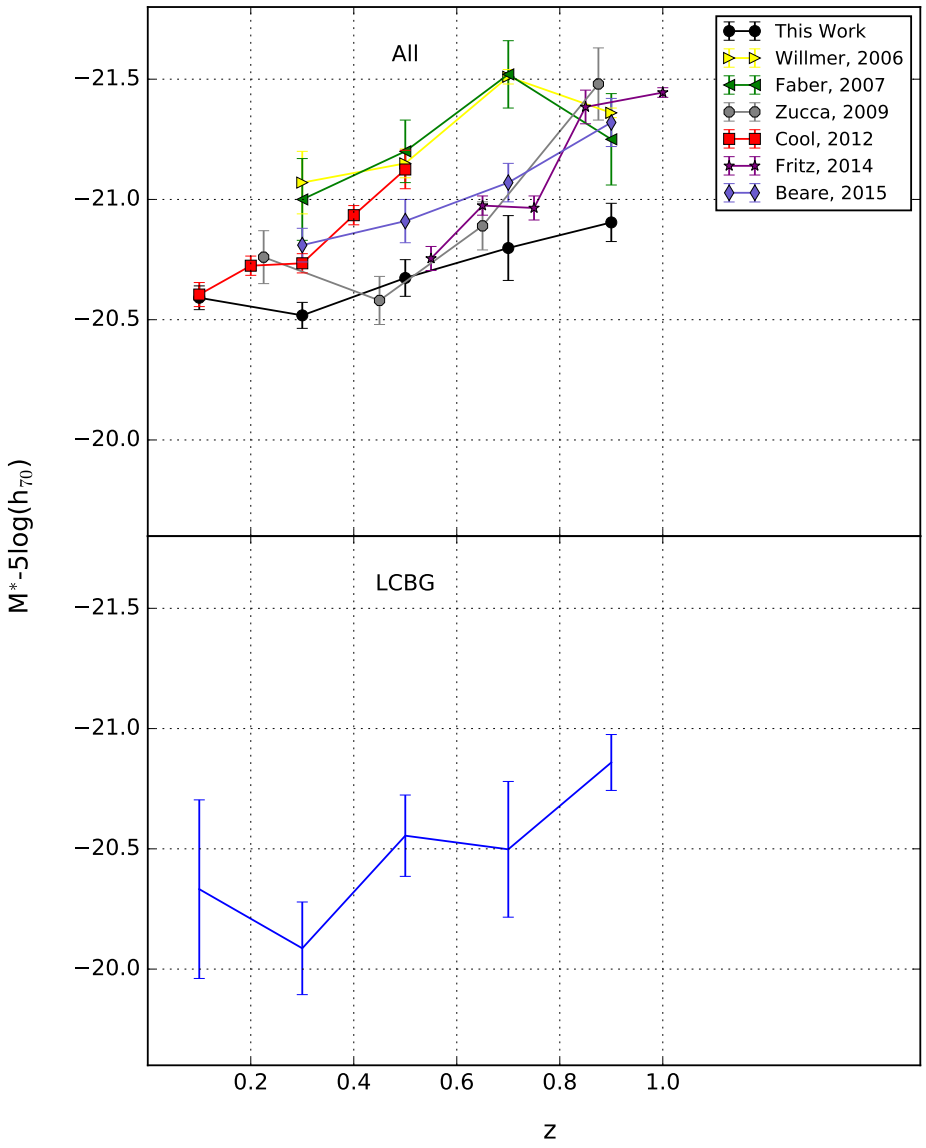

Figure 2.7 Evolution of M* with redshift between z=0.0-1.0 in bin sizes of z=0.2. We compare our values for the total luminosity function to those from Willmer et al. (2006), Faber et al. (2007), Zucca et al. (2009), Cool et al. (2012), Fritz et al. (2014) and Beare et al. (2015). Vertical axes are the same for comparison between all galaxies and LCBGs.

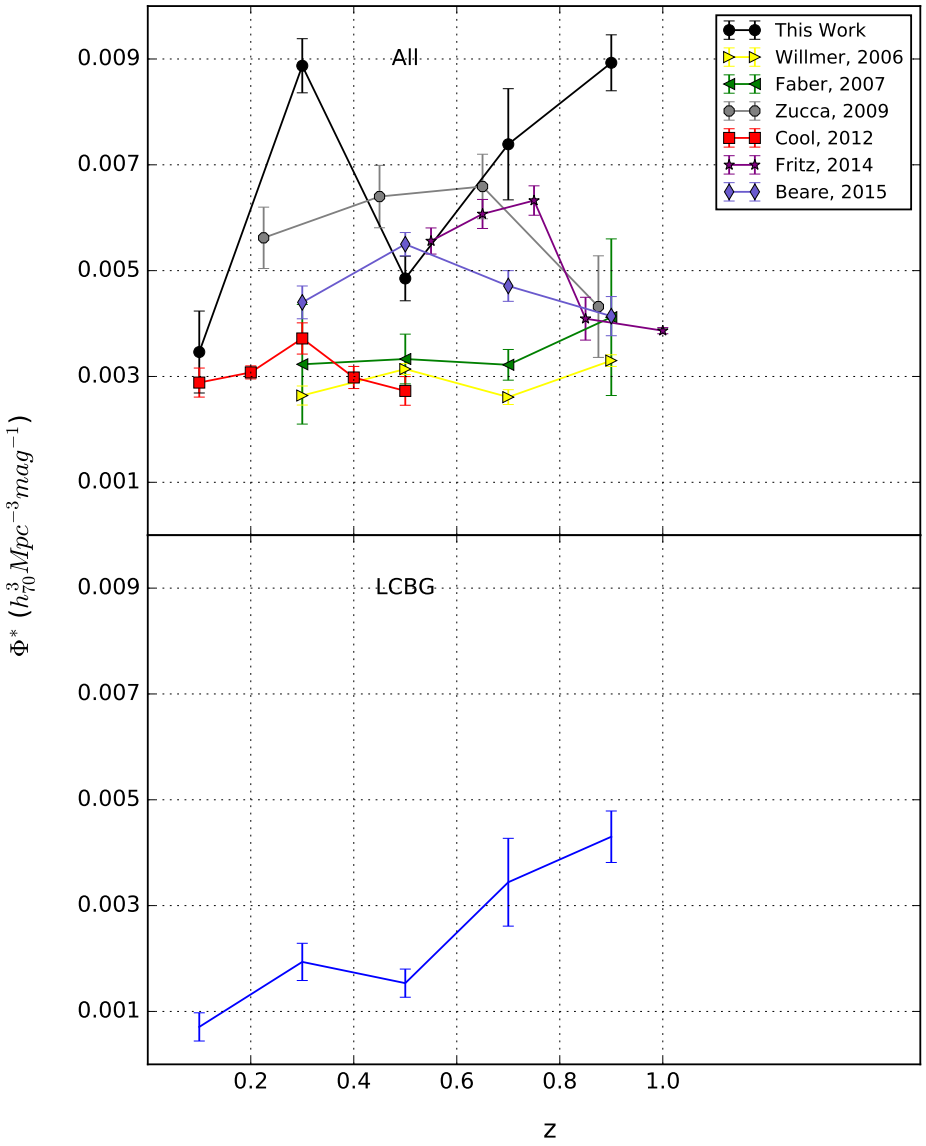

Figure 2.8 Same as Figure 2.7 but for ϕ^*

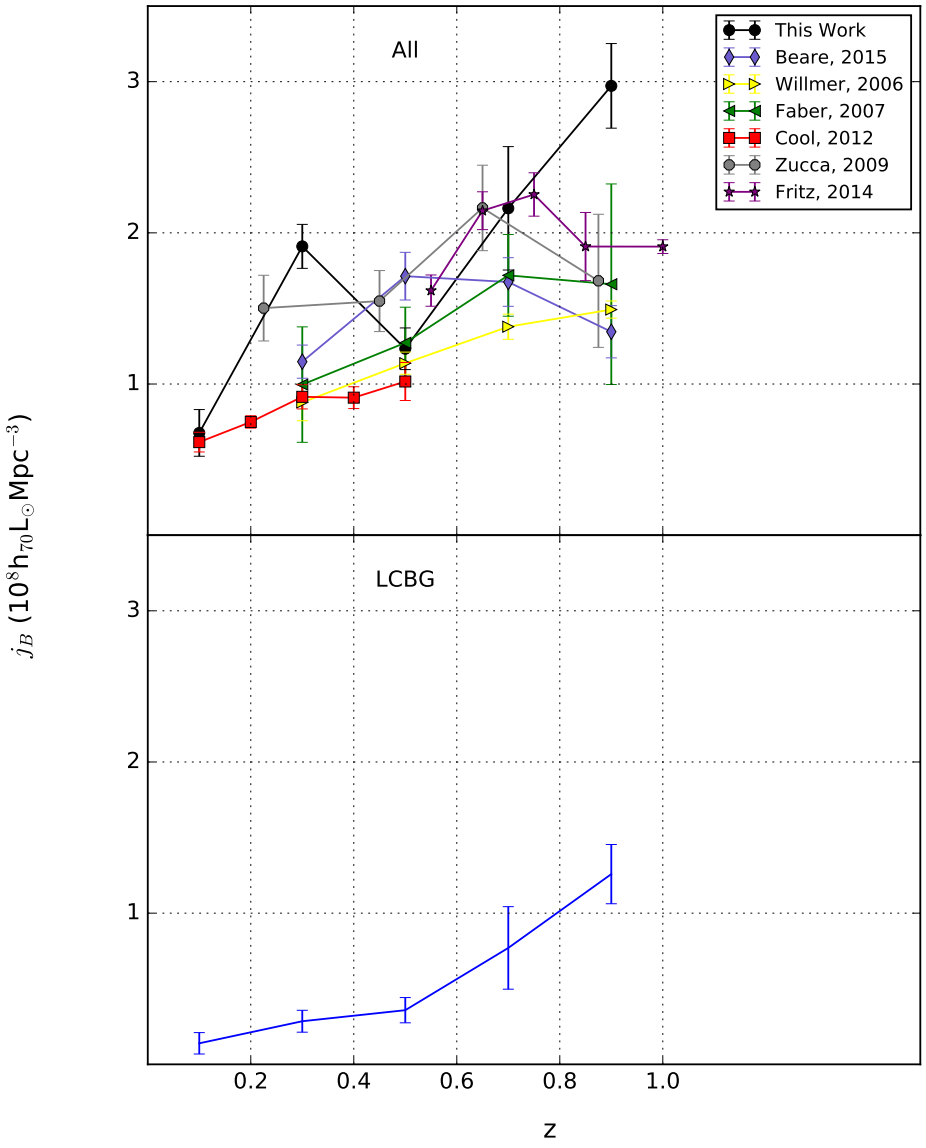

Figure 2.9 Same as Figure 2.7 but for j_B

times the Schechter function. We integrated from M_B=-23.5, where we have a steep drop off in the number of sources in our catalog, to M_B=-18.5, the limiting luminosity in the LCBG selection criteria. With these limits, j_B becomes:

$$j_B = \phi^* L^* (\Gamma(\alpha + 2, L_{M_B=-18.5}) - \Gamma(\alpha + 2, L_{M_B=-23.5})) \tag{2.15}$$

where L^* is the characteristic luminosity calculated from the characteristic magnitude, Γ is the upper incomplete gamma function, and $L_{M_B=x}$ is the luminosity calculated from the absolute magnitude limits defined above. We have plotted luminosity density (j_B) in Figure 2.9. The evolution of j_B we see in our Schechter function fit for the total galaxy sample seems high compared to previous surveys, but the numbers for previous surveys are taken with varying α, which at the highest redshift ranges in each study, is not well determined because there are few faint sources. For a more accurate comparison we look at two previous surveys that have a fixed value of α in their highest redshift bin, Zucca et al. (2009) and Beare et al. (2015). With α fixed at -1.03, as a reminder we find α=-1.05 in our highest redshift bin, Zucca et al. (2009) finds M^*=-21.17±0.04 mag, ϕ^*=(7.2±0.2)×10^{-3} h_{70}^{-3} Mpc^{-3}, and j_B=(2.97±0.12)×$10^8 h_{70} L_\odot Mpc^{-3}$. Beare et al. (2015) finds M^*=-21.19±0.05 mag, ϕ^*=(6.1±0.2)×10^{-3} h_{70}^{-3} Mpc^{-3}, and j_B=(2.7±0.1)×$10^8 h_{70} L_\odot Mpc^{-3}$ with α fixed at -1.1 as opposed to their calculated value of -1.59. Both of these values for luminosity density are consistent with each other and with our value of j_B=(3.0±0.3)×$10^8 h_{70} L_\odot Mpc^{-3}$, when the values for α in each survey are close

We integrate the LCBG luminosity function from M=-∞ to -18.5 to estimate

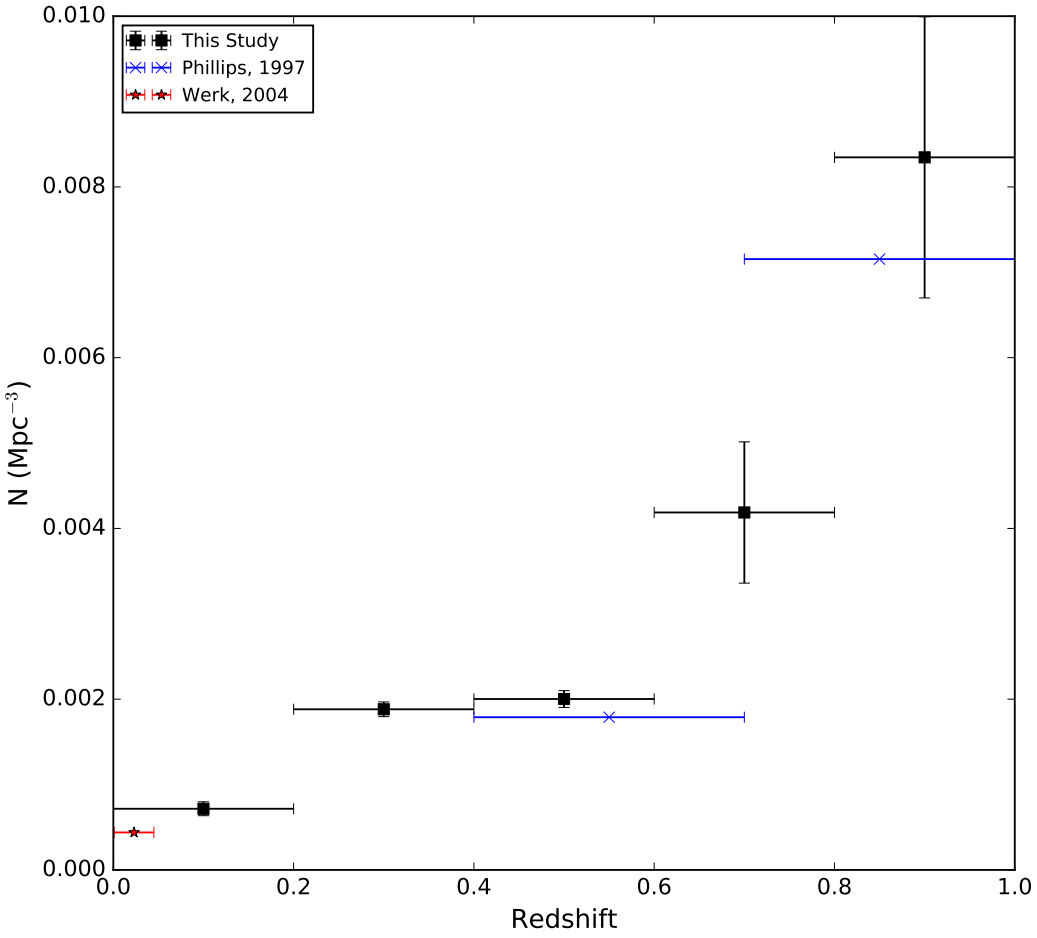

Figure 2.10 Number density of LCBGs in the COSMOS field. Also plotted are the points from Phillips et al. (1997), and Werk et al. (2004)

the evolution of LCBG number density between z=0.0-1.0 and plot that evolution in Figure 2.10. The 1σ error bars were calculated using the *uncertainties* package in Python

At the lowest redshift range in our sample, z=0.01-0.2, the LCBG number density is $7.2\times10^{-4}h_{70}^{3}\mathrm{Mpc}^{-3}$ and at the highest redshift range, z=0.8-1.0, the LCBG number density is $8.3\times10^{-3}h_{70}^{3}\mathrm{Mpc}^{-3}$. This is larger than an order of magnitude increase between z=0.0-1.0, consistent with what was found by Werk et al. (2004). We have plotted the number density of LCBGs versus redshift in Figure 2.10 to more clearly show the evolution. This shows the consistency with Werk et al. (2004), and with Phillips et al. (1997). Figure 2.10 shows the number density slowly increases by a factor of ~ 2 between z=0.01-0.5, then rapidly increases by approximately a factor of four between z=0.5-1.0.

We can also look at LCBGs as a fraction of the total population. This is done in three ways, all plotted in Figure 2.11. Plot (a) shows all LCBGs divided by all galaxies in the G10/COSMOS region. Plot (b) shows the number density of LCBGs divided by the number density of all galaxies brighter than -18.5 calculated by integrating the luminosity function. Plot (c) shows the number density of LCBGs divided by the number density of galaxies brighter than -15. We can see the fraction of LCBGs between z=0 and z=0.2 in plot (a) and (c) match well. This makes sense, as galaxies with M_B=-15 are only detectable in the lower redshift bin of the G10 dataset. The redshift bins between z=0.2 and z=0.8 in plots (a) and (b) match well also. This is because the absolute magnitude limit in the G10 dataset is close to -18.5 in those bins. The final redshift bin in plot (a) showing the fraction of LCBGs in

the G10/COSMOS source catalog, is limited by the photometry to sources brighter than -20.5. Therefore, the fraction should not match plot (b); LCBGs as a fraction of galaxies brighter than M_B=-18.5; nor plot (c), LCBGs as a fraction of galaxies brighter than M_B=-15.

Guzmán et al. (1997) found LCBGs make up (19.3±7.4)% of the galaxy population with I_{F814W} <22.5 between z=0.4-1.0 with the median redshift of z=0.594. The fraction of LCBGs in G10/COSMOS which has an apparent magnitude limit of Subaru i^+=22.5 between z=0.4 and z=0.6 is (26.4±1)%, within 1σ of the value from Guzmán et al. (1997). We have also plotted results from Tollerud et al. (2010) in Figure 2.11. They estimated the fraction of LCBGs to be (11.4±0.8)% also between z=0.4 and z=1 without stating their limiting apparent magnitude. They do note that for their total sample of galaxies the limiting absolute magnitude at z=1 in the R band is -18.5. At z=0.5, roughly their median redshift, their limiting absolute magnitude becomes -16.5. We find LCBGs make up 9.2% of galaxies brighter than M_B <-15 between 0.4≤z≤0.6, which is roughly consistent with the value from Tollerud et al. (2010) at their median redshift of z=0.49.

2.5 Conclusion

We have used data from the G10/COSMOS survey region to trace the evolution of the LCBG population between 0≤z≤1. We have done this by generating the luminosity function of the total galaxy population and of LCBGs in redshift intervals of z=0.2. We have found that the LCBG population appears to evolve as

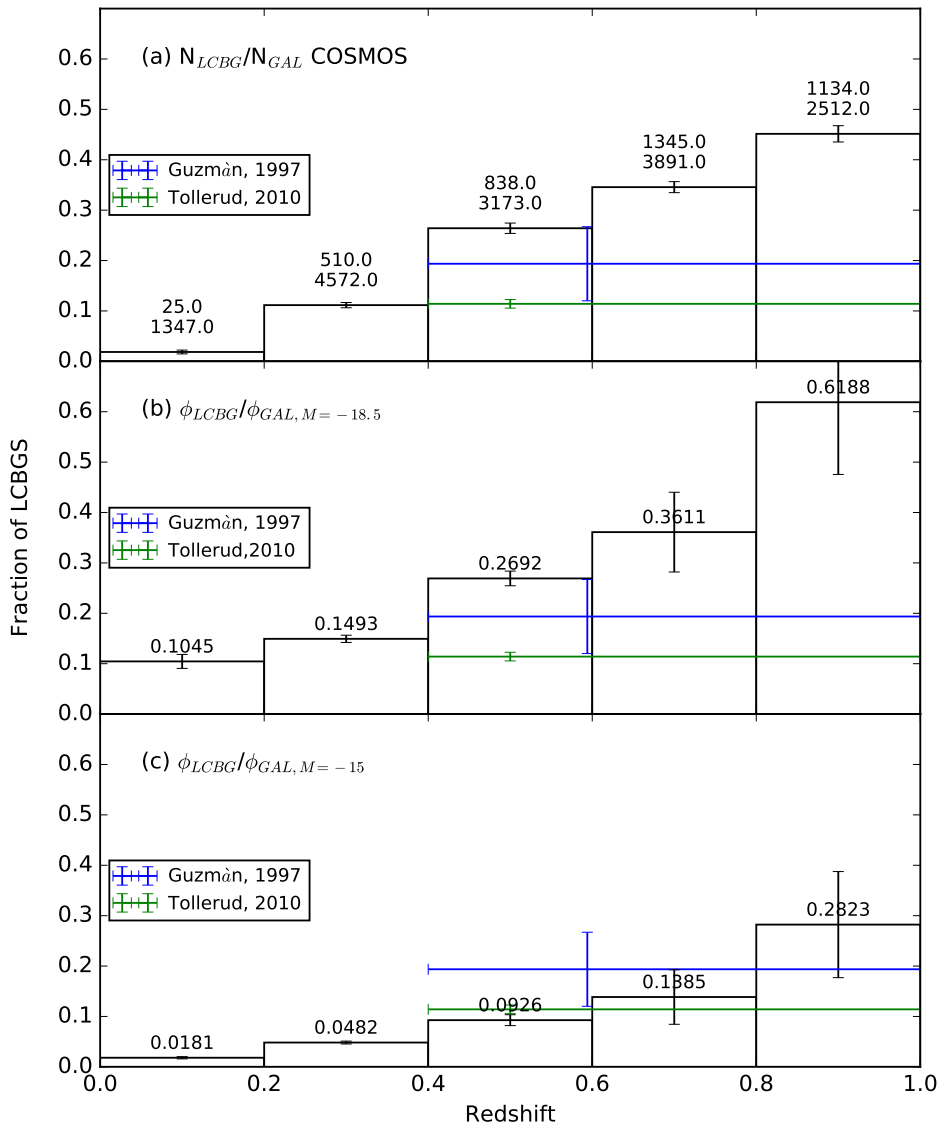

Figure 2.11 Evolution of the fraction of LCBGs in (a) COSMOS (b) integrating both the total sample luminosity function and the LCBG luminosity function to M_B=-18.5 and (c) integrating the total sample luminosity function to M_B=-15. Errors are calculated for number density in the same way as Figure 2.10. We have also included values from Guzmán et al. (1997) and Tollerud et al. (2010) for comparison.

rapidly as previously suggested, with the number density at z=0.9 approximately an order of magnitude larger than that at z=0.1.

We see evolution of $\sim$0.8 mag in M^* and $\sim 6\times10^{-3}\ h_{70}^{-3}$ Mpc^{-3} in ϕ^* both increasing from z=0.1-0.9. Knowing that Schechter parameters are degenerate, and in particular M^* and ϕ^* are dependent on the value of α, we also looked at the evolution of the less degenerate luminosity density. We find that it increases by a factor of 12 between z=0.1-0.9. We also show that LCBGs contribute roughly 42% of the luminosity density of galaxies brighter than M_B=-18.5 at z=0.9. Finally, we can see that LCBGs make up a significant fraction of all galaxies at z=0.9. They make up approximately 30% of the galaxy population brighter than M_B=-15 and 60% of the galaxy population brighter than M_B=-18.5. In the same vein, we see that they make up less than 2% of galaxies in the nearby universe. The rapid change in number density and luminosity density are both consistent with LCBGs being the most rapidly evolving galaxy population between z=0.0-1.0.

Chapter 3

A Study of Luminous Compact Blue Galaxies in the CHILES field[1]

Abstract

We present a study of the evolution of neutral hydrogen content and star formation rates of Luminous Compact Blue Galaxies (LCBGs) using the first 178 hours of data taken on the Very Large Array for the COSMOS HI Large Extragalactic Survey (CHILES). We have detected HI emission from two LCBGs at z=0.045 and z=0.072, and have found that both LCBGs have visible HI companions. We also preformed a stacking analysis of LCBGs in CHILES to constrain the average HI mass of LCBGs out to z=0.428. We have found an upper limit of 2.3×10^9 $M_\odot$ at the average redshift of z=0.239 and 5.6×10^9 $M_\odot$ at the average redshift of z=0.428. Finally we used 1.4 GHz radio continuum emission for CHILES Con Pol, a continuum survey commensal with CHILES, to measure extinction free star formation rates of LCBGs out to z=0.9 using a single homogeneous dataset. We find strong evolution in the star formation rates of LCBGs, and our results match well with previous studies using various star formation rate tracers. Finally we see that LCBGs contribute approximately 45% of the total star formation rate at z=0.9.

[1]Work in this chapter was done in collaboration with D.J. Pisano, The CHILES Team, and the CHILES Con Pol team.

3.1 Introduction

Luminous Compact Blue Galaxies (LCBGs) are a class of vigorously star forming galaxies that are common at z$\sim$ 0.9 but rare locally (Garland et al., 2004). The nature of their evolution is not well understood. Crawford et al. (2016) suggest most intermediate redshift LCBGs in clusters will evolve into dwarf elliptical galaxies based on dimming estimates from stellar evolution models. Crawford et al. (2016) also back up the claim that LCBGs will evolve into dwarf elliptical galaxies using comparisons of star formation and accretion history of dwarf elliptical galaxies in clusters to the predicted evolution of intermediate redshift LCGBs as they move through the cluster environment (i.e. rapid ending of star formation and stripping of material from interaction). Tollerud et al. (2010) found that at intermediate redshifts, some of the more compact LCBGs are a heterogeneous population that will likely evolve into some combination of dwarf elliptical and small disk galaxies. Neutral hydrogen (HI) observations with the Very Large Array (VLA) show LCBGs in the local universe have a variety of gas morphologies but show rotation that is more consistent with disk galaxies than dwarf elliptical galaxies (Rabidoux et al., 2014). Pérez-Gallego et al. (2011) used three-dimensional spectroscopy to generate kinematic maps of local LCBGs and found 48% are rotating disks, 28% show evidence of perturbed rotation, and 24% have complex kinematics with no evidence of disk roatation. We can use HI to trace the kinematics of LCBGs and determine how many are disk-like galaxies, and how many are dwarf elliptical like galaxies. This will help us determine which evolutionary scenario is most likely.

Previous studies of HI in LCBGs have been confined to the local universe due to the weakness of the HI line, the limited frequency coverage of radio telescopes, and strong radio frequency interference (RFI) present in the frequency bands covering redshifted HI emission. Studies of local LCBGs with the Green Bank Telescope (GBT) found that LCBGs are typically gas rich, with median values of $M_{HI} = 5 \times 10^9 M_\odot$ and $M_{HI} L_B^{-1} = 0.4 M_\odot L_\odot^{-1}$ (Garland et al., 2004). Roughly half have mass-to-light ratios approximately 10 times smaller than local galaxies at similar luminosities, confirming that these are small galaxies undergoing vigorous bursts of star formation. Follow up studies using the VLA and GMRT showed the GBT overestimated the HI mass by 66%, because the GBT beam likely contained companion galaxies (Rabidoux et al., 2014). Local LCBGs have an HI depletion timescale of $\tau_g = 3.59 \pm 0.10$ Gyr, roughly the same as local disk galaxies (Kennicutt et al., 1994) indicating this is likely not the last burst of star formation in local LCBGs. A larger statistical sample of HI in LCBGs will provide more kinematic information and allow us to constrain likely evolutionary scenarios. We can also use a larger sample of LCBGs at higher redshift to determine how much fuel is available for star-formation, and, given a star formation rate (SFR), how long LCBGs can sustain their current burst of star formation at different redshifts.

SFRs for LCBGs have been derived using various tracers including the equivalent width of the [O II] line (Phillips et al., 1997; Crawford et al., 2016), Hα emission (Garland et al., 2015), infrared luminosity (Crawford et al., 2016; Garland et al., 2005), and radio continuum (Garland et al., 2005). Garland et al. (2005) found the SFRs from far infrared luminosities for local LCBGs range from 0.4 to 14 $M_\odot$ year^{-1}

with a median of 1.4 $M_\odot$ year^{-1} with the Infrared Astronomical Satellite. They also found star formation rates estimated from the National Radio Astronomy Observatory VLA Sky Survey radio continuum flux are in good agreement with the SFRs estimated from the far infrared luminosities. Phillips et al. (1997) found LCBGs at intermediate and high redshift have SFRs derived from the equivalent width of the [O II] line that match well with the values from Garland et al. (2005), i.e. 0.1 to 14 $M_\odot$ year^{-1}. Crawford et al. (2016) derived SFRs using the equivalent width of the [O II] line and Spitzer 24 μ m infrared flux. They found that in roughly half of their sources, the measurement from the [O II] line was more than two times smaller than the measurement from the infrared line, showing that half of LCBGs have obscured star formation. Specifically, redder LCBGs have measured SFRs that differ between the two methods. Finally, Garland et al. (2015) found SFRs measured from the Hα line in local LCBGs are lower than SFRs of LCBGs at intermediate redshift.

Below we use data products from the COSMOS HI Large Extragalactic Survey (CHILES) and CHILES Con Pol (CCP; a commensal continuum survey) to study HI emission and SFRs for LCBGs. We will use the single emission line data set to determine the HI masses of LCBGs between z=0.05-0.45, and the radio continuum data from CCP to determine extinction free SFRs between z=0.05-1.0. Throughout this chapter we use cosmological parameters H_0=70 km s^{-1} Mpc^{-1}, $\Omega_M = 0.3$, $\Omega_\Lambda = 0.7$ and we use the Vega magnitude system. In section 3.2 we describe our sample selection, data products and data reduction. In Section 3.3 we discuss the methods used to stack our extracted HI spectra and in Section 3.4 we discuss how we calculated the SFR.

3.2 Sample Selection, Data, and Reduction

3.2.1 Sample Selection

In Chapter 2 we selected LCBGs in the COSMOS field using the selection criteria, M_B $\leq$-18.5 mag, $\mu_e(B)$ $\leq$21 mag arcsec^{-2}, and (B-V)$_0$ $\leq$0.6 mag (Werk et al., 2004). For this study we selected sources from the COSMOS field that lie within the CHILES survey region, a circular region within a 25' radius of right ascension α=150.351 deg and declination δ=2.35 deg. We found 2112 LCBGs within 25' of the CHILES pointing center between z=0.0-1.0, 364 of which are in the redshift range of z=0.0-0.45.

3.2.2 Observations

The first epoch of CHILES observations was a total of 178 hours, with 143 being on source, over 44 observing sessions using the VLA. The observations were carried out between 25 October, 2013 and 21 January, 2014 in the VLA's B-array configuration. The VLA allows for two 1 GHz basebands. The CHILES spectral line survey used 15 windows with 32 MHz bandwidth per window. Each window had 2048 channels and dual polarization. This was done on the first baseband and provided an initial frequency resolution of 0.016 MHz per channel. Observations were taken with three separate subband setups, each offset by approximately 10 MHz to stop the drop in sensitivity at the ends of each subband from occurring at the same frequency. This method, known as frequency dithering, is used to gain continuous frequency coverage from 970-1430 MHz. The pointing center for the

observations, mentioned above is α=150.351° and δ=2.35°. The primary beam size (FWHM) for the VLA is calculated as 45'/ν_{GHz} or 31.7 arcmin at 1420.406 MHz and 46.39 arcmin at 970 MHz. We observed 3C286 as a flux calibrator and J0943-189 as a phase calibrator.

The other baseband was used to take commensal observations for CCP, a continuum survey using 4 windows with 128 MHz bandwidth per window and full polarization. Each window had 64 channels for a 2 MHz channel resolution. The four windows used for CCP cover the frequencies 1000-1128 MHz, 1384-1512 MHz, 1640-1768 MHz, and 1768-1896 MHz.

3.2.3 Spectral Line Data Reduction and Imaging

The spectral line data was reduced following standard procedures including flagging, calibration and imaging. The standard VLA continuum pipeline was modified[2] to work with spectral line data. The pipeline was written using version 4.1 of the Common Astronomy Software Applications package (CASA)[3], to effectively flag and calibrate the data while limiting the need for human interaction. The pipeline convertsed the data to the CASA Measurement Set (MS) format, and automatically flagged times where the telescope may have malfunctioned or the data was otherwise unusable. The pipeline then generated initial calibrations on the flux calibrator, flagged the flux calibrator using *flagdata* in the *RFLAG* mode in two iterations. Then the pipeline generated delay and bandpass calibrations and flagged

[2]Work was done by E. Momjian, with significant contribution from X. Fernandez, and H. Gim
[3]http://casa.nrao.edu

them again with two iterations of *flagdata*. Calibrations were again generated for the bandpass and delay calibrators and a solution interval was determined. Next, the pipeline fit the spectral index to the flux calibrator and generated the final calibration tables. Then the pipeline applied the calibration tables to the observations of the targeted COSMOS field. Finally *flagdata* is run twice on the target to remove RFI. After the pipeline was run, the data was manually checked, and if the pipeline missed any RFI, it was manually flagged and the pipeline was run again to carry out the calibration steps.

Spectral line image cubes were generated for the entire frequency range. More details can be found in Fernández et al. (2016).

3.2.4 Continuum Data Reduction, Imaging

The radio continuum observations were split from the spectral line data and reduced and imaged separately. The data were processed and imaged with a custom pipeline developed by Chris Hales (Hales et. al, in prep) following standard calibration procedure, using *pieflag* (Hales & Middelberg, 2014) to flag and calibrate data. Simple imaging was done taking into account non-coplanar effects, but without self-calibration or A-projection. The final noise in the image was 3 μ Jy and the average frequency was 1.477 GHz.

3.2.5 Radio Continuum Sample

The 20 cm continuum flux was calculated from the CCP 180 hour continuum image (Hales, in prep) using Blobcat[4] software (Hales et al., 2012). Blobcat is a software package developed in Python designed to select sources from a 2-d total intensity radio continuum image. Sources in this case could be individual galaxies, or blended emission from multiple galaxies. Blobcat was set to select sources with flux seven times the local noise near the sources, where the noise in the center of the image is 3 μJy. Blobcat found 1136 objects that meet this criteria.

3.3 HI Stacking

Spectral line stacking is a technique that combines spectrum of a number of galaxies centered on the sought after spectral line. It can be used to find the average HI mass of numerous galaxies that are not detected in the survey. To do this, we follow the method outlined in Rhee et al. (2013, 2016) and described below. The spectra were extracted from the data cubes in a circular region around the source center. The circular region was generated to have a 35 kpc radius in the objects' rest frames. The extracted spectrum was 120 channels, or $\sim$8 MHz, in width. After extraction, all spectra were corrected for primary beam attenuation. We assumed the primary beam pattern of the VLA was a two dimensional circular Gaussian, characterized as:

[4]http://blobcat.sourceforge.net/

$$gain = e^{-4ln(2)(d/\theta)^2} \ , \ \theta = \frac{45'}{\nu_{GHz}} \tag{3.1}$$

where ν is the observing frequency, Θ is the half power beam width, and d is the angular separation from the field center in arcminutes[5].

After we corrected for the primary beam, we shifted the spectrum to the same rest-frame velocity then matched the the rest frame velocity width by convolving the spectrum with a boxcar function whose width is $v_{smoothed}/v_{unsmoothed}$. The spectrum were then combined using a weighted average, defined as:

$$\Big\langle S \Big\rangle = \frac{\sum_i w_i' S_i'}{\sum_i w_i'} \ , \ w_i = \frac{1}{\sigma_i'} \tag{3.2}$$

where S_i' is the spectrum with the primary beam correction applied, and σ_i is the noise per channel with the primary beam correction applied. We broke our sample into four ranges of approximately 100 sources each. The ranges are 980.1-1013.9 MHz (z=0.4-0.45), 1015.3-1052.07 MHz (z=0.35-0.4), 1052.7-1091.7 MHz (z=0.3-0.35), and 1092.9-1276.2 MHz (z=0.1-0.3).

The averaged spectrum can be used to find the co-added flux, and an estimated HI mass or an upper limit for each redshift range. We can compare this average mass to the average mass from local studies of HI in LCBGs.

[5]Primary beam information for the VLA can be found at https://science.nrao.edu/facilities/vla/docs/manuals/oss2016A/performance/fov/pbeam

Errors are estimated using jackknife resampling (Efron & Stein, 1981). We construct jackknife samples of the co-added spectrum from the total set, X=$(x_1, x_2, \ldots, x_n)$, by removing one spectrum. This leaves us with as many jackknife samples as spectrum in the set. The jackknife sample is defined as:

$$X_i = x_1, x_2, \ldots, x_{i-1}, x_{i+1}, \ldots, x_n \tag{3.3}$$

The ith partial coaded spectrum is then defined as:

$$\hat{\alpha_i} = f\left(X_i\right) \tag{3.4}$$

The pseudo values then become:

$$\hat{\alpha_i^*} = n\hat{\alpha} - (n-1)\,\hat{\alpha_i} \tag{3.5}$$

where $\hat{\alpha}$ is the co-added spectrum. The error then becomes:

$$(\sigma^*)^2 = \frac{1}{n\,(n-1)} \sum_i \left(\hat{\alpha_i^*} - \hat{\alpha^*}\right)^2 \;,\; \hat{\alpha^*} = \frac{1}{n} \sum_i^n \hat{\alpha_i^*} \tag{3.6}$$

We use this error on the flux to estimate the error in HI mass.

3.4 Star Formation Rates

20 cm continuum emission in galaxies is dominated by non-thermal synchrotron radiation, radiation from electrons that are accelerated by magnetic field lines. We therefore ignore thermal emission at these wavelengths. In galaxies without active galactic nuclei (AGN), most synchrotron emission comes from electrons in massive star (Type II) supernova remnants as they begin to interact with the surrounding interstellar medium. This emission then allows us to trace the rate of supernovae in these galaxies. Since all stars larger than 8 $M_\odot$ will eventually become supernova, we can link the supernova rate to the number of massive, short-lived stars that have recently been formed in a given galaxy using an initial mass function (IMF). From Condon (1992) the relation is:

$$\frac{\nu_{SN}}{yr^{-1}} = \int_{8M_\odot}^{100M_\odot} \psi(M) dM \tag{3.7}$$

where ν_{SN} is the supernova rate and ψ is the IMF. We use the IMF derived by Kroupa (2001) to directly compare with Rabidoux (2015). Kroupa (2001) has a power law slope of α=-2.3 for objects larger than 0.5 $M_\odot$ so the supernova rate becomes:

$$\frac{\nu_{SN}}{yr^{-1}} = \int_{8M_\odot}^{100M_\odot} \text{k M}^{-2.3} dM \tag{3.8}$$

where k is a constant with units yr^{-1}. This results in a supernova rate ν_{SN}=k×0.05 $\text{M}_\odot$. The IMF will tell you approximately how many stars are created per year, so to determine the total mass generated per year we multiply both sides of the above equation by mass to get the SFR in $\text{M}_\odot\ \text{yr}^{-1}$ for stars greater than 0.1 $\text{M}_\odot$:

$$\frac{SFR}{M_\odot yr^{-1}} = \int_{0.1M_\odot}^{100M_\odot} M\psi(M) dM \tag{3.9}$$

The Kroupa (2001) IMF has a varying slope to the power law dependent on mass, so to calculate SFR we evaluate

$$\frac{SFR\,(M > 0.1M_\odot)}{M_\odot yr^{-1}} = \int_{0.1M_\odot}^{0.5M_\odot} \text{k M M}^{-1.3} dM + \int_{0.5M_\odot}^{100M_\odot} \text{k M M}^{-2.3} dM \tag{3.10}$$

Evaluating this, we find the total SFR is SFR/($\text{M}_\odot\ \text{yr}^{-1}$)=k×3.86 $\text{M}_\odot$. Since k is constant we can set k in our SFR equal to k in our supernova rate. From this we find:

$$\frac{SFR\,(M > 0.1M_{\odot})}{M_{\odot}yr^{-1}} = 77.8\frac{\nu_{SN}}{yr^{-1}} \tag{3.11}$$

From Condon & Yin (1990), the observed relation for the supernova rate and the radio continuum luminosity is:

$$\frac{L_N}{WHz^{-1}} = 13 \times 10^{22} \left(\frac{\nu}{GHz}\right)^{\alpha} \left(\frac{\nu_{SN}}{yr^{-1}}\right) \tag{3.12}$$

where L_N is the radio continuum flux in W m^{-1} Hz^{-1} multiplied by the luminosity distance D_L^2 in m^2, and ν is the rest frequency. If we use Equation 3.13 to substitute for ν_{SN} we find the SFR is

$$\frac{SFR\,(M > 0.1M_{\odot})}{M_{\odot}yr^{-1}} = 5.99 \times 10^{-22} \left(\frac{\nu}{GHz}\right)^{\alpha} \left(\frac{L_N}{WHz^{-1}}\right) \tag{3.13}$$

We must account for changes in observed properties with redshift through k-corrections when calculating luminosity using equation:

$$\frac{L_N}{WHz^{-1}} = \left(\frac{4\pi\ D_L^2}{(1+z)^{1+\alpha}}\right) \times\ S_{obs} \tag{3.14}$$

Where S_{obs} is the observed flux density in Jy, D_L is the luminosity distance. The correction, $(1+z)^{1+\alpha}$ is a combination of two corrections. The first, $1/(1+z)$, accounts for the change in bandpass size, the second, $1/(1+z)^{\alpha}$, corrects from the observed frequency to the rest frequency.

3.4.1 Avoiding AGN Contamination

AGN, bright sources believed to be emission from accretion of material onto a supermassive black hole (Kazanas et al., 2012), can also be strong emitters of non-thermal radio continuum flux that can wash out emission from Type II supernova. We must only select sources without AGN emission to get an accurate measurement of the SFR in LCBGs

To do this we matched sources from the CCP catalog to sources in the optical catalog. We only used radio continuum sources that were within 1" of an optical source. If the CCP source matched an optical source with strong x-ray emission, sometimes indicative of AGN activity, we excluded that source from our study. We also matched the CCP sources to sources in the VLA 3GHz COSMOS survey (Smolčić et al., 2017b) which did a multi-wavelength analysis of all of their sources to search for evidence of AGN. If a CCP source was matched to a 3 GHz source that was flagged as an AGN we excluded it from our study. If a CCP source was matched to an optical source, but not matched to a 3 GHz source we still included it in our study. Criteria for AGN in the 3 GHz can be found in Section 6 of Smolčić et al. (2017c)

α (J200)	δ (J200)	redshift	M_B (mag)	R_e (kpc)	R_{HI} (kpc)	$\log_{10}(M_{HI})$ ($M_\odot$)	W_{20} (km s^{-1})
150.23	2.396	0.045	-21.3	3.07	8.98	9.62	316±26
150.265	2.515	0.072	-20.4	3.09	12.2	10.1	213±28

Table 3.1 HI properties of two LCBGs detected in CHILES. HI for both sources includes HI from companions.

We were able to match 431 sources in the CCP catalog to an optical counterpart with a robust redshift in the range z=0.0-1.0. Of those 431 sources, 106 were LCBGs. Strong and weak AGN emission was present in 217 of the sources, and 44 of those were LCBGS, leaving us with 214 sources, 62 of which are LCBGs

3.5 Results and Discussion

3.5.1 HI Detections

We searched the spectral line cubes for all 364 LCBGs in the CHILES volume. We used scaling relations from Dénes et al. (2014) which relates radius and absolute magnitude to HI mass from HIPASS, to estimate the HI mass of each source. To determine the noise level required for a detection we used:

$$\sigma_{req} = \frac{M_{HI}(1+z)}{2.36 \times 10^5 D_L^2 dv \sqrt{N} \sigma_{SNR}} \tag{3.15}$$

where σ_{req} is the noise level required, M_{HI} is estimated HI mass from the scaling relations in $M_\odot$, D_L is the luminosity distance to the source, dv is the velocity width of a single channel, N is the number of channels for if the HI line

width is 200 km s^{-1} (Papastergis et al., 2011), and σ_{SNR}=3 is the signal to noise ratio we would consider a detection. We can reasonably expect to detect any object with σ_{req} greater than the average noise per channel 75μJy $beam^{-1}$. Based on this we expected to detect 13 of the 364 sources, and did detect 2. The other 11 were not significant detections, likely because the mass estimates were higher than the actual HI mass.

We detect the LCBGs J100055.2+022343 at z=0.045 and J100103.7+023053 at z=0.072. The HI image for J1000055.2+022343 shows the HI extending to a companion in the north east part of the image. The companion is located at α=150.234° and δ=2.398°. The GAMA catalog only has a photometric redshift z=0.703, but based on HI must be located at z$\sim$0.04. The HI also extends to the north west and the maximum HI contour is not centered on the optical image of the galaxy. The optical image of J1000055.2+022343 appears to be a Sa type spiral galaxy with diffuse gas throughout.

The HI image for J100103.7+023053 shows the HI extending to a companion in the west part of the image. The companion is located at α=150.26° and δ=2.514°. The GAMA catalog lists the photometric redshift to the companion of z=0.2, but based on HI must be located at z$\sim$0.07. The HI also appears to be disturbed. The optical image of J100103.7+023053 appears to be a Sb type spiral galaxy.

Rabidoux et al. (2014) studied HI in nine LCBGs at $D \lessapprox 80$ kpc. They found the HI mass ranged from $8.5\times10^{8}M_{\odot}$ to $1.1\times10^{10}M_{\odot}$ with an average of $2.98\times10^{9}M_{\odot}$. They found eight of their nine LCBGs had nearby companions or disturbed morphology indicative of past interaction. Our two sources fall within

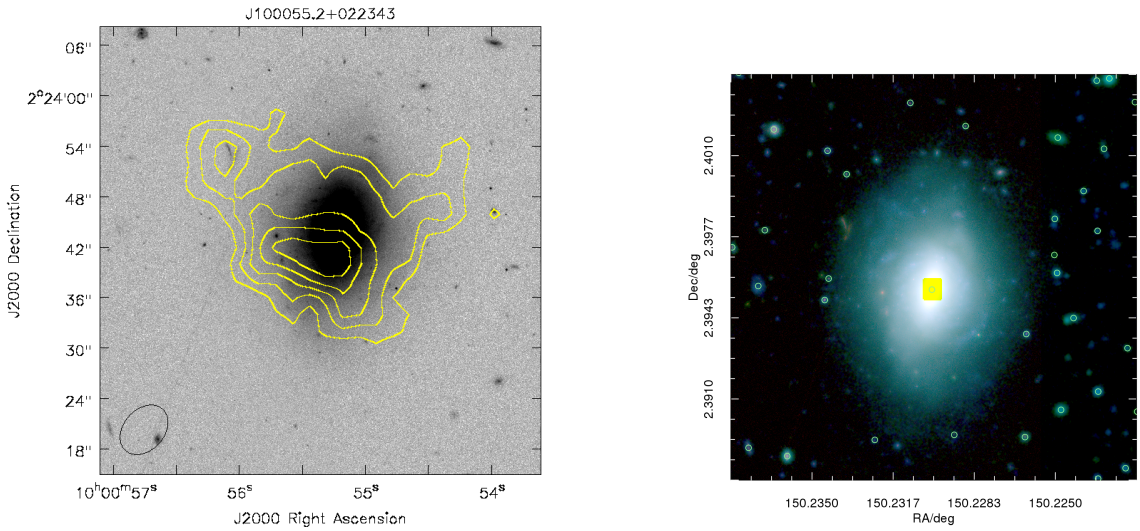

Figure 3.1 (left) Moment 0 map overlaid on I_{F814W} on left. Column density contours are (0.58), (0.87), (1.2), (1.5), (1.8)$\times 10^{21}$ cm^{-2}. HI contours are clearly visible around a companion in the right part of the image. (right) Image from GAMA cutout tool with Subaru B in blue, Subaru r in green, and I_{F814W} in red.

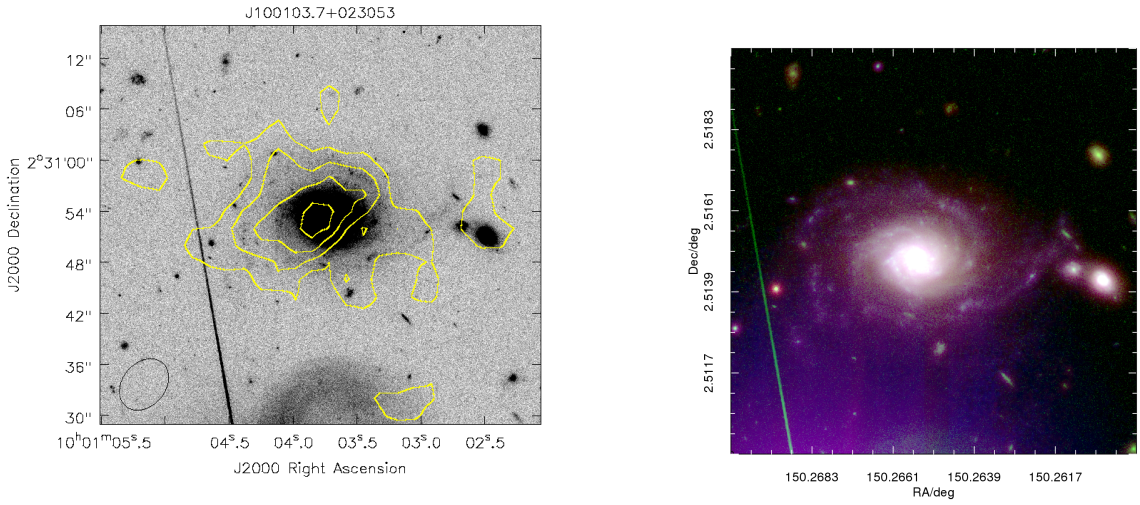

Figure 3.2 (left) Moment 0 map overlaid on I_{F814W} on left. Column density contours are (0.61), (0.92), (1.2), (1.5)$\times 10^{21}$. HI contours are clearly visible around a companion in the right part of the image. (right) Image from GAMA cutout tool with Subaru B in blue, Subaru r in green, and I_{F814W} in red.

their range, and both have companions. We only have two detections so we will use stacking to determine how the average HI mass of LCBGs evolves over redshift.

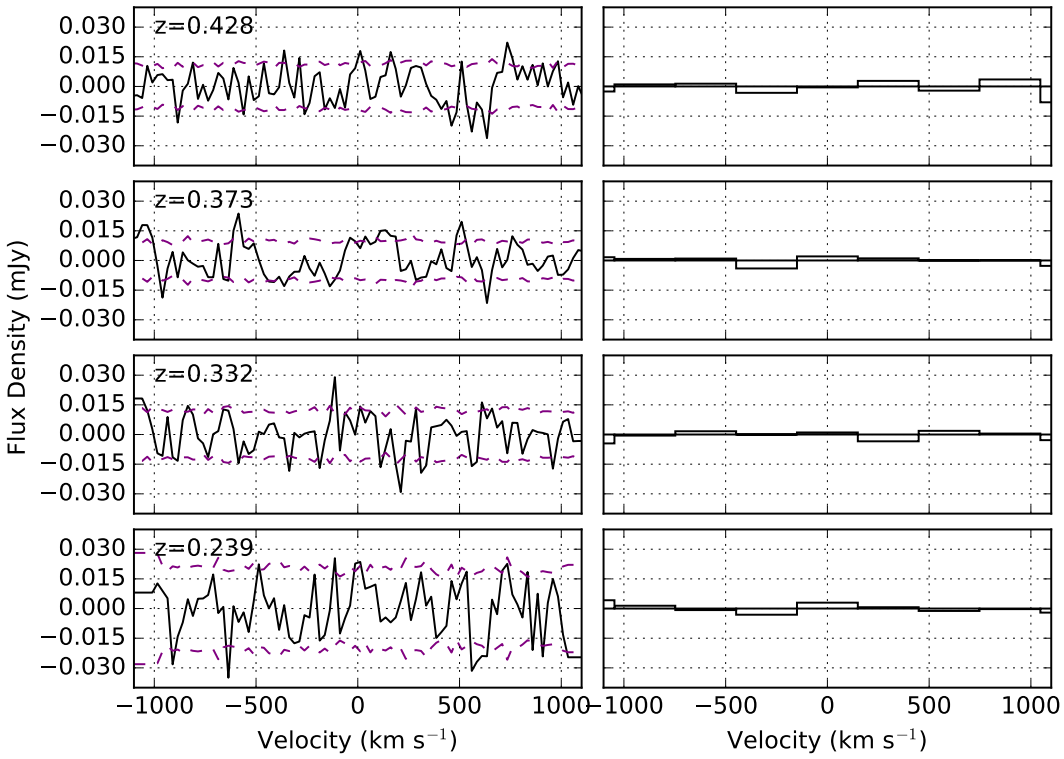

Figure 3.3 This shows the stacked HI signal in redshift bins z=0.4-0.45, z=0.35-0.4, z=0.3-0.35, and z=0.15-0.3. The purple dashed line represents the 1σ error estimated from jackknife sampling.

3.5.2 HI Mass Limits

We stacked 86 galaxies between z=0.4-0.45, 111 galaxies between z=0.35-0.4, 91 galaxies between z=0.3-0.35, and 74 galaxies between z=0.15-0.3 Figure 3.3 shows the stacked spectrum with The left side showing flux vs rest frame velocity smoothed to 25 km s^{-1}, and the right side showing the flux vs rest frame velocity smoothed to 300 km s^{-1}. We smooth to 300 km s^{-1} to match the median HI line width of 200 km s^{-1} from ALFALFA (Papastergis et al., 2011) and the error in redshift of $\sim$110 km s^{-1} in zCOSMOS spectra (Lilly et al., 2009). We then calculate the 5σ upper limit using:

redshift	N	5σ upper lim 10^9 $M_\odot$
0.239	86	2.3
0.332	111	3.6
0.373	91	4.21
0.428	74	5.57

Table 3.2 The properties of the stacked HI spectrum of LCBGs in CHILES. The first column shows the average redshift of all sources included in the stacked spectrum, N is the number of sources included in the stacked spectrum, and the upper limit is calculated as the 5σ upper limit

$$\sigma_{MHI} = \frac{2.36 \times 10^5 D_L^2 \sigma_s dv \sqrt{N} \sigma_{SNR}}{(1+z)\mu} \tag{3.16}$$

where σ_{MHI} is the upper limit of the neutral hydrogen mass, D_L is the luminosity distance in Mpc, σ_s is the error estimated from jackknife resampling in units of of Jy, dv is the channel width in km s^{-1} which for our spectra is 25 km s^{-1}, N is the number of channels the galaxy would span where we still assume a width of 300 km s^{-1} with 25 km s^{-1} channels for N=12, σ_{SNR} is the signal to noise ratio of five, and z is redshift. Our limits are listed in Table 3.5.2. Three limits are still higher than the average LCBG HI mass of 2.98×10^9 derived from Garland et al. (2015). The stack of spectra at z=0.239 has a 5σ upper limit of 2.3×10^9, lower than the local average HI mass in LCBGs. It is possible we do not have a significant detection at because of strong RFI, especially around between z=0.15-0.25

These upper limits are set from the first 178 hours of observation. We can continue to process data as the survey continues until we observe the full 1000 hours, in order to directly detect a larger number of LCBGs, and measure the average HI

mass in higher redshift LCBGs. The second epoch of observations for example, will add another 211 hours of observation time. This epoch is currently being processed and will be added to the first 178 hours to be imaged, making the noise roughly 30 percent lower, and increasing the number of detections and improving stacking limits.

3.5.3 LCBG Star Formation Rates

We have calculated SFR using equation 3.13, and the results are listed in Table 3.5.3. SFR for these sources range from 0.72-127 $M_\odot$ yr^{-1}. We calculate the error in the SFR from the error in the flux, and allowing for variation in the non-thermal spectral index, α, from equation 3.13. The spectral index is approximately 0.8 (Condon, 1992), but we allow it to vary, from 0.6 to 1.0. The minimum SFR detectable in the catalog was determined by calculating the SFR of the source with the lowest flux density at all redshifts between z=0.0-1.0

The average SFR in each bin, centered at the median redshift of the sample, is shown in Figure 3.4. The error bars show the standard deviation of the sample. and indicate there are a wide range of SFRs at each redshfit. The total range is also shown in Table 3.5.3. Our data shows an increase in total SFR from LCBGs as redshift increases. The average SFR at z=0.92 is $\sim$ 25 times higher than the average star formation rate at z=0.12. We showed in Chapter 2 the number density of LCBGs is evolving, and we see here the average star formation rate of LCBGs is evolving as well.

G10 ID	α (J2000)	δ (J2000)	z	M_B (mag)	R_e (kpc)	SFR(1.4GHz) ($M_\odot$ yr^{-1})
6008788	150.230	2.395	0.045	-20.950	2.912	0.717 ± 0.063
6327239	150.265	2.515	0.071	-20.217	2.880	2.472 ± 0.205
6001903	150.329	2.370	0.171	-19.319	1.992	2.489 ± 0.227
6013566	150.211	2.459	0.190	-20.024	2.779	2.296 ± 0.295
6003517	150.457	2.235	0.221	-19.849	2.239	3.649 ± 0.390
6019746	150.459	2.414	0.268	-20.503	3.047	4.737 ± 0.502
6019764	150.500	2.405	0.269	-20.335	2.609	7.546 ± 0.640
6003502	150.413	2.279	0.307	-21.285	4.053	29.094 ± 1.696
6005714	150.231	2.437	0.312	-20.573	2.903	7.255 ± 0.714
6000784	150.516	2.123	0.337	-20.808	3.924	15.926 ± 1.543
6005346	150.171	2.238	0.339	-21.895	4.878	11.654 ± 1.079
6005198	150.235	2.280	0.361	-20.764	3.705	9.225 ± 0.894
6001324	150.299	2.222	0.374	-20.934	3.792	14.853 ± 1.117
6003560	150.286	2.284	0.415	-20.902	3.677	11.763 ± 1.064
6012905	150.491	2.174	0.431	-20.870	3.274	14.614 ± 1.644
6018052	150.332	2.242	0.446	-21.307	4.797	21.700 ± 1.506
6020196	150.276	2.369	0.467	-20.813	3.542	16.466 ± 1.346
6020067	150.229	2.440	0.468	-21.614	4.352	25.354 ± 1.795
6018168	150.305	2.181	0.499	-21.360	3.990	13.065 ± 1.678
6018167	150.339	2.182	0.501	-22.430	6.360	29.084 ± 2.107
6014015	150.401	2.464	0.502	-21.064	3.829	34.164 ± 2.174
6005672	150.421	2.344	0.517	-20.791	3.197	7.965 ± 1.329
6020003	150.397	2.309	0.518	-21.112	4.564	9.378 ± 1.345
6002350	150.319	2.623	0.527	-21.630	4.297	23.380 ± 3.037
6273846	150.403	2.317	0.536	-21.268	4.845	24.619 ± 1.827
6005667	150.503	2.356	0.553	-20.733	2.903	35.963 ± 2.521
6019402	150.600	2.427	0.595	-21.666	5.599	28.192 ± 3.512
6014084	150.271	2.501	0.610	-22.222	2.685	38.233 ± 2.965
6014095	150.374	2.507	0.618	-20.918	1.714	23.487 ± 2.476
6019756	150.403	2.409	0.632	-20.031	2.649	13.234 ± 1.965
6017817	150.452	2.216	0.636	-20.074	2.200	14.870 ± 2.456
6018300	150.218	2.246	0.656	-21.931	4.372	30.127 ± 2.947
6001279	150.396	2.207	0.671	-21.466	4.506	25.469 ± 2.781
6022936	150.160	2.474	0.672	-21.508	4.705	56.468 ± 4.540
6019729	150.457	2.418	0.676	-21.489	4.601	63.565 ± 4.225
6020133	150.246	2.405	0.682	-21.322	4.424	25.898 ± 2.684
6022720	150.186	2.558	0.687	-22.378	5.674	44.919 ± 4.871
6003806	150.175	2.371	0.688	-21.598	5.145	22.155 ± 3.002
6001263	150.495	2.260	0.701	-22.347	5.980	29.885 ± 3.251
6002397	150.264	2.542	0.703	-22.715	8.607	83.173 ± 5.787
6002408	150.275	2.523	0.716	-22.283	3.164	44.608 ± 4.009

G10 ID	α	δ	z	M_B	R_e	SFR(1.4GHz)
6003775	150.353	2.342	0.742	−21.072	3.008	17.137 ± 2.489
6003784	150.335	2.319	0.750	−20.671	2.292	15.750 ± 2.517
6013454	150.294	2.402	0.797	−21.400	2.983	19.724 ± 2.980
6017806	150.508	2.220	0.816	−20.818	2.095	43.611 ± 4.966
6014112	150.294	2.476	0.819	−21.502	1.872	25.940 ± 3.644
6014099	150.371	2.498	0.821	−22.373	6.961	40.484 ± 4.270
6001939	150.093	2.450	0.838	−20.856	3.228	55.976 ± 7.273
6003508	150.471	2.262	0.847	−21.212	3.084	31.855 ± 4.126
6010663	150.535	2.450	0.872	−21.981	4.393	37.482 ± 5.328
6013999	150.553	2.486	0.874	−21.102	3.909	61.448 ± 6.988
6013435	150.351	2.435	0.879	−22.426	6.603	52.602 ± 4.870
6008228	150.311	2.243	0.890	−21.837	6.600	32.536 ± 4.164
6003789	150.373	2.301	0.894	−21.732	5.809	28.141 ± 3.741
6001920	150.229	2.316	0.897	−21.963	4.195	28.876 ± 4.164
6223721	150.520	2.265	0.923	−22.673	7.386	50.327 ± 5.955
6001874	150.394	2.445	0.925	−21.614	3.257	62.319 ± 5.812
6022180	150.382	2.617	0.927	−22.385	6.610	101.088 ± 10.186
6021988	150.439	2.543	0.951	−21.262	1.546	102.001 ± 9.372
6003804	150.225	2.380	0.977	−22.204	5.302	40.252 ± 5.198
6004004	150.468	2.464	0.981	−21.943	3.276	37.112 ± 5.487
6019510	150.608	2.340	0.986	−22.193	4.312	127.496 ± 12.280

Table 3.3 SFRs calculated using Equation 3.13. SFRs for these sources range from 0.7-127 $M_\odot$ yr^{-1}. The spectral index is approximately 0.8 (Condon, 1992), but we allow it to vary, from 0.6 to 1.0. The minimum SFR detectable in the catalog was determined by calculating the SFR of the source with the lowest flux density at all redshifts between z=0.0-1.0

redshift	N	median	$\langle SFR \rangle$	range	Minimum SFR
0.12	4	2.38	1.99±0.73	0.717-2.49	0.34
0.31	9	9.22	11.5±7.23	3.65-29.1	2.87
0.50	14	22.5	21.1±8.58	7.96-36.0	7.4
0.68	17	25.9	33.5±18.6	13.2-83.2	13.3
0.92	18	42.0	53.3±27.6	25.9-127	20.45

Table 3.4 Showing number of LCBGs in each bin, median and average SFR, the range in SFR, and the minimum SFR at the redshift listed. Note, the lowest SFR in the bin can be lower minimum SFR at the center of the bin.

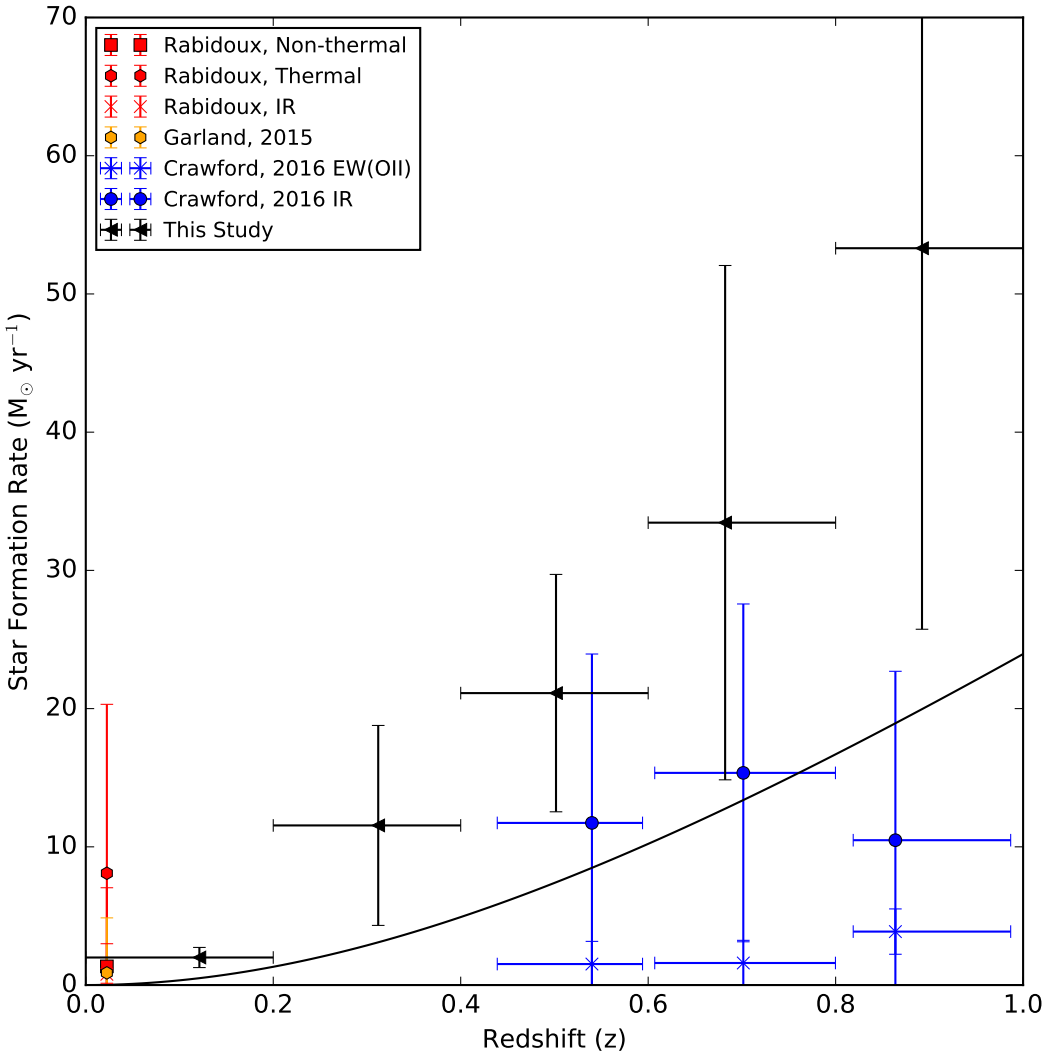

Figure 3.4 The blue line shows the minimum SFR detectable at an redshift based on the noise in the cube. The black points show the average LCBG SFR calculated in this study. We plot local SFRs from Rabidoux (2015) using both thermal and non-thermal radio continuum estimators. We also plot SFRs for objects at intermediate redshift calculated using the [O II] equivalent width and the far infrared flux.

Our average non-thermal radio continuum SFRs are higher but still within one standard deviation of the average far infrared SFRs from Crawford et al. (2016) in all redshift bins but the last. Crawford et al. (2016) measured SFRs for cluster and field LCBGs. The average SFR plotted from Crawford et al. (2016) in Figure 3.4 combines the two samples at each redshift bin to make one sample. The difference in the last bin could partially be due to our sensitivity limits, with the average from Crawford et al. (2016) being lower than the minimum SFR detectable. It could also be because Crawford et al. (2016) only has 9 detections in IR and two of those have higher star formation rates estimated from [O II] equivalent width than from IR. We are still seeing higher star formation rates at high redshift.

For the other two bins, we expect to get similar SFR statistics. There is a strong correlation between the far-infrared (FIR) luminosity and 1 GHz luminosity for galaxies, known as the FIR-radio correlation. This is likely because they are both tracing the same population of stars while generally not being susceptible to obscuration. The FIR emission is coming from interstellar dust being heated by massive stars, while the radio continuum emission is synchrotron emission from relativistic electrons emitted by supernova as mentioned above. It is likely that as we become more sensitive to objects with lower SFRs, the average SFR in the bins overlapping Crawford et al. (2016) will become closer to their values.

In Figure 3.5 we have plotted the the total SFR of LCBGs over the total SFR of the from galaxies detected in CCP $i^+ \leq 22.5$ between z=0.0-1.0. We see similar to the number density of LCBGs found in Chapter 2, the fraction of SFR contributed by LCBGs increases rapidly to z=1. Guzmán et al. (1997) found LCBGs

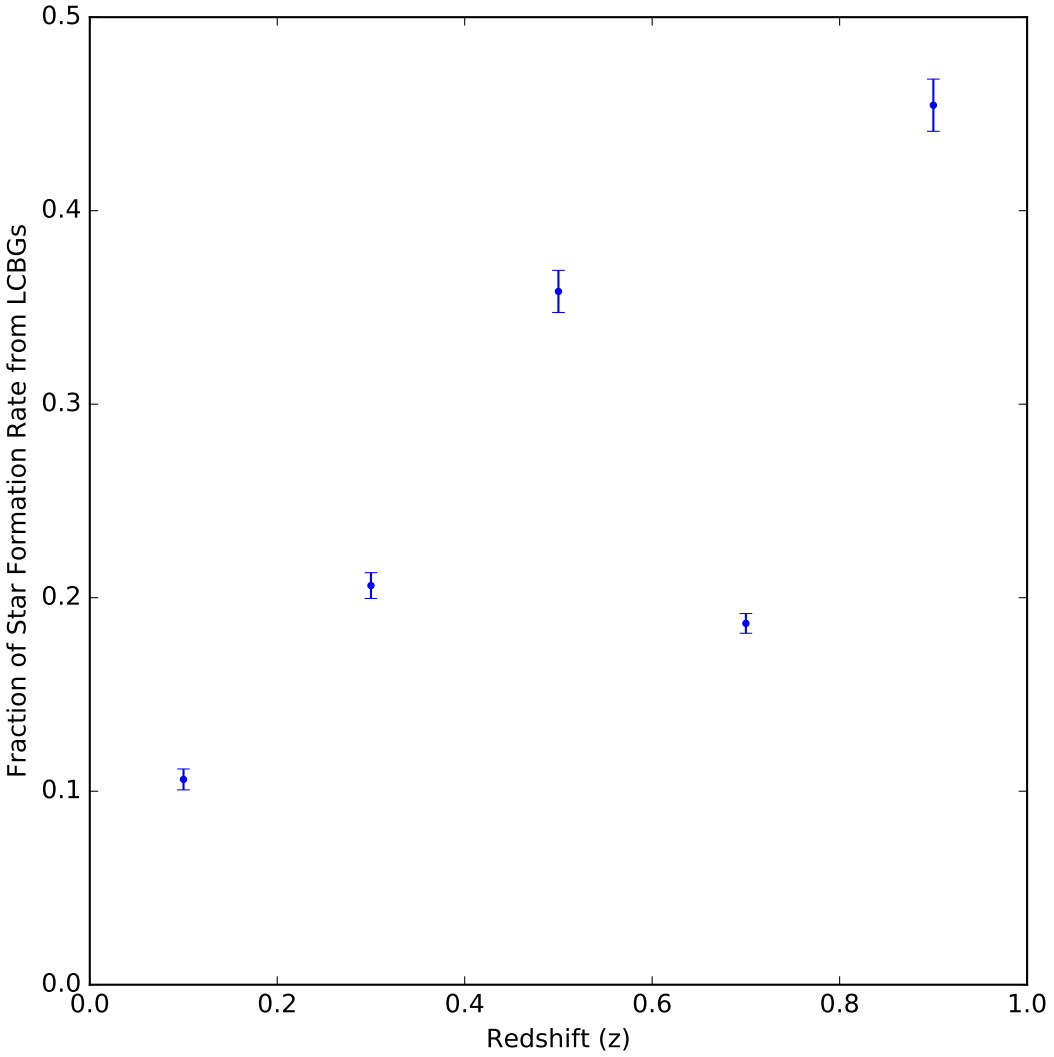

Figure 3.5 Above we have plotted the fraction of total SFR contributed by LCBGs at z=0.1,0.3,0.5,0.7,0.9

contribute ≈ 45% of the SFR density between z=0.4-1 for their sample of LCBGs with $I_{F814W} \leq 22.5$, similar to our galaxy selection criteria. This matches with the LCBG SFR fraction we find between z=0.4-0.6 and z=0.8-1.0 but our value between z=0.6-0.8 has a lower LCBG SFR fraction. We note this redshift range contains ≈ 20% more galaxies than the two surrounding ranges, and two galaxies in this sample have SFRs greater than 300 $M_\odot$ yr^{-1} contributing about 25% of the total SFR. It is possible these two sources have AGN, and if we remove them, LCBGs contribute ≈ 25% of the SFR.

3.6 Conclusions

We have used data from the CHILES survey to detect HI emission in two LCBGs. We found those LBCGs have HI masses of 4.2×10^9 and 1.2×10^{10} similar to values found in Garland et al. (2004). We detected HI in companions for both LCBGs. These companions were visible in photometric images, but had no redshift information which we have now been able to provide.

We also stacked LCBG spectra extracted from CHILES data to determine the upper limit of the average HI mass for LCBGs at various redshifts. We set a 5σ upper limit of 2.3×10^9 $M_\odot$ at z$\sim$ 0.239 up to 5.57×10^9 $M_\odot$ at z$\sim$ 0.428. These upper limits are larger than the average HI mass for LCBGs in the local universe as shown in Garland et al. (2004) and after adding the second epoch of observations we should be able to constrain the average HI mass in numerous bins and trace the evolution of HI in LCBGs to z=0.45.

Finally we have looked at the SFRs for LCBGs between z=0.0-1.0 using the 1.4 GHz radio continuum luminosity from CCP. We have found SFRs for 62 LCBGs that do not have AGN emission. We find the average SFR in LCBGs is increasing, like the number density of LCBGs. We find the average SFR for LCBGs at ~ 0.12 are consistent with SFRs in local LCBGs (Rabidoux, 2015), and the average SFRs of LCBGs in CCP at intermediate redshift are consistent with the SFRs calculated from Crawford et al. (2016). When comparing LCBG SFRs to all star forming galaxies detected in CCP, we find that at higher redshifts, LCBGs contribute a higher percentage of the total SFR. At z=0.1 LCBGs contribute approximately 10% of the total SFR, and that number goes up to 45% at z=0.9. As we continue to add the second epoch of CHILES observations to our study, we should be able to detect HI in more LCBGs and at higher redshifts, and constrain LCBG SFRs.

Chapter 4

The Search for HI Emission at z $\approx$ 0.4 in Gravitationally Lensed Galaxies with the Green Bank Telescope[1]

Abstract

Neutral hydrogen (HI) provides fuel for star formation, but is difficult to detect at high redshift due to weak emission, limited sensitivity of modern instruments, and terrestrial radio frequency interference (RFI) at low frequencies. We report the first attempt to use gravitational lensing to detect HI line emission from three gravitationally lensed galaxies behind the cluster Abell 773, two at redshifts of 0.398 and one at $z = 0.487$, using the Green Bank Telescope. We find a 3σ upper limit for a galaxy with a rotation velocity of 200 km s^{-1} is M$_{HI} = 6.58\times10^9$ and $1.5\times 10^{10}\ M_\odot$ at $z = 0.398$ and $z = 0.487$. The estimated HI masses of the sources at z= 0.398 and z= 0.487 are factors of 3.7 and $\sim$ 30 times lower than our detection limits at the respective redshifts. To facilitate these observations we have used sigma clipping to remove both narrow- and wideband RFI but retain the signal from the source. We are able to reduce the noise of the spectrum by $\sim$ 25% using our routine instead of discarding observations with too much RFI. The routine is most effective when $\sim$ 10% of the integrations or fewer contain RFI. These techniques can be used to study HI in highly magnified distant galaxies that are otherwise too faint to detect

[1]This chapter has been published as Hunt et al. (2016)

4.1 Introduction

In order to better understand the star formation history of the universe we must study the three indicators of star formation and its sustainability as a function of redshift: changes of stellar mass, star formation rate and gas content of galaxies. Studies of stellar mass density between redshifts, z, of zero and four have shown that approximately 10% of today's stellar mass has formed by $z \approx 3$ and 50% to 75% has formed at $z \approx 1$ (Dickinson et al., 2003; Rudnick et al., 2003; Fontana et al., 2003) with the total stellar mass density increasing by an order of magnitude between $z = 3.5$ and $z = 0.1$ (Ilbert et al., 2013; Marchesini et al., 2009; Pérez-González et al., 2008). Like stellar mass density, the star formation rate has been shown to increase with increasing redshift, up to an order of magnitude between $z = 0.01$ and $z = 1$ peaking between $z = 2$ and 3 (Hopkins & Beacom, 2006; Hopkins, 2004; Glazebrook et al., 2004; Wilson et al., 2002; Haarsma et al., 2000; Flores et al., 1999). Though stellar mass density and star formation rate density have similar trends, the predicted stellar mass density from instantaneous star formation rate density measurements is higher than the observed stellar mass density by approximately 60% (Madau & Dickinson, 2014). Studies of molecular gas, the material from which stars form, have been biased towards gas rich, actively star forming galaxies, but indicate that gas mass fraction increases over redshift, and peaks at $z \sim 2$ similar to the star formation rate (Carilli & Walter, 2013). Neutral atomic hydrogen (HI) in galaxies is the ultimate fuel for star formation, but the HI content of galaxies has only been measured in Damped Lyα systems beyond z= 2 (Noterdaeme et al.,

2012), and indirectly between $z \sim 0.25$ and $z = 2$. Saintonge et al. (2011) found little correlation between M_{HI} from Catinella et al. (2010) and M_{H_2} in massive galaxies in the CO Legacy Database for GALEX Arecibo SDSS Survey. Michałowski et al. (2015) found that galaxies hosting long gamma-ray bursts are deficient in molecular gas but abundant in HI suggesting that at least the initial burst of star formation could come directly from the atomic gas. So though we may have a glimpse at how molecular gas changes as a function of redshift we are still unsure how the atomic gas, still an imporant element of star formation, changes as a function of redshift between $z = 0$ and $z = 1$.

To date, atomic gas between $z = 0$ and $z = 0.2$ has been studied by measuring the 21 cm HI emission. Surveys such as ALFALFA and HIPASS have detected large samples of galaxies and measured their HI content out to $z \sim 0.08$ (Giovanelli et al., 2005; Zwaan et al., 2003), but until recently little was known about HI 21 cm emission beyond $z = 0.1$. Zwaan et al. (2001) used the Westerbork Synthesis Radio Telescope (WSRT) to make the first detection of HI at z$>$ 0.1, z=0.1766, finding $M_{HI} = (6.0 \pm 0.8) \times 10^9$ for a galaxy in the cluster Abell 2218. Catinella et al. (2008) and Verheijen et al. (2010) detected HI in $\sim$ 180 galaxies between z=0.16 $-$ 0.25 down to masses of $M_{HI} = 3 \times 10^{10}$ to $2 \times 10^9 M_\odot$ respectively with the Arecibo telescope and the Westerbork Synthesis Radio Telescope (WSRT) respectively.

Indirect detections of HI have been made to $z = 0.8$ using observing techniques such as stacking (Lah et al., 2009) and intensity mapping (Chang et al., 2010). Lah et al. (2009) found average HI mass of $(6.6 \pm 3.5) \times 10^9 M_\odot$ per galaxy in Abell 370, a

cluster at $z = 0.37$. Numerous groups have used the 100 m Green Bank Telescope[2] (GBT), the only telescope with a cooled receiver that can detect HI at redshift $z \geq 0.45$ with a reasonable integration time, to create an HI intensity map (Chang et al., 2010; Masui et al., 2013; Switzer et al., 2013). After cross-correlating the GBT data with optical data from the WiggleZ Dark Energy Survey, Masui et al. (2013) made a 7.4σ detection of HI density at z=0.8 of $\Omega_{HI} = (0.4 \pm 0.05(stat.) \pm 0.04(sys.)) \times 10^{-3} \times (1/rb)$, where r, the stochasticity, and b, the bias, are not well constrained.

Direct detections beyond $z = 0.25$ are difficult due to the weakness of the 21 cm HI line, the limited sensitivity and frequency coverage of present-day radio telescopes, and the many sources of radio frequency interference (RFI) in the frequency bands that cover redshifted HI emission. After successful pilot observations (Fernández et al., 2013), the COSMOS HI Large Extragalactic Survey (CHILES) is currently using the recently upgraded Karl G. Jansky Very Large Array to search for 21 cm emission in individual galaxies in the well observered COSMOS field out to $z = 0.45$. Telescopes designed specifically to carry out intensity mapping surveys, like the Canadian Hydrogen Intensity Mapping Experiment (CHIME) (Battye et al., 2013), Baryon acoustic oscillations In Neutral Gas Observations (BINGO) (Bandura et al., 2014), and Tianlai (Chen, 2015) will greatly improve measurements of Ω_{HI}. Planned deep field surveys with telescopes such as ASKAP, MeerKAT and the Square Kilometer Array (SKA) (Meyer, 2009; Holwerda et al., 2012; Staveley-

[2]The National Radio Astronomy Observatory (NRAO) is a facility of the National Science Foundation operated under cooperative agreement by Associated Universities, Inc.

Smith & Oosterloo, 2015) will have the sensitivity and frequency coverage required to directly detect HI emission in individual galaxies beyond $z = 0.45$.

Until these telescopes are completed, direct detections of magnified HI 21 cm emission from strongly lensed sources can be made to $z \sim 1$ using current telescopes (Deane et al., 2015). This technique has been used to detect magnified CO emission in many strongly lensed galaxies, the first being a galaxy at $z = 2.2867$ by Brown & Vanden Bout (1991), and more recently a survey detecting emission from sources beyond $z = 4$ (Vieira et al., 2013). Probing lensed sources for HI emission should also be possible, but careful concern is required when selecting these sources to ensure they are sufficiently magnified and the observed frequencies are not saturated with RFI. In this study we report on our observations of three gravitationally lensed galaxies behind the galaxy cluster Abell 773 (Sand et al., 2005), chosen because they had known redshifts and were likely to be highly magnified.

Throughout this paper we assume $H_o = 69.7 kms^{-1}Mpc^{-1}, \Omega_M = 0.282$, and $\Omega_\Lambda = 0.718$ (Hinshaw et al., 2013) and use the cosmology calculator from Wright (2006)[3] to calculate distances. In Section 4.2 we explain our observations, data reduction method, and the flagging method we used to remove RFI. In Section 4.3, we present the results. In Section 4.4, we discuss our results, the effectiveness of our flagging, and mass estimates based on galaxy magnitudes. In Section 4.5 we go through our conclusion and briefly discuss the application of our technique to additional targets.

[3]http://www.astro.ucla.edu/∼wright/CosmoCalc.html

4.2 Observations and Analysis

4.2.1 Sources

Three sources were selected, F3, F13 and F18, from a list gravitationally lensed galaxies behind various massive clusters observed with the Hubble Space Telescope (Sand et al., 2005). These observations were taken using the Wide Field Planetary Camera 2 (WFPC2) on the *Hubble Space Telescope* with the F702W filter. Sand et al. (2005) lists the magnitude of F3 as 21.21 ± 0.02, F13 as 21.52 ± 0.03 and F18 as 23.39 ± 0.11. F3 and F13 both lie at z= 0.398 and F18 lies at z= 0.487 (Richard et al., 2010; Sand et al., 2005). The sources are labeled in Figure 4.1, which shows the they all fall within the $\sim 13'$ GBT beam.

We originally targeted these sources because they fell within $0.25 \leq \ z \leq 1.0$ and had a high length-to-width ratio which suggested a higher magnification of $\sim$ 10. After our observations we obtained a lens model from J. Richard (2009, private communication) which yielded magnifications of 1.7 ± 0.1 for F3, 2.0 ± 0.2 for F13, and 2.7 ± 0.3 for F18.

4.2.2 Observations

Observations of the three galaxies were carried out at night in order to minimize RFI over seven years using the GBT which has a gain of 2 K Jy^{-1}. Observations occurred 2007 January 21 and 26, over eight sessions from 2008 January $16 - 24$, and over four sessions from 2014 February $2 - 6$. We used the Prime Focus 2 receiver ($901 - 1230$ MHz), and the Spectral Processor backend with two polarizations

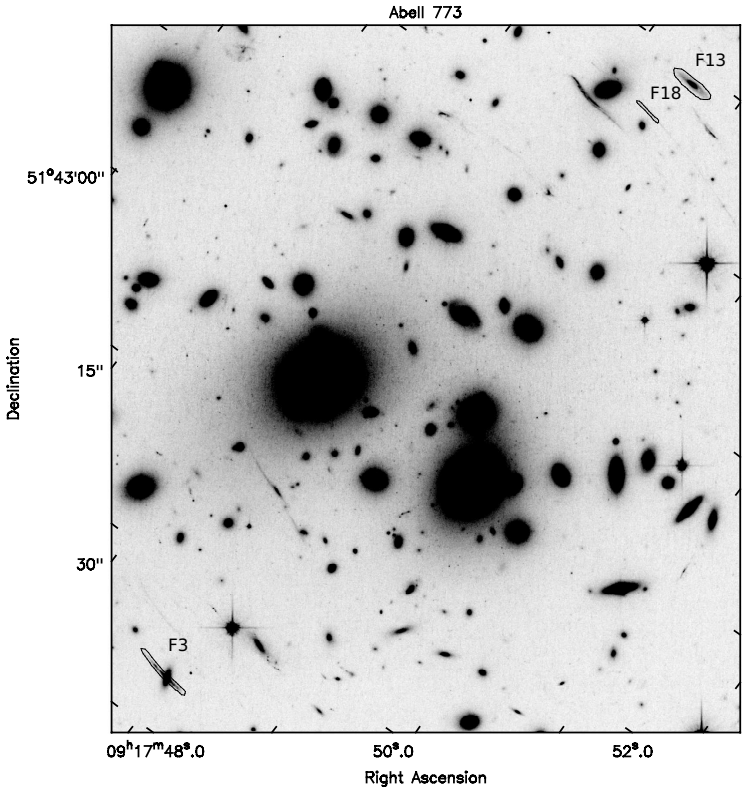

Figure 4.1 The above figure shows an HST F814W image of the galaxy cluster Abell 773. The lensed galaxies F3, F13, and F18 are labelled and outlined. The positions for each source can be found in Sand et al. (2005). The lensed galaxies should clearly fall within the 13' GBT beam.

and over two frequency bands for all observations. The first band was centered at 955 MHz ($z = 0.487$) and the second at 1016 MHz (z=0.398), each with 10 MHz bandwidth ($\Delta v = 3140$ km s^{-1} at 955 MHz and $\Delta v = 2952$ km s^{-1} at 1016 MHz). In 2007 and 2014 our data had 512 channels per frequency band for a frequency resolution of 19.5 KHz and a velocity resolution of 6.2 km s^{-1} at $z = 0.487$ and 5.8 km

	z=0.398	z=0.487
Observed Frequency (ν)	$1016 MHz$	$955.5 MHz$
Pointing Coordinates (J2000)	$09^h17^m54^s.62$, 51°43'44"6	
Observing Time (hr)	77.6	
Effective Integration Time (hr)	17.2	18.1
Bandwidth (MHz)	10	
Frequency Resolution (kHz)	39.1	
Velocity Resolution (km s^{-1})	11.5	12.3
System Temperature (K)	26.2	23.7
T_{cal} (K)	1.61	1.58
% Flagged	6	0.85

Table 4.1 Observing time is the total telescope time. Effective integration time is per polarization. Frequency and velocity resolutions listed are the final values after smoothing. T_{cal} is the temperature injected by the noise diode used to compare what is measured by the telescope to a known value for calibration. The percentage of data flagged includes integrations that were dropped because of high noise, and the percentage of data flagged in Fourier space.

s^{-1} at $z = 0.398$. In 2008 the configuration changed to 256 channels per frequency band with the final velocity resolution listed in Table 4.1. The beam size for the PF2 receiver is $\sim 13.6'$ at 955 MHz and $\sim 12.8'$ at 1018 MHz; the three sources we observed were within $1'$ of our pointing direction so that all of the emission falls within the beam.

The GBT is located in the National Radio Quiet Zone which greatly reduces most, but not all, RFI from terrestrial sources. These sources of RFI cause both wide and narrow band interference with a wide range of flux density and will be further discussed in Section 4.2.4. The Spectral Processor is ideally designed to handle the wide range of flux densities with a dynamic range of 45 dB.

Standard position switching was used for the observations, with a short integration time of two seconds to reduce the number of spectra affected by wideband

RFI. In 2007 we spent two minutes on source and two minutes off source, and switched to five minutes on source and five minutes off source for the 2008 and 2014 observations to reduce overhead. The off source pointing was carried out 2 minutes of right ascension, or 30 arcminutes, ahead of the source for the first year and 5 minutes of right ascension ahead of the source for the rest of the observations so that the same azimuth and zenith angle were tracked as the on source observations. Our total observing time was 77.6 hours, giving an integration time of 17.2 hours at $z = 0.398$ and 18.1 hours at $z = 0.487$.

4.2.3 Data Reduction

Reduction of the data was done using GBTIDL[4]. For each night, spectral window, on-off scan pair, polarization, and integration we used the *getps* procedure which calibrates a total power, position switched scan pair as defined in Equation 4.1 where T_{sys} is listed in Table 4.1, the gain for the GBT is 2 Jy K^{-1} and the atmospheric opacity correction is $\tau = 0.01$.

$$S = \frac{On - Off}{Off} \times T_{sys} \times \ Gain \times \ e^{\tau} \tag{4.1}$$

Next, a fifth order polynomial baseline, the lowest order polynomial that produces flat baselines, was fit across the frequencies 950.24-953.65 MHz, $954.15 - 957.25$ MHz and $957.95 - 960$ MHz at $z = 0.487$ and $1011.25 - 1011.75$ MHz and $1012.5 - 1021$

[4]GBTIDL (http://gbtidl.nrao.edu/) is the data reduction package produced by NRAO and written in the IDL language for the reduction of GBT data.

MHz at $z = 0.398$. This fit was applied to every integration whether wideband RFI was present or not. The fifth order polynomial applied across our 10 MHz bandwidth removes variations in the bandpass of roughly 2 MHz and should not affect a typical galaxy with a line width of $200 kms^{-1}$ (Papastergis et al., 2011) which would have a frequency width of $\lesssim$ 677 kHz. We developed an automated flagging routine, described in more detail in Section 4.2.4, which we then used to flag all RFI. A spectrum for each night and spectral window was created by accumulating integrations from all on-off scan pairs and both polarizations. The effective integration time at 1016 MHz is much lower, and percentage of data flagged much higher, because the data for one polarization on night two had abnormally high noise, and was flagged completely. There is no obvious reason for why the noise was higher in that one polarization. Next, we used a Gaussian kernel to smooth over the first two nights and the last four nights to change the frequency resolution from 19.5 kHz per channel (a velocity resolution of 6.2 km s^{-1} at $z = 0.487$ and 5.8 km s^{-1} at $z = 0.398$) to 39.1 kHz per channel (a velocity resolution of 12.3 km s^{-1} at $z = 0.487$ and 11.5 km s^{-1} at $z = 0.398$) to improve the noise and match the other eight nights. A fifth order polynomial baseline was fit to the final spectrum for each night and then we accumulated and averaged all nights to get the final spectrum.

4.2.4 RFI and Flagging Routine

The observed frequency bands contain a large amount of RFI which we believe is caused by airplane distance measuring equipment (DME) radar. The ground to

air portion of the radar transmits between 962 and 1024 MHz. Fisher et al. (2005) describes DME as a pair of strong pulses between an airplane and a ground station sent at 24 to 30 pairs a second, meaning that each pulse is much shorter than the two second integration time. Our two second integration time is a limit of the Spectral Processor, but future observations will be able to take advantage of the increased dynamic range and processing power of the VErsatile GBT Astronomical Spectrometer (VEGAS), allowing for increased bandwidth and spectral resolution, and shorter integration time. The wideband interference could come from a strong, intermittent DME signal outside of the observing band, appearing consecutively in up to 77 integrations. The time the RFI was visible in the data ranged from 2 seconds to 144 seconds, but was most frequently visible for ~ 4 seconds at a time. The wideband RFI has a characteristic width of 1 MHz which is still larger than the aforementioned 677 kHz frequency width expected for the signal.

Both wideband and narrow band interference were removed using a custom sigma clipping method (Yahil & Vidal, 1977), measuring the standard deviation of the spectrum and removing points above or below some multiple of that value. Channels around the clipped point were then blanked to remove the whole spike. This was done on the frequency spectrum (the frequency domain) to remove narrow band interference, and on its Fourier transform (the Fourier domain) to remove wideband interference.

We only wanted to flag spectra in the Fourier domain when wideband RFI was present in order to avoid unnecessarily removing data. The data containing wideband interference often had tall spikes in the Fourier transform, and we used

this to search for wideband interference. We also found the data that contained narrow band interference had tall spikes in Fourier space. From data analysis we saw that the narrow band interference occurred most frequently at 954 and 958 MHz at $z = 0.487$ and 1012 MHz and 1018 MHz at $z = 0.398$. Before we carried out our preliminary Fourier transform to search for wideband RFI, we quickly interpolated over those frequencies. This way we were able to test for wideband interference using the Fourier domain while avoiding confusion with narrow band interference. If a peak in Fourier space was measured over our threshold, a flux density greater than 0.015 Jy or less than -0.015 Jy, we assume that integration contains wideband interference.

We then started over with the original spectrum and continued our clipping routine. The values were selected after measuring the maximum and minimum values in the Fourier domain of many spectra both containing and lacking wideband RFI. The unaltered spectra were Fourier transformed and clipped, setting channels larger than 4.3σ to zero and doing the same for four channels on either side when the band had 512 channels and two channels on either side when the band had 256 channels to ensure the spike was removed. The value of 4.3σ and the number of channels flagged on either side of the spike were both chosen after testing various combinations to determine the combination that removed all wideband interference while flagging the lowest number of channels. After the spikes in the Fourier domain were removed, the spectrum was inverse Fourier transformed, and the wideband interference was no longer present in the frequency domain. We continued in the frequency domain, measuring the standard deviation across the central 2 MHz,

blanking channels larger than 3.5 σ, and removing seven channels on either side when the band had 512 channels, and four channels on either side when the band had 256 channels, eliminating most of the narrowband interference in the frequency domain. Because the narrow band RFI is ever present at 954 and 957.5 MHz we could not remove all of it from the final spectrum. Again the value for sigma clipping and width were determined by testing multiple scans to find the lowest combination of values to remove as much of the spike as possible without removing signal.

A test was developed to check the effectiveness of our flagging routine. We used a GBT observation of the galaxy NGC 5375 in which the signal from the galaxy is not visible in a single integration, but becomes visible when many integrations are averaged together. NGC 5375 is at much lower redshift and has a velocity width of 280 km s^{-1}, so its frequency width, 1.4 MHz, is 2.1 times larger than the assumed frequency width of the high redshift sources, 677 kHz. To make sure the HI signal is not visible in a single integration we artificially increased the noise in each channel in each integration by adding a random number to the measured flux density in each channel. The signal to noise ratio in each integration becomes 0.66 after adding this artificial noise, making the source undetectable in a single integration. Then we introduced wideband interference, extracted from our original dataset by fitting a high order polynomial, to approximately 10% of the integrations in the test dataset at random. It is important to note that we only flagged about 190 channels, much less than 1% of the data. Next we flagged the data in the Fourier domain for the integrations in which we introduced wideband interference, zeroing any values higher than 4.3 times the noise like we did to the sources behind Abell 773, and

did nothing to the others. We averaged all of the integrations to create a final average spectrum, and compared them to the unaltered final spectrum. The results in Figure 4.2.4 show that the HI signal looks the same when there is no wideband interference, and when the artificial wideband interference is removed using our flagging routine. The spectrum without wideband interference added had an RMS of 0.0093 Jy with an integrated signal to noise ratio of 8.2 and the spectrum with wideband interference added and then removed had an RMS of 0.0095 Jy with an integrated signal to noise ratio of 7.6. The RMS of the residual spectrum is 0.002 Jy. The signal to noise ratio and frequency width of the test source are much larger than those expected from our data, so the test represents an extreme and the flagging routine should have a smaller effect on our data.

4.3 Results

The final spectra are shown in Figure 4.3. The spectra have an RMS of 211 μJy at $z = 0.487$ and 204 μJy at $z = 0.398$. For comparison, the theoretical value for the noise is 183 μJy and 171 μJy respectively. This is calculated from

$$\sigma = \frac{T_{sys}}{G\ \sqrt{N_{pol}\ \Delta\nu\ t_{eff}}} \tag{4.2}$$

where T_{sys} is the system temperature, 23.7 K at $\nu = 1016$ MHZ and 26.2 K at $\nu =$ 955 MHZ, $G = 2KJy^{-1}$ is the gain, $N_{pol} = 2$ is the number of polarizations, $\Delta\nu =$

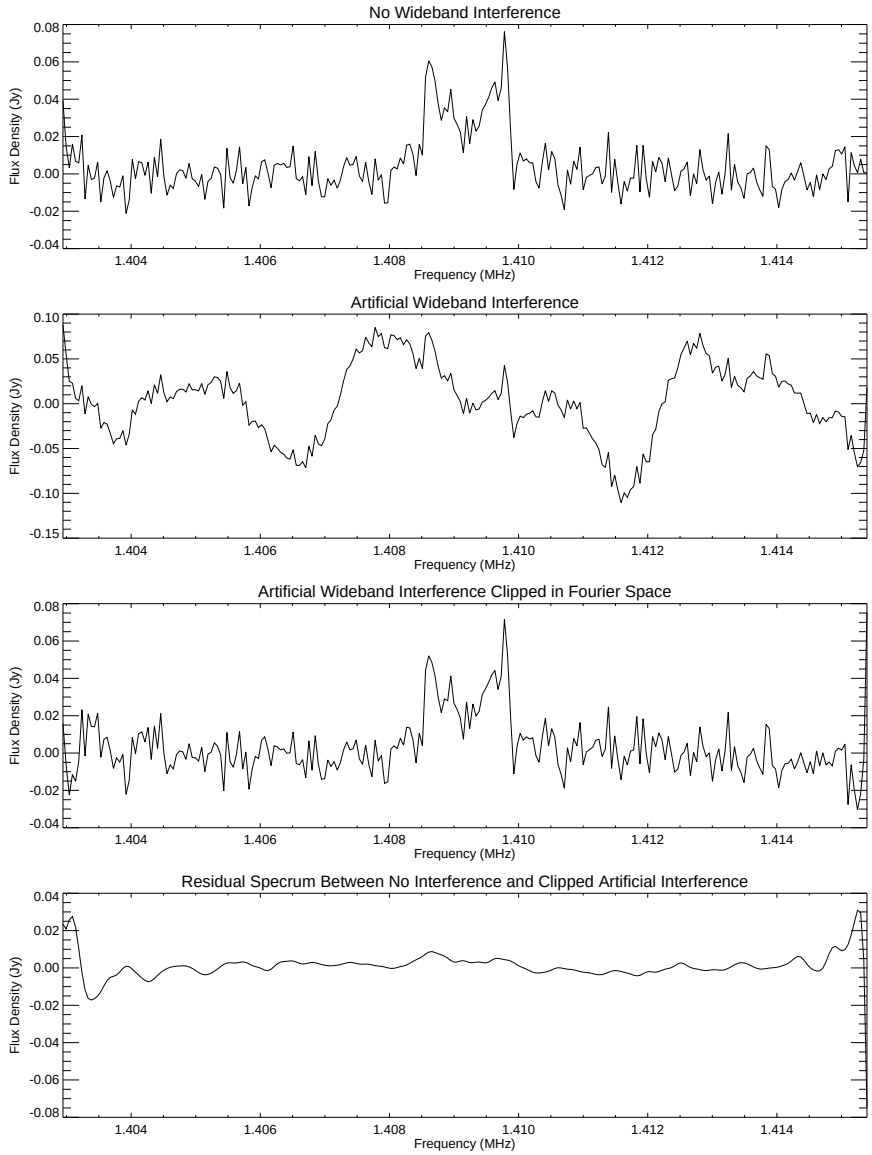

Figure 4.2 The above figures show the spectrum we used to test our flagging routine. The top plot shows the final spectrum without adding wideband interference. The middle plot shows the final spectrum after adding wideband interference to 10% of the integrations. The third plot shows the final spectrum after adding wideband interference and then applying our flagging routine.The final plot shows the difference between the spectrum in which no interference was added, and the spectrum which was flagged in Fourier space.

39.1 KHz is the frequency width per channel, and t_{eff} is the effective integration time listed in Table 4.1. The corresponding M_{HI} detection limit is

$$\sigma_{MHI} = \frac{2.36 \times 10^5 D_L^2 \sigma_s dv \sqrt{N} \sigma_{SNR}}{(1+z)\mu} \tag{4.3}$$

where σ_{MHI} is the upper limit of the neutral hydrogen mass, D_L is the luminosity distance to the object, 2.18 Gpc at $z = 0.398$ and 2.77 Gpc at $z = 0.487$, σ_s is the RMS per channel in the spectrum in units of Jy, dv is the channel width in km s^{-1}, N is the number of channels the galaxy would span, σ_{SNR} is the signal to noise ratio, z is redshift, and μ is the magnification. To set a mass limit we need to select a value for N. We use the mode of the line width, ~ 200 km s^{-1}, from 10744 galaxies in the Arecibo Legacy Fast ALFA (ALFALFA) survey (Papastergis et al., 2011) divided by a velocity resolution of 12.3 km s^{-1} at $z = 0.487$ and 11.5 km s^{-1} at $z = 0.398$ to find $N = 16$ and 17 respectively. Using the above parameters, we calculate the 3 σ detection limit to be $M_{HI} = 1.50\times\ 10^{10}\ M_\odot$ and $M_{HI} = 6.36 \times 10^9$ $M_\odot$ respectively.

4.4 Discussion

4.4.1 Effectiveness of Flagging

The flagging procedure we used was possible only because the galaxy is not visible in any single integration and there was no danger of clipping or altering our signal. As mentioned in §2.2, we measured the standard deviation of the central 2 MHz (628 km s^{-1} at 955 MHz and 590 km s^{-1} at 1016 MHz) of the spectrum in both

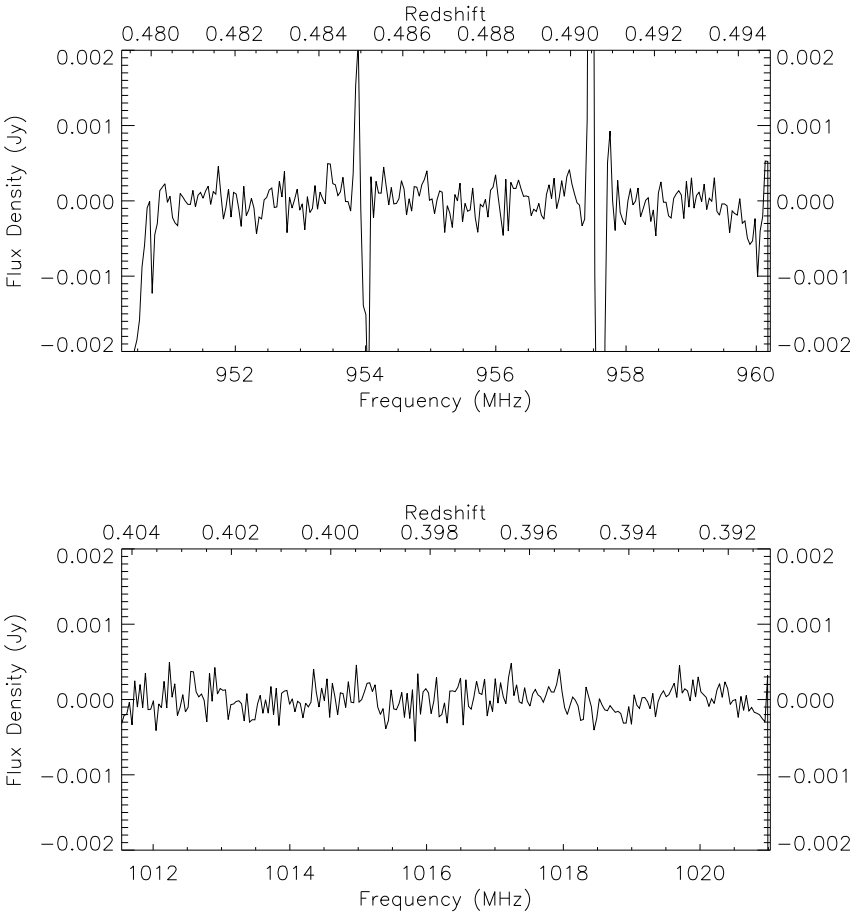

Figure 4.3 This is the final combined spectrum for our data at both $z = 0.398$ and $z = 0.487$. The RFI present at 954 MHz and 957.5 MHz persisted no matter how we changed our flagging routine.

bands and used that value for sigma-clipping. We did this because that region of the spectrum was generally devoid of narrow-band RFI. In the central 2 MHz very few integrations were clipped in the frequency domain, so besides the one polarization in night two that was discarded due to high noise, most of the information that was lost came from clipping in the Fourier domain. Only 6.53% of the data was flagged at 1016 MHz and 1.6% was flagged at 955 MHz. If we ignored integrations with wideband RFI instead of flagging in Fourier space, we would have removed $\sim 14\%$

of the data at 955 MHz and $\sim 10\%$ of the data at 1016 MHz. While this method has a small effect on the final noise of the spectrum, it also yields cleaner baselines.

In Figure 4.4 we show three examples of spectra before and after flagging. The top panel shows a spectrum with wideband RFI before and after flagging. In the first spectrum, our routine was effective at removing the wideband RFI and we were also able to remove narrowband spikes. The middle panel has a spectrum showing only narrow band RFI. The spectrum was not changed in Fourier space and the narrow band RFI was removed with sigma clipping. The bottom example in Figure 4.4 shows flagging done when the spectrum does not appear to contain any RFI. The spectrum before and after the flagging routine remained exactly the same.

Figure 4.5 shows the channels that were clipped most often in the frequency domain. In the band centered at 955 MHz (z=0.398) narrow band interference was frequently present near 954 MHz and 958 MHz. After changing our widening parameters we were still unable to remove it entirely from our final spectrum and it is still visible in Figure 4.3. We removed many channels on the edge and around 1012 MHz in the band centered at 1016 MHz (z=0.487). A large percentage of the data is flagged because of narrow band RFI outside the central region. The dips in the middle of each plot in Figure 4.5 correspond to the areas where we measured the standard deviation and retained most of the data.

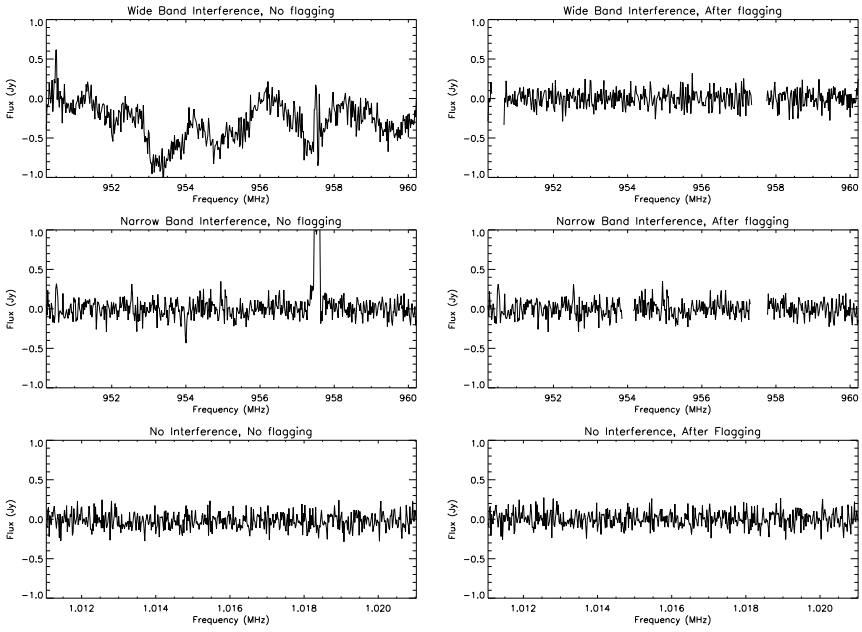

Figure 4.4 The above figures show the spectrum before and after the clipping procedure. The first example shows the clipping of a single integration that showed wideband and narrowband interference. You can see that the wave structure was removed and two spikes were removed. The second example shows clipping of only narrow band interference. The third example shows a spectrum that does not appear to have any interference. We measured the standard deviation before and after clipping and found that the spectrum was unaffected. Standard deviation was $\sigma = 0.102$ Jy for each spectrum

4.4.2 Mass Limits

We were able to use the scaling relation between R band absolute magnitude and HI mass described by Dénes et al. (2014) derived from the HI Parkes All Sky Survey (HIPASS), to estimate the HI mass for each galaxy. A galaxy type for these sources was not available so we assumed all threee were Sbc spirals, the best case scenario for detection. The estimated masses are $M_{HI_{F3}} = (2.2\pm1.3)\times10^9$, $M_{HI_{F13}} = (1.5\pm.8)\times10^9$, and $M_{HI_{F18}} = (4.7\pm2.3)\times10^8$. The calculated average mass weighted by the magnification for F3 and F13 is $M_{HI_{F3+F13}} = (1.8\pm0.7)\times10^9$. We obtained

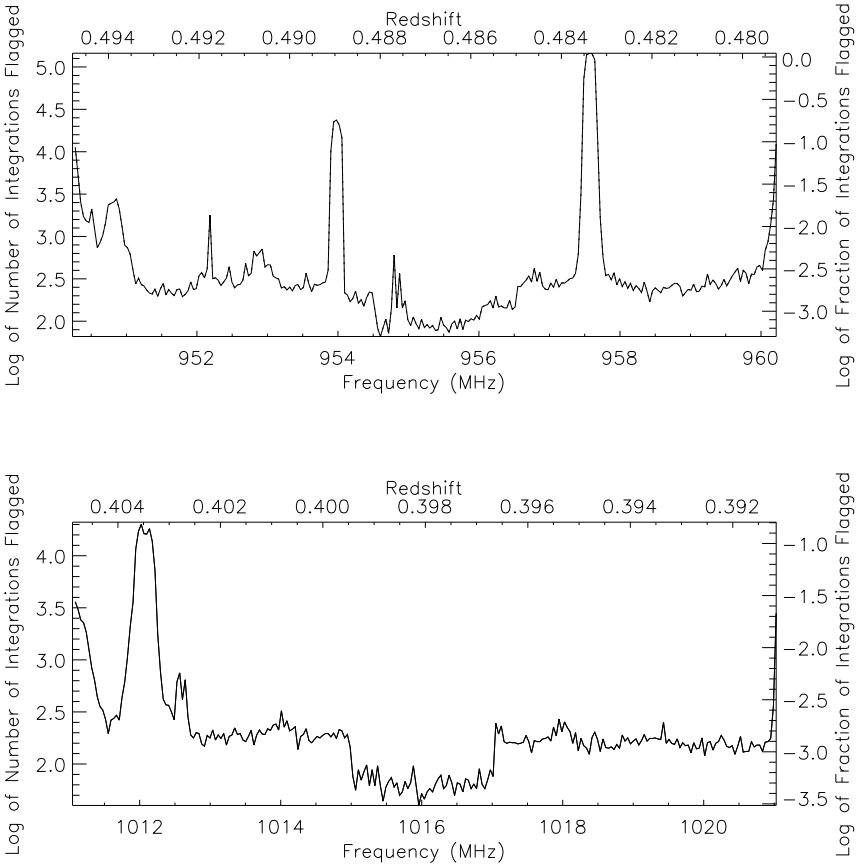

Figure 4.5 The above figures shows how often each frequency bin was clipped. The dip in the middle of each band is due to setting the standard deviation based on those frequencies. Since our statistics were based off that region, fewer data points were outside 3.5 times the standard deviation.

the local unmagnified R band magnitude by transforming the magnified, redshifted F702W magnitude using the k-corrections and color relations from Fukugita et al. (1995). F3 and F13 lie at the same redshift so we add the mass of the sources together weighted by their magnification for a total estimated mass detectable at $z = 0.398$. These mass estimates are ~ 30 and 3.7 times smaller than the detection limit for F18 and both F3 and F13 respectively. To bring the noise down to the level required to detect emission from F3 and F13 we require approximately 200 extra hours of integration time, or 800 hours of observation time.

Our detection limit would have been much lower if the length-to-width ratio had been a more accurate predictor of magnification, but future studies can target objects with known magnifications from more accurate lens models. We can use Figure 4.6 to determine the magnification required to detect sources of various mass with 25 hour integration time. For example, we should be able to detect a galaxy with $M_{HI} = 3.16 \times 10^9$ $M_\odot$ out to z=0.725 as long as it has a $\mu > 30$. A strongly lensed arc behind the cluster Abell 370 at z=0.725 has been mentioned in Richard et al. (2010). It appears to be an SBc type galaxy, which typically have higher HI mass (Roberts & Haynes, 1994), with a total magnification of 32, and should be detectable with the GBT within 100 hours of observation time.

4.5 Conclusions and Future Work

Gravitational lensing has been used to measure emission from molecular gas and stars at higher redshift in the past and we suggest it can be used to measure HI at high redshift with current telescopes. The lower frequencies of redshifted HI have a denser RFI environment and, as our observations show, can lead to over 10% of the data being discarded due to wideband RFI. To recover as much information as possible from our data we created a custom sigma clipping routine that removes wideband and narrowband interference. The narrowband interference is removed using sigma clipping in the frequency domain, and wideband interference is removed using sigma clipping in the Fourier domain. When we flag that data in the Fourier domain the information near the source is preserved and the wideband RFI removed,

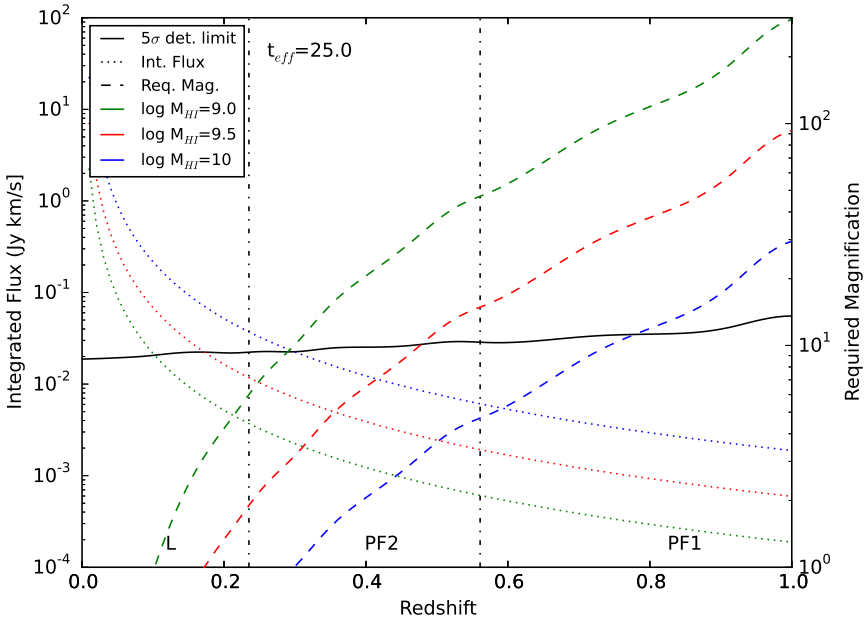

Figure 4.6 This figure shows the magnification necessary to detect a galaxy of $M_{HI} = 10^9$ $M_\odot$ (green), $10^{9.5}$ $M_\odot$ (red), 10^{10} $M_\odot$ (blue) at a given redshift using the GBT with a 25 hour effective integration time. The dotted line represents the integrated flux for each mass, the solid line indicates the 5σ detection limit with 25 hour effective integration time, and the dashed line indicates the magnification required to bring the integrated flux of the source up to the detection limit. The detection limit is calculated using the T_{sys} values of the GBT and fluctuates in accordance. The labels at the bottom (L, PF2, PF1) show the GBT receiver required to observe HI in the noted redshift range.

reducing the noise and flattening the baseline. Testing shows the routine is effective when the narrowband interference does not cover your signal, and when $\lesssim$ 10% of the integrations have wideband interference. We used this flagging technique on spectra from three sources behind the galaxy cluster Abell 773. Flagging the spectra with wideband interference in the Fourier domain rather than discarding them reduced the final noise in the spectrum by about 25%. The final noise per channel of our spectrum was $211\mu Jy$ at $z = 0.487$ and $204\mu Jy$ at $z = 0.398$. This flagging method can be combined with the magnification provided by gravitational

lensing to detect HI in individual galaxies out to and beyond a redshift of $z = 0.5$

We have observed three sources for an effective integration time of 18.1 hrs at $z = 0.487$ and 17.2 hrs at $z = 0.398$. The sources have low magnification, and were not detected, but we were able to set a 3σ detection limit on their masses of $\mathrm{M}_{HI} = 1.35\times\ 10^{10}\ M_{\odot}$ and $\mathrm{M}_{HI} = 6.36 \times 10^{9}\ M_{\odot}$ respectively which is higher than their estimated masses of 4.7×10^{8} and $1.8 \times 10^{9}\ M_{\odot}$ respectively. In order to detect these sources we require 235 additional hours of observation time. Adding more observation time now seems costly, so we must identify other sources to observe that should be detectable based on their magnification.

We have used the criteria from Figure 4.6 to find other sources that are detectable with the GBT. Sources beyond $z = 1$ would require unrealistically large magnifications, effective integration times, or HI masses to be detectable so we have identified 28 lenses below that redshift that can be targeted for similar observations. We have already begun observations on two sources behind the cluster Abell 370, one with a magnification of ~ 32 where an HI detection should be possible in an effective integration time of 25 hours.

Chapter 5

Conclusion

Previous studies of LCBGs have looked at snapshots in time to evaluate number density (Werk et al., 2004; Guzmán et al., 1997), star formation rates (Beare et al., 2015; Crawford et al., 2016; Guzmán et al., 1997), and HI mass (Garland et al., 2004, 2007; Rabidoux et al., 2014). With large, publicly available datasets like the Cosmic Evolution Survey (COSMOS), and deep radio frequency surveys like the COSMOS HI Extragalactic Survey (CHILES), we study the evolution of LCBGs in a single field between z=0.0-1.0, the redshift range in which we see their rapid evolution.

We find in Chapter 2 that the characteristic magnitude, M^* of LCBGs grows by 0.7 between z=0.0-1.0, consistent with the evolution of the population of blue galaxies over the same redshift range (Willmer et al., 2006; Beare et al., 2015). This indicates that the brighter blue galaxies become more numerous as we move to higher redshift. We see the total number density of LCBGs grows by a factor of ~ 11, more than an order of magnitude between z=0.0-1.0 and LCBGs make up 10% of the total galaxy population brighter than M_B=-18.5 at z$\sim$ 0.1 and $\sim$ 62% of the galaxy population brighter than M_B=-18.5 at z$\sim$ 0.9%. This is consistent with LCBGs being the most rapidly evolving population of galaxies over that redshift range (Rawat et al., 2007).

In Chapter 3 we detected 2 LCBGs in HI in the CHILES survey at z=0.045 and z=0.072 with HI masses 4.2×10^9 $M_\odot$ and 1.2×10^{10} $M_\odot$. We set limits on the average HI mass of LCBGs out to z=0.45 which are all higher than the average HI mass in the local universe of 2.9×10^9 $M_\odot$ except between z=0.15-0.3 where the spectra contain strong RFI from GPS for example. We looked at evolution of SFR in LCBGs and found that it increases out to z=1. Looking at LCBGs SFR as a fraction of the total SFR showed LCBGs make up $\sim \%10 - \%45$ of the total SFR between z= $0.0 - 1.0$ meaning they are a very important population to study if we want to understand why the star formation rate density evolves.

In Chapter 4 we presented observations of HI in gravitationally lensed galaxies. We find a 3σ upper limit for a galaxy with a rotation velocity of 200 km s^{-1} is $M_{HI} = 6.58\times10^9$ and $1.5\times\ 10^{10}\ M_\odot$ at $z = 0.398$ and $z = 0.487$ respectively. We also used a version of sigma clipping for this data set that clips in both frequency and Fourier space and reduces the amount of discarded data from $\sim$ 10 to $\sim$ 2%. We can use similar observations to study HI out to z=1 before the SKA is finally operational, and to target low mass objects that would otherwise require very long observation times.

5.1 Future studies of LCBGs

The large statistical study of LCBGs has shown how much they evolve, but has given little insight into what might be driving this evolution. We have just begun a study looking at the effect of environment on LCBGs. We are targeting five galaxy

clusters to get a statistical sample of LCBGs in a dense environment which we can then compare to LCBGs in the COSMOS field to determine how environment affects LCBGs. We also plan to use group information available for the COSMOS field (Knobel et al., 2012) to determine how environment effects LCBGs over the redshift range z=0.2-1.0.

We will also detect HI in a number of LCBGs with the next CHILES data release. With a larger sample of LCBGs with HI information, especially at higher redshift, we can constrain which evolutionary products are most likely. Since the HI disk is typically wider, we can get a better sense of how fast LCBGs are rotating and determine their total mass. The kinematic information will also tell us if LCBGs at higher redshift show evidence of rotation similar to Rabidoux et al. (2014). With these studies we can get a better grasp of what is driving the evolution of LCBGs and then what's driving the evolution of star formation rate density.

5.2 Gravitationally Lensed HI

We have already taken data for two galaxies behind the cluster Abell 370. Both galaxies have a much higher magnification and should likely be detectable in 100 hours of observation time. We are still working on RFI flagging, as the RFI environment is more complicated than that discussed in Chapter 4. We can also use telescopes like the recently upgraded GMRT or the GBT to target lensed galaxies that are at lower redshift and more easily detected. These observations will lead to the first detection of HI in a gravitationally lensed galaxy, and help us quantify

these observations in future deep field studies that will likely detect a number of lensed HI sources.

Bibliography

Ahn, C. P., Alexandroff, R., Allende Prieto, C., et al. 2014, ApJS, 211, 17

Andrews, S. K., Driver, S. P., Davies, L. J. M., et al. 2017, MNRAS, 464, 1569

Baldry, I. K., Alpaslan, M., Bauer, A. E., et al. 2014, MNRAS, 441, 2440

Bandura, K., Addison, G. E., Amiri, M., et al. 2014, in Proc. SPIE, Vol. 9145, Ground-based and Airborne Telescopes V, 914522

Battye, R. A., Browne, I. W. A., Dickinson, C., et al. 2013, MNRAS, 434, 1239

Beare, R., Brown, M. J. I., Pimbblet, K., Bian, F., & Lin, Y.-T. 2015, ApJ, 815, 94

Blanton, M. R., & Roweis, S. 2007, AJ, 133, 734

Brown, R. L., & Vanden Bout, P. A. 1991, AJ, 102, 1956

Capak, P., Aussel, H., Ajiki, M., et al. 2007, ApJS, 172, 99

Cardamone, C., Schawinski, K., Sarzi, M., et al. 2009, MNRAS, 399, 1191

Carilli, C. L., & Walter, F. 2013, ARA&A, 51, 105

Catinella, B., & Cortese, L. 2015, MNRAS, 446, 3526

Catinella, B., Haynes, M. P., Giovanelli, R., Gardner, J. P., & Connolly, A. J. 2008, ApJL, 685, L13

Catinella, B., Schiminovich, D., Kauffmann, G., et al. 2010, MNRAS, 403, 683

Chang, T.-C., Pen, U.-L., Bandura, K., & Peterson, J. B. 2010, Nature, 466, 463

Chen, X. 2015, IAU General Assembly, 22, 2252187

Choloniewski, J. 1986, MNRAS, 223, 1

Civano, F., Marchesi, S., Comastri, A., et al. 2016, ApJ, 819, 62

Coe, D., Zitrin, A., Carrasco, M., et al. 2013, ApJ, 762, 32

Coil, A. L., Blanton, M. R., Burles, S. M., et al. 2011, ApJ, 741, 8

Condon, J. J. 1992, ARA&A, 30, 575

Condon, J. J., & Yin, Q. F. 1990, ApJ, 357, 97

Cool, R. J., Eisenstein, D. J., Kochanek, C. S., et al. 2012, ApJ, 748, 10

Cool, R. J., Moustakas, J., Blanton, M. R., et al. 2013, ApJ, 767, 118

Cowie, L. L., Songaila, A., Hu, E. M., & Cohen, J. G. 1996, AJ, 112, 839

Crawford, S. M., Bershady, M. A., Glenn, A. D., & Hoessel, J. G. 2006, ApJL, 636, L13

Crawford, S. M., Wirth, G. D., & Bershady, M. A. 2014, ApJ, 786, 30

Crawford, S. M., Wirth, G. D., Bershady, M. A., & Randriamampandry, S. M. 2016, ApJ, 817, 87

Davies, L. J. M., Driver, S. P., Robotham, A. S. G., et al. 2015, MNRAS, 447, 1014

Deane, R. P., Obreschkow, D., & Heywood, I. 2015, MNRAS, 452, L49

Delhaize, J., Meyer, M. J., Staveley-Smith, L., & Boyle, B. J. 2013, MNRAS, 433, 1398

Dénes, H., Kilborn, V. A., & Koribalski, B. S. 2014, MNRAS, 444, 667

Dickinson, M., Papovich, C., Ferguson, H. C., & Budavári, T. 2003, ApJ, 587, 25

Efron, B., & Stein, C. 1981, Ann. Statist., 9, 586. http://dx.doi.org/10.1214/aos/1176345462

Efstathiou, G., Ellis, R. S., & Peterson, B. A. 1988, MNRAS, 232, 431

Faber, S. M., Willmer, C. N. A., Wolf, C., et al. 2007, ApJ, 665, 265

Fernández, X., van Gorkom, J. H., Hess, K. M., et al. 2013, ApJL, 770, L29

Fernández, X., Gim, H. B., van Gorkom, J. H., et al. 2016, ApJL, 824, L1

Fisher, J. R., Zhang, Q., Zheng, Y., Wilson, S. G., & Bradley, R. F. 2005, AJ, 129, 2940

Flores, H., Hammer, F., Thuan, T. X., et al. 1999, ApJ, 517, 148

Fontana, A., Donnarumma, I., Vanzella, E., et al. 2003, ApJL, 594, L9

Fritz, A., Scodeggio, M., Ilbert, O., et al. 2014, A&A, 563, A92

Fukugita, M., Shimasaku, K., & Ichikawa, T. 1995, PASP, 107, 945

Garilli, B., Le Fèvre, O., Guzzo, L., et al. 2008, A&A, 486, 683

Garland, C. A., Pisano, D. J., Mac Low, M.-M., et al. 2015, ApJ, 807, 134

Garland, C. A., Pisano, D. J., Williams, J. P., Guzmán, R., & Castander, F. J. 2004, ApJ, 615, 689

Garland, C. A., Pisano, D. J., Williams, J. P., et al. 2007, ApJ, 671, 310

Garland, C. A., Williams, J. P., Pisano, D. J., et al. 2005, ApJ, 624, 714

Giovanelli, R., Haynes, M. P., Kent, B. R., et al. 2005, AJ, 130, 2598

Glazebrook, K., Tober, J., Thomson, S., Bland-Hawthorn, J., & Abraham, R. 2004, AJ, 128, 2652

Guzmán, R., Gallego, J., Koo, D. C., et al. 1997, ApJ, 489, 559

Guzmán, R., Jangren, A., Koo, D. C., Bershady, M. A., & Simard, L. 1998, ApJL, 495, L13

Guzmán, R., Koo, D. C., Faber, S. M., et al. 1996, ApJL, 460, L5

Guzmán, R., Östlin, G., Kunth, D., et al. 2003, ApJL, 586, L45

Haarsma, D. B., Partridge, R. B., Windhorst, R. A., & Richards, E. A. 2000, in Bulletin of the American Astronomical Society, Vol. 32, American Astronomical Society Meeting Abstracts #196, 685

Hales, C. A., & Middelberg, E. 2014, pieflag: CASA task to efficiently flag bad data, Astrophysics Source Code Library, , , ascl:1408.014

Hales, C. A., Murphy, T., Curran, J. R., et al. 2012, MNRAS, 425, 979

Heckman, T. M., Hoopes, C. G., Seibert, M., et al. 2005, ApJL, 619, L35

Hinshaw, G., Larson, D., Komatsu, E., et al. 2013, ApJS, 208, 19

Holwerda, B. W., Blyth, S.-L., & Baker, A. J. 2012, in IAU Symposium, Vol. 284, The Spectral Energy Distribution of Galaxies - SED 2011, ed. R. J. Tuffs & C. C. Popescu, 496–499

Hopkins, A. M. 2004, ApJ, 615, 209

Hopkins, A. M., & Beacom, J. F. 2006, ApJ, 651, 142

Hoyos, C., Guzmán, R., Bershady, M. A., Koo, D. C., & Díaz, A. I. 2004, AJ, 128, 1541

Huang, S., Haynes, M. P., Giovanelli, R., & Brinchmann, J. 2012, ApJ, 756, 113

Hunt, L. R., Pisano, D. J., & Edel, S. 2016, AJ, 152, 30

Ilbert, O., Tresse, L., Zucca, E., et al. 2005, A&A, 439, 863

Ilbert, O., Capak, P., Salvato, M., et al. 2009, ApJ, 690, 1236

Ilbert, O., McCracken, H. J., Le Fèvre, O., et al. 2013, A&A, 556, A55

Johnson, H. L., & Morgan, W. W. 1953, ApJ, 117, 313

Kazanas, D., Fukumura, K., Behar, E., Contopoulos, I., & Shrader, C. 2012, The Astronomical Review, 7, 92

Kennicutt, Jr., R. C., Tamblyn, P., & Congdon, C. E. 1994, ApJ, 435, 22

Knobel, C., Lilly, S. J., Carollo, C. M., et al. 2012, ApJ, 755, 48

Koo, D. C., Bershady, M. A., Wirth, G. D., Stanford, S. A., & Majewski, S. R. 1994, ApJL, 427, L9

Koo, D. C., Guzman, R., Faber, S. M., et al. 1995, ApJL, 440, L49

Koo, D. C., & Kron, R. G. 1988, ApJ, 325, 92

Koo, D. C., Kron, R. G., & Cudworth, K. M. 1986, PASP, 98, 285

Kroupa, P. 2001, MNRAS, 322, 231

Lah, P., Pracy, M. B., Chengalur, J. N., et al. 2009, MNRAS, 399, 1447

Lange, R., Driver, S. P., Robotham, A. S. G., et al. 2015, MNRAS, 447, 2603

Lilly, S. J., Le Brun, V., Maier, C., et al. 2009, ApJS, 184, 218

Lynden-Bell, D. 1971, MNRAS, 155, 95

Madau, P., & Dickinson, M. 2014, ARA&A, 52, 415

Marchesini, D., van Dokkum, P. G., Förster Schreiber, N. M., et al. 2009, ApJ, 701, 1765

Masui, K. W., Switzer, E. R., Banavar, N., et al. 2013, ApJL, 763, L20

McCracken, H. J., Milvang-Jensen, B., Dunlop, J., et al. 2012, A&A, 544, A156

Meyer, M. 2009, in Panoramic Radio Astronomy: Wide-field 1-2 GHz Research on Galaxy Evolution, 15

Michałowski, M. J., Gentile, G., Hjorth, J., et al. 2015, A&A, 582, A78

Noeske, K. G., Koo, D. C., Phillips, A. C., et al. 2006, ApJL, 640, L143

Noterdaeme, P., Petitjean, P., Carithers, W. C., et al. 2012, A&A, 547, L1

Odekon, M. C., Koopmann, R. A., Haynes, M. P., et al. 2016, ApJ, 824, 110

Oliver, S. J., Bock, J., Altieri, B., et al. 2012, MNRAS, 424, 1614

Papastergis, E., Martin, A. M., Giovanelli, R., & Haynes, M. P. 2011, ApJ, 739, 38

Pérez-Gallego, J., Guzmán, R., Castillo-Morales, A., et al. 2011, MNRAS, 418, 2350

Pérez-González, P. G., Rieke, G. H., Villar, V., et al. 2008, ApJ, 675, 234

Phillips, A. C., Guzmán, R., Gallego, J., et al. 1997, ApJ, 489, 543

Rabidoux, K. 2015, PhD thesis, West Virginia University, proQuest Dissertations Publishing, 2015. 3718541

Rabidoux, K., Pisano, D. J., Garland, C. A., et al. 2014, ArXiv e-prints, arXiv:1412.4739

Randriamampandry, S. M., Crawford, S. M., Bershady, M. A., Wirth, G. D., & Cress, C. M. 2017, ArXiv e-prints, arXiv:1706.04534

Rao, S., & Briggs, F. 1993, ApJ, 419, 515

Rawat, A., Kembhavi, A. K., Hammer, F., Flores, H., & Barway, S. 2007, A&A, 469, 483

Rhee, J., Lah, P., Chengalur, J. N., Briggs, F. H., & Colless, M. 2016, MNRAS, 460, 2675

Rhee, J., Zwaan, M. A., Briggs, F. H., et al. 2013, MNRAS, 435, 2693

Richard, J., Smith, G. P., Kneib, J.-P., et al. 2010, MNRAS, 404, 325

Roberts, M. S., & Haynes, M. P. 1994, ARA&A, 32, 115

Rubin, V. C., & Ford, Jr., W. K. 1970, ApJ, 159, 379

Rudnick, G., Rix, H.-W., Franx, M., et al. 2003, ApJ, 599, 847

Russell, H. N. 1914, Popular Astronomy, 22, 275

Saintonge, A., Kauffmann, G., Wang, J., et al. 2011, MNRAS, 415, 61

Sand, D. J., Treu, T., Ellis, R. S., & Smith, G. P. 2005, ApJ, 627, 32

Sanders, D. B., Salvato, M., Aussel, H., et al. 2007, ApJS, 172, 86

Schade, D., Lilly, S. J., Crampton, D., et al. 1995, ApJL, 451, L1

Schade, D., Lilly, S. J., Le Fevre, O., Hammer, F., & Crampton, D. 1996, ApJ, 464, 79

Schechter, P. 1976, ApJ, 203, 297

Schmidt, M. 1968, ApJ, 151, 393

Schneider, P. 2006, in Saas-Fee Advanced Course 33: Gravitational Lensing: Strong, Weak and Micro, ed. G. Meylan, P. Jetzer, P. North, P. Schneider, C. S. Kochanek, & J. Wambsganss, 1–89

Scoville, N., Aussel, H., Brusa, M., et al. 2007, ApJS, 172, 1

Smolčić, V., Novak, M., Bondi, M., et al. 2017a, A&A, 602, A1

Smolčić, V., Novak, M., Delvecchio, I., et al. 2017b, A&A, 602, A6

Smolčić, V., Delvecchio, I., Zamorani, G., et al. 2017c, A&A, 602, A2

Stark, D. V., Kannappan, S. J., Eckert, K. D., et al. 2016, ApJ, 832, 126

Staveley-Smith, L., & Oosterloo, T. 2015, Advancing Astrophysics with the Square Kilometre Array (AASKA14), 167

Switzer, E. R., Masui, K. W., Bandura, K., et al. 2013, MNRAS, 434, L46

Tammann, G. A., Yahil, A., & Sandage, A. 1979, ApJ, 234, 775

Taniguchi, Y., Scoville, N., Murayama, T., et al. 2007, ApJS, 172, 9

Taniguchi, Y., Kajisawa, M., Kobayashi, M. A. R., et al. 2015, 67, 104

Tasca, L. A. M., Kneib, J.-P., Iovino, A., et al. 2009, A&A, 503, 379

Tollerud, E. J., Barton, E. J., van Zee, L., & Cooke, J. 2010, ApJ, 708, 1076

Turner, E. L. 1979, ApJ, 231, 645

Tyson, J. A. 1988, AJ, 96, 1

Verheijen, M., Deshev, B., van Gorkom, J., et al. 2010, ArXiv e-prints, arXiv:1009.0279

Vieira, J. D., Marrone, D. P., Chapman, S. C., et al. 2013, Nature, 495, 344

Werk, J. K., Jangren, A., & Salzer, J. J. 2004, ApJ, 617, 1004

Wieringa, M. H., de Bruyn, A. G., & Katgert, P. 1992, A&A, 256, 331

Willmer, C. N. A., Faber, S. M., Koo, D. C., et al. 2006, ApJ, 647, 853

Wilson, G., Cowie, L. L., Barger, A. J., & Burke, D. J. 2002, AJ, 124, 1258

Wright, A. H., Robotham, A. S. G., Bourne, N., et al. 2016, MNRAS, 460, 765

Wright, E. L. 2006, PASP, 118, 1711

Yahil, A., & Vidal, N. V. 1977, ApJ, 214, 347

Zamojski, M. A., Schiminovich, D., Rich, R. M., et al. 2007, ApJS, 172, 468

Zucca, E., Zamorani, G., Vettolani, G., et al. 1997, A&A, 326, 477

Zucca, E., Bardelli, S., Bolzonella, M., et al. 2009, A&A, 508, 1217

Zwaan, M. A., van Dokkum, P. G., & Verheijen, M. A. W. 2001, Science, 293, 1800

Zwaan, M. A., Staveley-Smith, L., Koribalski, B. S., et al. 2003, AJ, 125, 2842